US00RE48612E

(19) **United States**
(12) **Reissued Patent**
Yun et al.

(10) **Patent Number: US RE48,612 E**
(45) **Date of Reissued Patent: *Jun. 29, 2021**

(54) **X-RAY INTERFEROMETRIC IMAGING SYSTEM**

(71) Applicant: **Sigray, Inc.**, Concord, CA (US)

(72) Inventors: **Wenbing Yun**, Walnut Creek, CA (US); **Sylvia Jia Yun Lewis**, San Francisco, CA (US); **Janos Kirz**, Berkeley, CA (US)

(73) Assignee: **Sigray, Inc.**, Concord, CA (US)

(*) Notice: This patent is subject to a terminal disclaimer.

(21) Appl. No.: **16/523,940**

(22) Filed: **Jul. 26, 2019**

Related U.S. Patent Documents

Reissue of:
(64) Patent No.: **9,719,947**
Issued: **Aug. 1, 2017**
Appl. No.: **14/700,137**
Filed: **Apr. 29, 2015**

U.S. Applications:
(63) Continuation-in-part of application No. 14/527,523, filed on Oct. 29, 2014, now abandoned.
(Continued)

(51) **Int. Cl.**
G01N 23/02 (2006.01)
G01N 23/20 (2018.01)
(Continued)

(52) **U.S. Cl.**
CPC ***G01N 23/20075*** (2013.01); ***A61B 6/4007*** (2013.01); ***A61B 6/4291*** (2013.01);
(Continued)

(58) **Field of Classification Search**
CPC G01N 23/20075; A61B 6/4007; A61B 6/484; A61B 6/508; A61B 6/4291;
(Continued)

(56) **References Cited**

U.S. PATENT DOCUMENTS

1,203,495	A	10/1916	Coolidge
1,211,092	A	1/1917	Coolidge

(Continued)

FOREIGN PATENT DOCUMENTS

CN	101257851	9/2008
CN	101532969	9/2009

(Continued)

OTHER PUBLICATIONS

"Diamond," Section 10.4.2 of Zorman et al., "Material Aspects of Micro-Nanoelectromechanical Systems," Chapter 10 of Springer Handbook of Nanotechnology, 2nd ed., Barat Bushan, ed. (Springer Science + Business Media, Inc., New York, 2007), pp. 312-314.

(Continued)

Primary Examiner — Deandra M Hughes
(74) *Attorney, Agent, or Firm* — Knobbe, Martens, Olson, Bear, LLP

(57) **ABSTRACT**

An x-ray interferometric imaging system in which the x-ray source comprises a target having a plurality of structured coherent sub-sources of x-rays embedded in a thermally conducting substrate. The system additionally comprises a beam-splitting grating G_1 that establishes a Talbot interference pattern, which may be a π phase-shifting grating, and an x-ray detector to convert two-dimensional x-ray intensities into electronic signals. The system may also comprise a second analyzer grating G_2 that may be placed in front of the detector to form additional interference fringes, a means to translate the second grating G_2 relative to the detector. The system may additionally comprise an antiscattering grid to reduce signals from scattered x-rays. Various configurations of dark-field and bright-field detectors are also disclosed.

16 Claims, 42 Drawing Sheets

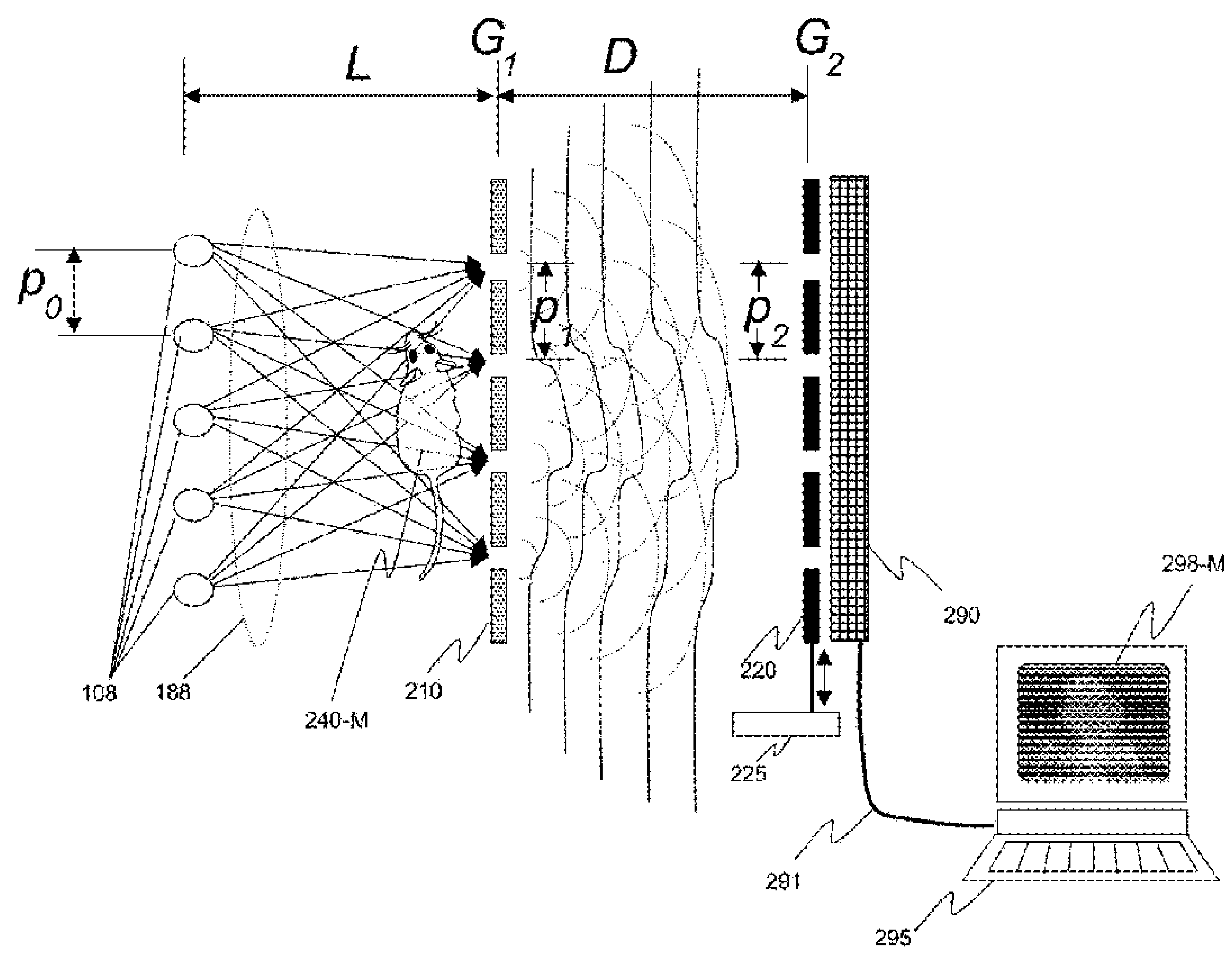

Related U.S. Application Data

(60) Provisional application No. 61/993,811, filed on May 15, 2014, provisional application No. 61/991,889, filed on May 12, 2014, provisional application No. 61/989,743, filed on May 7, 2014, provisional application No. 61/987,106, filed on May 1, 2014, provisional application No. 61/981,098, filed on Apr. 17, 2014, provisional application No. 61/901,361, filed on Nov. 7, 2013, provisional application No. 61/898,019, filed on Oct. 31, 2013.

(51) **Int. Cl.**

G21K 1/02	(2006.01)
A61B 6/00	(2006.01)
H01J 35/08	(2006.01)

(52) **U.S. Cl.**
CPC ***A61B 6/484*** (2013.01); ***A61B 6/508*** (2013.01); ***G21K 1/02*** (2013.01); ***H01J 35/08*** (2013.01); *G21K 2207/005* (2013.01); *H01J 35/116* (2019.05); *H01J 2235/086* (2013.01)

(58) **Field of Classification Search**
CPC H01J 35/08; H01J 2235/086; H01J 35/116; G21K 2207/005
See application file for complete search history.

(56) **References Cited**

U.S. PATENT DOCUMENTS

1,215,116	A	2/1917	Coolidge	
1,328,495	A	1/1920	Coolidge	
1,355,126	A	10/1920	Coolidge	
1,790,073	A	1/1931	Pohl	
1,917,099	A	7/1933	Coolidge	
1,946,312	A	2/1934	Coolidge	
2,926,270	A	2/1960	Zunick	
3,795,832	A	3/1974	Holland	
4,165,472	A	8/1979	Wittry	
4,192,994	A	3/1980	Kastner	
4,227,112	A	10/1980	Waugh et al.	
4,266,138	A	5/1981	Nelson et al.	
4,426,718	A	1/1984	Hayashi	
4,523,327	A	6/1985	Eversole	
4,573,186	A	2/1986	Reinhold	
4,727,000	A	2/1988	Ovshinsky	
4,798,446	A	1/1989	Hettrick	
4,807,268	A	2/1989	Wittry	
4,940,319	A	7/1990	Ueda et al.	
4,945,552	A	7/1990	Ueda	
4,951,304	A	8/1990	Piestrup et al.	
4,972,449	A	11/1990	Upadhya et al.	
5,001,737	A	3/1991	Lewis et al.	
5,008,918	A	4/1991	Lee et al.	
5,119,408	A	6/1992	Little	
5,132,997	A	7/1992	Kojima	
5,148,462	A	9/1992	Spitsyn et al.	
5,173,928	A	12/1992	Momose et al.	
5,249,216	A	9/1993	Ohsugi et al.	
5,276,724	A	1/1994	Kumasaka et al.	
5,371,774	A	12/1994	Cerrina	
5,452,142	A	9/1995	Hall	
5,461,657	A	10/1995	Hayashida	
5,513,237	A	4/1996	Nobuta et al.	
5,602,899	A	2/1997	Larson	
5,604,782	A	2/1997	Cash, Jr.	
5,629,969	A	5/1997	Koshishiba	
5,657,365	A	8/1997	Yamamoto et al.	
5,682,415	A	10/1997	O'Hara	
5,715,291	A	2/1998	Momose	
5,729,583	A	3/1998	Tang et al.	
5,737,387	A	4/1998	Smither	
5,768,339	A	6/1998	O'Hara	
5,772,903	A	6/1998	Hirsch	
5,778,039	A	7/1998	Hossain	
5,799,056	A	8/1998	Gulman	
5,812,629	A	9/1998	Clauser	
5,825,848	A	10/1998	Virshup et al.	
5,832,052	A	11/1998	Hirose et al.	
5,857,008	A	1/1999	Reinhold	
5,878,110	A	3/1999	Yamamoto et al.	
5,881,126	A	3/1999	Momose	
5,912,940	A	6/1999	O'Hara	
5,930,325	A	7/1999	Momose	
6,108,397	A	8/2000	Cash, Jr.	
6,108,398	A	8/2000	Mazor et al.	
6,118,853	A	9/2000	Hansen et al.	
6,125,167	A	9/2000	Morgan	
6,181,773	B1 *	1/2001	Lee	G21K 1/025 378/154
6,195,410	B1	2/2001	Cash, Jr.	
6,226,347	B1	5/2001	Golenhofen	
6,278,764	B1	8/2001	Barbee, Jr. et al.	
6,307,916	B1	10/2001	Rogers et al.	
6,359,964	B1	3/2002	Kogan	
6,377,660	B1	4/2002	Ukita et al.	
6,381,303	B1	4/2002	Vu et al.	
6,389,100	B1	5/2002	Verman et al.	
6,430,254	B2	8/2002	Wilkins	
6,430,260	B1	8/2002	Snyder	
6,442,231	B1	8/2002	O'Hara	
6,456,688	B1	9/2002	Taguchi et al.	
6,463,123	B1	10/2002	Korenev	
6,487,272	B1	11/2002	Kutsuzawa	
6,504,901	B1	1/2003	Loxley et al.	
6,504,902	B2	1/2003	Iwasaki et al.	
6,507,388	B2	1/2003	Burghoorn	
6,553,096	B1	4/2003	Zhou et al.	
6,560,313	B1	5/2003	Harding et al.	
6,560,315	B1	5/2003	Price et al.	
6,707,883	B1	3/2004	Tiearney et al.	
6,711,234	B1	3/2004	Loxley et al.	
6,763,086	B2	7/2004	Platonov	
6,811,612	B2	11/2004	Gruen et al.	
6,815,363	B2	11/2004	Yun et al.	
6,829,327	B1	12/2004	Chen	
6,847,699	B2	1/2005	Rigali et al.	
6,850,598	B1	2/2005	Fryda et al.	
6,870,172	B1	3/2005	Mankos et al.	
6,885,503	B2	4/2005	Yun et al.	
6,891,627	B1	5/2005	Levy et al.	
6,914,723	B2	7/2005	Yun et al.	
6,917,472	B1	7/2005	Yun et al.	
6,934,359	B2	8/2005	Chen	
6,947,522	B2	9/2005	Wilson et al.	
6,975,703	B2	12/2005	Wilson et al.	
7,003,077	B2	2/2006	Jen et al.	
7,006,596	B1	2/2006	Janik	
7,015,467	B2	3/2006	Maldonado et al.	
7,023,950	B1	4/2006	Annis	
7,023,955	B2	4/2006	Chen et al.	
7,057,187	B1	6/2006	Yun et al.	
7,076,026	B2	6/2006	Verman et al.	
7,079,625	B2	7/2006	Lenz	
7,095,822	B1	8/2006	Yun	
7,103,138	B2	9/2006	Pelc et al.	
7,110,503	B1	9/2006	Kumakhov	
7,119,953	B2	10/2006	Yun et al.	
7,120,228	B2	10/2006	Yokhin et al.	
7,130,375	B1	10/2006	Yun et al.	
7,149,283	B2 *	12/2006	Hoheisel	G21K 1/025 378/149
7,170,969	B1	1/2007	Yun et al.	
7,180,979	B2	2/2007	Momose	
7,180,981	B2	2/2007	Wang	
7,183,547	B2	2/2007	Yun et al.	
7,215,736	B1	5/2007	Wang et al.	
7,215,741	B2	5/2007	Ukita et al.	
7,218,700	B2	5/2007	Huber et al.	
7,218,703	B2	5/2007	Yada et al.	
7,221,731	B2	5/2007	Yada et al.	
7,245,696	B2	7/2007	Yun et al.	
7,264,397	B2	9/2007	Ritter	

(56) References Cited

U.S. PATENT DOCUMENTS

7,268,945	B2	9/2007	Yun et al.	
7,286,640	B2	10/2007	Yun et al.	
7,297,959	B2	11/2007	Yun et al.	
7,298,826	B2	11/2007	Inazuru	
7,330,533	B2	2/2008	Sampayon	
7,346,148	B2	3/2008	Ukita	
7,346,204	B2	3/2008	Ito	
7,349,525	B2	3/2008	Morton	
7,359,487	B1	4/2008	Newcome	
7,365,909	B2	4/2008	Yun et al.	
7,365,918	B1	4/2008	Yun et al.	
7,382,864	B2	6/2008	Hebert et al.	
7,388,942	B2	6/2008	Wang et al.	
7,394,890	B1	7/2008	Wang et al.	
7,400,704	B1	7/2008	Yun et al.	
7,406,151	B1	7/2008	Yun	
7,412,024	B1	8/2008	Yun et al.	
7,412,030	B1	8/2008	O'Hara	
7,412,131	B2	8/2008	Lee et al.	
7,414,787	B2	8/2008	Yun et al.	
7,433,444	B2	10/2008	Baumann	
7,440,542	B2	10/2008	Baumann	
7,443,953	B1	10/2008	Yun et al.	
7,443,958	B2	10/2008	Harding	
7,453,981	B2	11/2008	Baumann	
7,463,712	B2	12/2008	Zhu et al.	
7,474,735	B2 *	1/2009	Spahn	G21K 1/025 378/155
7,486,770	B2	2/2009	Baumann	
7,492,871	B2	2/2009	Popescu	
7,499,521	B2	3/2009	Wang et al.	
7,515,684	B2	4/2009	Gibson et al.	
7,522,698	B2	4/2009	Popescu	
7,522,707	B2	4/2009	Steinlage et al.	
7,522,708	B2	4/2009	Heismann	
7,529,343	B2	5/2009	Safai et al.	
7,532,704	B2	5/2009	Hempel	
7,551,719	B2	6/2009	Yokhin et al.	
7,551,722	B2	6/2009	Ohshima et al.	
7,561,662	B2	7/2009	Wang et al.	
7,564,941	B2	7/2009	Baumann	
7,583,789	B1	9/2009	Macdonald et al.	
7,601,399	B2	10/2009	Barnola et al.	
7,605,371	B2	10/2009	Yasui et al.	
7,639,786	B2	12/2009	Baumann	
7,646,843	B2	1/2010	Popescu et al.	
7,672,433	B2	3/2010	Zhong et al.	
7,680,243	B2	3/2010	Yokhin et al.	
7,738,629	B2	6/2010	Chen	
7,787,588	B1	8/2010	Yun et al.	
7,796,725	B1	9/2010	Yun et al.	
7,796,726	B1	9/2010	Gendreau et al.	
7,800,072	B2	9/2010	Yun et al.	
7,809,113	B2	10/2010	Aoki et al.	
7,813,475	B1	10/2010	Wu et al.	
7,817,777	B2	10/2010	Baumann et al.	
7,848,483	B2	12/2010	Platonov	
7,864,426	B2	1/2011	Yun et al.	
7,864,922	B2	1/2011	Kawabe	
7,873,146	B2	1/2011	Okunuki et al.	
7,876,883	B2	1/2011	O'Hara	
7,889,838	B2	2/2011	David et al.	
7,889,844	B2	2/2011	Okunuki et al.	
7,899,154	B2	3/2011	Chen et al.	
7,902,528	B2	3/2011	Hara et al.	
7,914,693	B2	3/2011	Jeong et al.	
7,920,673	B2	4/2011	Lanza et al.	
7,920,676	B2	4/2011	Yun et al.	
7,924,973	B2	4/2011	Kottler et al.	
7,929,667	B1	4/2011	Zhuang et al.	
7,945,018	B2	5/2011	Heismann	
7,949,092	B2	5/2011	Brons	
7,949,095	B2	5/2011	Ning	
7,974,379	B1	7/2011	Case et al.	
7,983,381	B2	7/2011	David et al.	
7,991,120	B2	8/2011	Okunuki et al.	
8,005,185	B2	8/2011	Popescu	
8,009,796	B2	8/2011	Popescu	
8,009,797	B2	8/2011	Ouchi	
8,041,004	B2	10/2011	David	
8,036,341	B2	11/2011	Lee	
8,058,621	B2	11/2011	Kommareddy	
8,068,579	B1	11/2011	Yun et al.	
8,073,099	B2	12/2011	Niu et al.	
8,094,784	B2	1/2012	Morton	
8,139,711	B2	3/2012	Takahashi	
8,139,716	B2	3/2012	Okunuki et al.	
8,184,771	B2	5/2012	Murakoshi	
8,208,602	B2	6/2012	Lee	
8,208,603	B2	6/2012	Sato	
8,233,587	B2	7/2012	Sato	
8,243,879	B2	8/2012	Itoh et al.	
8,243,884	B2	8/2012	Rödhammer et al.	
8,249,220	B2	8/2012	Verman et al.	
8,280,000	B2	10/2012	Takahashi	
8,306,183	B2	11/2012	Koehler	
8,306,184	B2	11/2012	Chang et al.	
8,331,534	B2	12/2012	Silver	
8,351,569	B2	1/2013	Baker	
8,351,570	B2	1/2013	Nakamura	
8,353,628	B1	1/2013	Yun et al.	
8,357,894	B2	1/2013	Toth et al.	
8,360,640	B2	1/2013	Reinhold	
8,374,309	B2	2/2013	Donath	
8,406,378	B2	3/2013	Wang et al.	
8,416,920	B2	4/2013	Okumura et al.	
8,422,633	B2	4/2013	Lantz et al.	
8,423,127	B2	4/2013	Mahmood et al.	
8,451,975	B2	5/2013	Tada	
8,422,637	B2	6/2013	Okunuki et al.	
8,488,743	B2	7/2013	Verman	
8,509,386	B2	8/2013	Lee et al.	
8,520,803	B2	8/2013	Behling	
8,526,575	B1	9/2013	Yun et al.	
8,532,257	B2	9/2013	Mukaide et al.	
8,553,843	B2	10/2013	Drory	
8,559,594	B2	10/2013	Ouchi	
8,559,597	B2	10/2013	Chen et al.	
8,565,371	B2	10/2013	Bredno	
8,576,983	B2	11/2013	Baeumer	
8,588,372	B2	11/2013	Zou et al.	
8,591,108	B2	11/2013	Tada	
8,602,648	B1	12/2013	Jacobsen et al.	
8,632,247	B2	1/2014	Ishii	
8,644,451	B2	2/2014	Aoki et al.	
8,666,024	B2	3/2014	Okunuki et al.	
8,666,025	B2	3/2014	Klausz	
8,699,667	B2	4/2014	Steinlage et al.	
8,735,844	B1	5/2014	Khaykovich et al.	
8,737,565	B1	5/2014	Lyon et al.	
8,744,048	B2	6/2014	Lee et al.	
8,755,487	B2	6/2014	Kaneko	
8,767,915	B2	7/2014	Stutman	
8,767,916	B2	7/2014	Hashimoto	
8,781,069	B2	7/2014	Murakoshi	
8,824,629	B2	9/2014	Ishii	
8,831,174	B2	9/2014	Kohara	
8,831,175	B2	9/2014	Silver et al.	
8,831,179	B2	9/2014	Adler et al.	
8,837,680	B2	9/2014	Tsujii	
8,855,265	B2	10/2014	Engel	
8,859,977	B2	10/2014	Kondoh	
8,861,682	B2	10/2014	Okunuki et al.	
8,903,042	B2	12/2014	Ishii	
8,908,824	B2	12/2014	Kondoh	
8,972,191	B2	3/2015	Stampanoni et al.	
8,989,351	B2	3/2015	Vogtmeier et al.	
8,989,474	B2	3/2015	Kido et al.	
8,995,622	B2	3/2015	Adler et al.	
9,001,967	B2	4/2015	Baturin	
9,001,968	B2	4/2015	Kugland et al.	
9,007,562	B2	4/2015	Marconi et al.	
9,008,278	B2	4/2015	Lee et al.	
9,016,943	B2	4/2015	Jacobsen et al.	

(56) **References Cited**

U.S. PATENT DOCUMENTS

9,020,101	B2	4/2015	Omote et al.	
9,025,725	B2	5/2015	Kiyohara et al.	
9,029,795	B2	5/2015	Sando	
9,031,201	B2	5/2015	Sato	
9,063,055	B2	6/2015	Ouchi	
9,086,536	B2	7/2015	Pang et al.	
9,129,715	B2	9/2015	Adler et al.	
9,222,899	B2	12/2015	Yamaguchi	
9,234,856	B2	1/2016	Mukaide	
9,251,995	B2	2/2016	Ogura	
9,257,254	B2	2/2016	Ogura et al.	
9,263,225	B2	2/2016	Morton	
9,280,056	B2	3/2016	Clube et al.	
9,281,158	B2	3/2016	Ogura	
9,291,578	B2	3/2016	Adler	
9,329,141	B2	5/2016	Stutman	
9,336,917	B2	5/2016	Ozawa et al.	
9,357,975	B2	6/2016	Baturin	
9,362,081	B2	6/2016	Bleuet	
9,370,084	B2	6/2016	Sprong et al.	
9,390,881	B2	7/2016	Yun et al.	
9,412,552	B2	8/2016	Aoki et al.	
9,430,832	B2	8/2016	Koehler et al.	
9,439,613	B2	9/2016	Stutman	
9,445,775	B2	9/2016	Das	
9,448,190	B2	9/2016	Yun et al.	
9,449,780	B2	9/2016	Chen	
9,449,781	B2	9/2016	Yun et al.	
9,453,803	B2	9/2016	Radicke	
9,486,175	B2	11/2016	Fredenberg et al.	
9,494,534	B2	11/2016	Baturin	
9,502,204	B2	11/2016	Ikarashi	
9,520,260	B2	12/2016	Hesselink et al.	
9,524,846	B2	12/2016	Sato et al.	
9,532,760	B2	1/2017	Anton et al.	
9,543,109	B2	1/2017	Yun et al.	
9,564,284	B2	2/2017	Gerzoskovitz	
9,570,264	B2	2/2017	Ogura et al.	
9,570,265	B1	2/2017	Yun et al.	
9,588,066	B2	3/2017	Pois et al.	
9,594,036	B2	3/2017	Yun et al.	
9,595,415	B2	3/2017	Ogura	
9,632,040	B2	4/2017	Stutman	
9,658,174	B2	5/2017	Omote	
9,700,267	B2	7/2017	Baturin et al.	
9,719,947	B2 *	8/2017	Yun	G01N 23/20075
9,748,012	B2	8/2017	Yokoyama	
9,757,081	B2	9/2017	Proksa	
9,761,021	B2	9/2017	Koehler	
9,770,215	B2 *	9/2017	Souchay	A61B 6/06
9,823,203	B2	11/2017	Yun et al.	
9,826,949	B2	11/2017	Ning	
9,837,178	B2	12/2017	Nagai	
9,842,414	B2	12/2017	Koehler	
9,861,330	B2	1/2018	Rossl	
9,874,531	B2 *	1/2018	Yun	H01J 35/08
9,881,710	B2	1/2018	Roessl	
9,916,655	B2	3/2018	Sampanoni	
9,934,930	B2	4/2018	Parker et al.	
9,939,392	B2	4/2018	Wen	
9,970,119	B2	5/2018	Yokoyama	
10,014,148	B2	7/2018	Tang et al.	
10,020,158	B2	7/2018	Yamada	
10,028,716	B2	7/2018	Rossl	
10,045,753	B2	8/2018	Teshima	
10,068,740	B2	9/2018	Gupta	
10,074,451	B2	9/2018	Kottler et al.	
10,076,297	B2	9/2018	Bauer	
10,085,701	B2	10/2018	Hoshino	
10,105,112	B2	10/2018	Utsumi	
10,115,557	B2	10/2018	Ishii	
10,141,081	B2	11/2018	Preusche	
10,151,713	B2	12/2018	Wu et al.	
10,153,061	B2	12/2018	Yokoyama	
10,153,062	B2	12/2018	Gall et al.	
10,182,194	B2	1/2019	Karim et al.	
10,217,596	B2	2/2019	Liang et al.	
10,231,687	B2	3/2019	Kahn et al.	
10,247,683	B2	4/2019	Yun et al.	
10,256,001	B2	4/2019	Yokoyama	
10,264,659	B1	4/2019	Miller et al.	
10,267,752	B2	4/2019	Zhang et al.	
10,267,753	B2	4/2019	Zhang et al.	
10,269,528	B2	4/2019	Yun et al.	
10,295,485	B2	5/2019	Yun et al.	
10,295,486	B2	5/2019	Yun et al.	
10,297,359	B2	5/2019	Yun et al.	
10,304,580	B2 *	5/2019	Yun	G21K 7/00
10,349,908	B2 *	7/2019	Yun	G01N 23/046
10,352,695	B2	7/2019	Dziura et al.	
10,352,880	B2 *	7/2019	Yun	A61B 6/4007
10,393,683	B2	8/2019	Hegeman et al.	
10,401,309	B2 *	9/2019	Yun	H01J 35/08
10,416,099	B2	9/2019	Yun et al.	
10,429,325	B2	10/2019	Ito et al.	
10,466,185	B2 *	11/2019	Yun	G01N 23/223
10,653,376	B2 *	5/2020	Yun	A61B 6/508
2001/0006413	A1	7/2001	Burghoorn	
2002/0080916	A1	6/2002	Jiang	
2002/0085676	A1	7/2002	Snyder	
2003/0142790	A1	1/2003	Zhou et al.	
2003/0054133	A1	3/2003	Wadley et al.	
2003/0112923	A1	6/2003	Lange	
2003/0223536	A1	12/2003	Yun et al.	
2004/0047446	A1	3/2004	Platonov	
2004/0076260	A1 *	4/2004	Charles, Jr.	H01J 35/18 378/124
2004/0120463	A1	6/2004	Wilson et al.	
2004/0140432	A1	7/2004	Maldonado et al.	
2005/0025281	A1	2/2005	Verman et al.	
2005/0074094	A1	4/2005	Jen et al.	
2005/0123097	A1	6/2005	Wang	
2005/0163284	A1	7/2005	Inazuru	
2005/0282300	A1	12/2005	Yun et al.	
2006/0045234	A1	3/2006	Pelc	
2006/0062350	A1	3/2006	Yokhin	
2006/0182322	A1 *	8/2006	Bernhardt	A61B 5/02007 382/128
2006/0233309	A1	10/2006	Kutzner et al.	
2006/0239405	A1	10/2006	Verman	
2007/0030959	A1	2/2007	Ritter	
2007/0071174	A1	3/2007	Hebert et al.	
2007/0108387	A1	5/2007	Yun et al.	
2007/0110217	A1	5/2007	Ukita	
2007/0183563	A1	8/2007	Baumann	
2007/0183579	A1	8/2007	Baumann et al.	
2007/0189449	A1	8/2007	Baumann	
2007/0248215	A1	10/2007	Ohshima et al.	
2008/0084966	A1	4/2008	Aoki et al.	
2008/0089484	A1	4/2008	Reinhold	
2008/0094694	A1	4/2008	Yun et al.	
2008/0099935	A1	5/2008	Egle	
2008/0116398	A1	5/2008	Hara	
2008/0117511	A1	5/2008	Chen	
2008/0159707	A1	7/2008	Lee et al.	
2008/0165355	A1	7/2008	Yasui et al.	
2008/0170662	A1	7/2008	Reinhold	
2008/0170668	A1	7/2008	Kruit et al.	
2008/0181363	A1	7/2008	Fenter et al.	
2008/0240344	A1	10/2008	Reinhold	
2008/0273662	A1	11/2008	Yun	
2009/0052619	A1	2/2009	Endoh	
2009/0092227	A1 *	4/2009	David	A61B 6/4291 378/36
2009/0154640	A1	6/2009	Baumann et al.	
2009/0316860	A1	12/2009	Okunuki et al.	
2010/0012845	A1	1/2010	Baeumer et al.	
2010/0027739	A1	2/2010	Lantz et al.	
2010/0040202	A1	2/2010	Lee	
2010/0046702	A1	2/2010	Chen et al.	
2010/0061508	A1	3/2010	Takahashi	
2010/0091947	A1	4/2010	Niu	
2010/0141151	A1	6/2010	Reinhold	
2010/0246765	A1	9/2010	Murakoshi	

(56) References Cited

U.S. PATENT DOCUMENTS

2010/0260315	A1	10/2010	Sato et al.	
2010/0272239	A1	10/2010	Lantz et al.	
2010/0284513	A1	11/2010	Kawabe	
2011/0026680	A1	2/2011	Sato	
2011/0038455	A1	2/2011	Silver et al.	
2011/0058655	A1	3/2011	Okumura et al.	
2011/0064191	A1	3/2011	Toth et al.	
2011/0085644	A1	4/2011	Verman	
2011/0135066	A1	6/2011	Behling	
2011/0142204	A1	6/2011	Zou et al.	
2011/0235781	A1	9/2011	Aoki et al.	
2011/0243302	A1	10/2011	Murakoshi	
2011/0268252	A1	11/2011	Ozawa et al.	
2012/0041679	A1*	2/2012	Stampanoni	A61B 6/484 702/1
2012/0057669	A1	3/2012	Vogtmeier et al.	
2012/0163547	A1	6/2012	Lee et al.	
2012/0163554	A1*	6/2012	Tada	A61B 6/4291 378/154
2012/0224670	A1	9/2012	Kiyohara et al.	
2012/0228475	A1	9/2012	Pang et al.	
2012/0269323	A1	10/2012	Adler et al.	
2012/0269324	A1	10/2012	Adler	
2012/0269325	A1	10/2012	Adler et al.	
2012/0269326	A1	10/2012	Adler et al.	
2012/0294420	A1	11/2012	Nagai	
2013/0011040	A1	1/2013	Kido et al.	
2013/0032727	A1	2/2013	Kondoe	
2013/0039460	A1	2/2013	Levy	
2013/0108012	A1	5/2013	Sato	
2013/0108022	A1	5/2013	Kugland et al.	
2013/0195246	A1	8/2013	Tamura et al.	
2013/0223594	A1	8/2013	Sprong et al.	
2013/0235976	A1	9/2013	Jeong et al.	
2013/0259207	A1	10/2013	Omote et al.	
2013/0279651	A1	10/2013	Yokoyama	
2013/0308112	A1	11/2013	Clube et al.	
2013/0308754	A1	11/2013	Yamazaki et al.	
2014/0023973	A1	1/2014	Marconi et al.	
2014/0037052	A1	2/2014	Adler	
2014/0064445	A1	3/2014	Adler	
2014/0072104	A1	3/2014	Jacobsen et al.	
2014/0079188	A1	3/2014	Hesselink et al.	
2014/0105363	A1	4/2014	Chen et al.	
2014/0146945	A1	5/2014	Fredenberg et al.	
2014/0153692	A1	6/2014	Larkin et al.	
2014/0177800	A1	6/2014	Sato et al.	
2014/0185778	A1	7/2014	Lee et al.	
2014/0205057	A1	7/2014	Koehler et al.	
2014/0211919	A1	7/2014	Ogura et al.	
2014/0226785	A1	8/2014	Stutman et al.	
2014/0241493	A1	8/2014	Yokoyama	
2014/0270060	A1	9/2014	Date et al.	
2014/0369469	A1	12/2014	Ogura et al.	
2015/0030126	A1	1/2015	Radicke	
2015/0030127	A1	1/2015	Aoki et al.	
2015/0043713	A1	2/2015	Chen	
2015/0049860	A1	2/2015	Das	
2015/0055743	A1	2/2015	Vedantham et al.	
2015/0055745	A1	2/2015	Holzner et al.	
2015/0071402	A1	3/2015	Handa	
2015/0092924	A1	4/2015	Yun et al.	
2015/0110252	A1	4/2015	Yun et al.	
2015/0117599	A1	4/2015	Yun et al.	
2015/0194287	A1	7/2015	Yun et al.	
2015/0243397	A1	8/2015	Yun et al.	
2015/0247811	A1	9/2015	Yun et al.	
2015/0260663	A1	9/2015	Yun et al.	
2015/0323478	A1	11/2015	Stutman	
2015/0357069	A1	12/2015	Yun et al.	
2016/0064175	A1	3/2016	Yun et al.	
2016/0066870	A1	3/2016	Yun et al.	
2016/0106387	A1	4/2016	Kahn	
2016/0178540	A1	6/2016	Yun et al.	
2016/0178541	A1	6/2016	Hwang et al.	
2016/0206259	A1*	7/2016	Auclair	A61B 6/502
2016/0268094	A1	9/2016	Yun et al.	
2016/0320320	A1	11/2016	Yun et al.	
2016/0351370	A1	12/2016	Yun et al.	
2017/0018392	A1	1/2017	Cheng	
2017/0047191	A1	2/2017	Yun et al.	
2017/0052128	A1	2/2017	Yun et al.	
2017/0074809	A1	3/2017	Ito	
2017/0162288	A1	6/2017	Yun et al.	
2017/0162359	A1	6/2017	Tang et al.	
2017/0227476	A1	8/2017	Zhang et al.	
2017/0234811	A1	8/2017	Zhang et al.	
2017/0261442	A1	9/2017	Yun et al.	
2017/0336334	A1	11/2017	Yun et al.	
2018/0144901	A1	5/2018	Yun et al.	
2018/0202951	A1	7/2018	Yun et al.	
2018/0261352	A1	9/2018	Matsuyama et al.	
2018/0306734	A1	10/2018	Morimoto et al.	
2018/0323032	A1	11/2018	Strelec et al.	
2018/0344276	A1	12/2018	DeFreitas et al.	
2018/0348151	A1	12/2018	Kasper et al.	
2018/0356355	A1	12/2018	Momose et al.	
2019/0017942	A1	1/2019	Filevich	
2019/0017946	A1	1/2019	Wack et al.	
2019/0018824	A1	1/2019	Zarkadas	
2019/0019647	A1	1/2019	Lee et al.	
2019/0027265	A1	1/2019	Dey et al.	
2019/0043689	A1	2/2019	Camus	
2019/0057832	A1	2/2019	Durst et al.	
2019/0064084	A1	2/2019	Ullom et al.	
2019/0086342	A1	3/2019	Pois et al.	
2019/0088439	A1	3/2019	Honda	
2019/0113466	A1	4/2019	Karim et al.	
2019/0115184	A1	4/2019	Zalubovsky	
2019/0131103	A1	5/2019	Tuohimaa	
2019/0132936	A1	5/2019	Steck et al.	
2019/0154892	A1	5/2019	Moldovan	
2019/0172681	A1	6/2019	Owen et al.	
2019/0189385	A1	6/2019	Liang et al.	
2019/0204246	A1	7/2019	Hegeman et al.	
2019/0204757	A1	7/2019	Brussard et al.	
2019/0206652	A1	7/2019	Akinwande et al.	
2019/0212281	A1	7/2019	Shchgegrov	
2019/0214216	A1	7/2019	Jeong et al.	
2019/0216416	A1	7/2019	Koehler et al.	
2019/0219713	A1	7/2019	Booker et al.	
2019/0261935	A1	8/2019	Kitamura	
2019/0272929	A1	9/2019	Omote et al.	
2019/0304735	A1	10/2019	Safai et al.	
2019/0311874	A1	10/2019	Tuohimma et al.	
2019/0317027	A1	10/2019	Tsuboi et al.	
2019/0341219	A1	11/2019	Zhang et al.	
2019/0341220	A1	11/2019	Parker et al.	
2019/0353802	A1	11/2019	Steinhauser et al.	
2019/0374182	A1	12/2019	Karim et al.	
2019/0380193	A1	12/2019	Matsuhana et al.	
2019/0387602	A1	12/2019	Woywode et al.	
2019/0391087	A1	12/2019	Matejka et al.	
2020/0003708	A1	1/2020	Kobayashi et al.	
2020/0003712	A1	1/2020	Kataoka et al.	
2020/0041429	A1	2/2020	Cho et al.	
2020/0058462	A1	2/2020	Suzuki	
2020/0088656	A1	3/2020	Pois et al.	
2020/0090826	A1	3/2020	Adler	
2020/0103358	A1	4/2020	Wiell et al.	
2020/0105492	A1	4/2020	Behling et al.	

FOREIGN PATENT DOCUMENTS

CN	102124537	A	7/2011
CN	102325498		1/2012
CN	102551761	A	7/2012
EP	0432568		6/1991
EP	0751533		1/1997
EP	1028451		8/2000
EP	1169713		1/2006
EP	3093867	A1	11/2016
FR	2548447		1/1985
JP	H06-188092		7/1994

(56) References Cited

FOREIGN PATENT DOCUMENTS

JP	H07-056000		3/1995
JP	H07-194592		8/1995
JP	H08-184572		7/1996
JP	H11-304728		11/1999
JP	2000-306533		11/2000
JP	2003-149392		5/2003
JP	2003-288853		10/2003
JP	2004-089445		3/2004
JP	2007-218683		8/2007
JP	2007-265981		10/2007
JP	2007-311185		11/2007
JP	2008-200359		4/2008
JP	2008-200359	A	4/2008
JP	2008-145111		6/2008
JP	2008-197495		8/2008
JP	2009-195349		3/2009
JP	2009-212058		9/2009
JP	2010-236986		10/2010
JP	2011-029072		2/2011
JP	2011-218147		11/2011
JP	2012-032387		2/2012
JP	2012-187341		10/2012
JP	2012-254294		12/2012
JP	2013-508683		3/2013
JP	2013-157269		8/2013
JP	2013-160637		8/2013
JP	2013-181811		9/2013
JP	2013-239317		11/2013
JP	2015-002074		1/2015
JP	2015-047306		3/2015
JP	2015-072263		4/2015
JP	2015-077289		4/2015
KR	10-2012-0091591	A	8/2012
WO	WO 1995/006952		3/1995
WO	WO 1998/011592		3/1998
WO	WO 2002/039792		5/2002
WO	WO 2003/081631		10/2003
WO	WO 2005/109969		11/2005
WO	WO 2006/096052		9/2006
WO	WO 2007/125833		11/2007
WO	WO 2009/098027		8/2009
WO	WO 2009/1104560		8/2009
WO	WO 2010/109909		9/2010
WO	WO 2011/032572		3/2011
WO	WO 2012/032950		3/2012
WO	WO 2013/004574		1/2013
WO	WO 2013/111050		8/2013
WO	WO 2013/118593		8/2013
WO	WO 2013/160153		10/2013
WO	WO 2013/168468		11/2013
WO	WO 2014/054497		4/2014
WO	WO 2015/016019		2/2015
WO	WO 2015/034791		3/2015
WO	WO 2015/066333		5/2015
WO	WO 2015/084466		6/2015
WO	WO 2015/168473		11/2015
WO	WO 2015/176023		11/2015
WO	WO 2015/187219		12/2015
WO	WO 2016/187623		11/2016
WO	WO 2017/031740		3/2017
WO	WO 2017/204850		11/2017
WO	WO 2017/213996		12/2017
WO	WO 2018/122213		7/2018
WO	WO 2018/175570		9/2018

OTHER PUBLICATIONS

"Element Six CVD Diamond Handbook" (Element Six, Luxembourg, 2015).

"High performance benchtop EDXRF spectrometer with Windows® software," published by: Rigaku Corp., Tokyo, Japan; 2017.

"Monochromatic Doubly Curved Crystal Optics," published by: X-Ray Optical Systems, Inc. (XOS), East Greenbush, NY; 2017.

"Optics and Detectors," Section 4 of X-Ray Data Booklet, 3rd Ed., A.C. Thompson ed. (Lawrence Berkeley Nat'l Lab, Berkeley, CA, 2009).

"Properties of Solids," Ch. 12 of CRC Handbook of Chemistry and Physics, 90th ed., Devid R. Lide & W.M. "Mickey" Haynes, eds. (CRC Press, Boca Raton, FL, 2009), pp. 12-41-12-46; 12-203-12-212.

"Science and Technology of Future Light Sources", Arthur L. Robinson (LBNL) and Brad Plummer (SLAG), eds. Report Nos. ANL-08/39 / BNL-81895-2008 / LBNL-1090E-2009 / SLAC-R-917 (Lawrence Berkeley Nat'l Lab, Berkeley, CA, Dec. 2008).

"Series 5000 Packaged X-ray Tubes," Product Technical Data Sheet DS006 Rev. G, X-Ray Technologies Inc. (Oxford Instruments), Scotts Valley, CA (no date).

"Toward Control of Matter: Energy Science Needs for a New Class of X-Ray Light Sources" (Lawrence Berkeley Nat'l Lab, Berkeley, CA, Sep. 2008).

"X-ray Optics for BES Light Source Facilities," Report of the Basic Energy Sciences Workshop on X-ray Optics for BES Light Source Facilities, D. Mills & H. Padmore, Co-Chairs, (U.S. Dept. of Energy, Office of Science, Potomac, MD, Mar. 2013).

Abullian et al., "Quantitative determination of the lateral density and intermolecular correlation between proteins anchored on the membrane surfaces using grazing incidence small-angle X-ray scattering and grazing incidence X-ray fluorescence," Nov. 28, 2012, The Journal of Chemical Physics, vol. 137, pp. 204907-1 to 204907-8.

Adachi et al., "Development of the 17-inch Direct-Conversion Dynamic Flat-panel X-ray Detector (FPD)," Digital R/F (Shimadzu Corp., 2 pages. (no date, published -2004 with product release).

Aharonovich et al., "Diamond Nanophotonics," Adv. Op. Man's vol. 2, Issue 10 (2014).

Als-Nielsen et al., "Phase contrast imaging" Sect. 9.3 of Ch. 9 of "Elements of Modern X-ray Physics, Second Edition", (John Wiley & Sons Ltd, Chichester, West Sussex, UK, 2011), pp. 318-329.

Als-Nielsen et al., "Photoelectric Absorption," Ch. 7 of "Elements of Modern X-ray Physics, Second Edition," (John Wiley & Sons Ltd, Chichester, West Sussex, UK, 2011).

Als-Nielsen et al., "Refraction and reflection from interfaces," Ch. 3 of "Elements of Modern X-ray Physics, Second Edition," (John Wiley & Sons Ltd., Chichester, West Sussex, UK, 2011), pp. 69-112.

Als-Nielsen et al., "X-rays and their interaction with matter", and "Sources", Ch. 1 & 2 of "Elements of Modern X-ray Physics, Second Edition" (John Wiley & Sons Ltd, Chichester, West Sussex, UK, 2011).

Altapova et al., "Phase contrast laminography based on Talbot interferometry," Opt. Express, vol. 20, No. 6, (2012) pp. 6496-6508.

Ando et al., "Smooth and high-rate reactive ion etching of diamond," Diamond and Related Materials, vol. 11, (2002) pp. 824-827.

Arfelli et al., "Mammography with Synchrotron Radiation: Phase-Detection Techniques," Radiology vol. 215, (2000), pp. 286-293.

Arndt et al., Focusing Mirrors for Use with Microfocus X-ray Tubes, 1998, Journal of Applied Crystallography, vol. 31, pp. 733-741.

Bachucki et al., "Laboratory-based double X-ray spectrometer for simultaneous X-ray emission and X-ray absorption studies," J. Anal. Atomic Spectr. DOI:10.1039/C9JA00159J (2019).

Balaic et al., "X-ray optics of tapered capillaries," Appl. Opt. vol. 34 (Nov. 1995) pp. 7263-7272.

Baltes et al., "Coherent and incoherent grating reconstruction," J. Opt. Soc. Am. A vol. 3(8), (1986), pp. 1268-1275.

Barbee Jr., "Multilayers for x-ray optics," Opt. Eng. vol. 25 (Aug. 1986) pp. 898-915.

Baron et al., "A compact optical design for Bragg reflections near backscattering," J. Synchrotron Rad., vol. 8 (2001), pp. 1127-1130.

Bech, "In-vivo dark-field and phase-contrast x-ray imaging," Scientific Reports 3, (2013), Article No. 03209.

Bech, "X-ray imaging with a grating interferometer," University of Copenhagen PhD. Thesis, (May 1, 2009).

(56) References Cited

OTHER PUBLICATIONS

Bergamin et al., "Measuring small lattice distortions in Si-crystals by phase-contrast x-ray topography," J. Phys. D: Appl. Phys. vol. 33 (Dec. 31, 2000) pp. 2678-2682.

Bernstorff, "Grazing Incidence Small Angle X-ray Scattering (GISAXS)," Presentation at Advanced School on Synchrotron and Free Electron Laser Sources and their Multidisciplinary Applications, Apr. 2008, Trieste, Italy.

Bilderback et al., "Single Capillaries," Ch. 29 of "Handbook of Optics vol. III, 2nd Ed." (McGraw Hill, New York, 2001).

Birkholz, "Chapter 4: Grazing Incidence Configurations," Thin Film Analysis by X-ray Scattering (Wiley-VCH Verlag GmbH & Co. KGaA, Weinheim, Germany, 2006).

Bjeoumikhov et al., "A modular system for XRF and XRD applications consisting of a microfocus X-ray source and different capillary optics," X-ray Spectrometry, vol. 33 (2004), pp. 312-316.

Bjeoumikhov et al., "Capillary Optics for X-Rays," Ch. 18 of "Modern Developments in X-Ray and Neutron Optics," A. Erko et al., eds. (Springer, Berlin, Germany, 2008), pp. 287-306.

Canberra Model S-5005 WinAxil X-Ray Analysis Software, published by: Canberra Eurisys Benelux N.V./S.A.,Zellik, Belgium; Jun. 2004.

Cerrina, "The Schwarzschild Objective," Ch. 27 of "Handbook of Optics vol. III, 2nd Ed." (McGraw Hill, New York, 2001).

Chen et al., "Advance in detection of low sulfur content by wavelength dispersive XRF," Proceedings of the Annual ISA Analysis Division Symposium (2002).

Chen et al., "Doubly curved crystal (DCC) X-ray optics and applications," Powder Diffraction, vol. 17(2) (2002), pp. 99-103.

Chen et al., "Guiding and focusing neutron beams using capillary optics," Nature vol. 357 (Jun. 4, 1992), pp. 391-393.

Chervenak et al., "Experimental thick-target bremsstrahlung spectra from electrons in the range 10 to 30 keV", Phys. Rev. A vol. 12 (1975), pp. 26-33.

Chon, "Measurement of Roundness for an X-Ray Mono-Capillary Optic by Using Computed Tomography," J. Korean Phys. Soc. vol. 74, No. 9, pp. 901-906 (May 2019).

Coan et al., "In vivo x-ray phase contrast analyzer-based imaging for longitudinal osteoarthritis studies in guinea pigs," Phys. Med. Biol. vol. 55(24) (2010), pp. 7649-7662.

Cockcroft et al., "Chapter 2: Experimental Setups," Powder Diffraction: Theory and Practice, R.E. Dinnebier and S.J.L. Billinge, eds (Royal Society of Chemistry Publishing, London, UK, 2008).

Cohen et al., "Tunable laboratory extended x-ray absorption fine structure system," Rev. Sci. Instr. vol. 51, No. 3, Mar. 1980, pp. 273-277.

Cong et al., "Fourier transform-based iterative method for differential phase-contrast computed tomography", Opt. Lett. vol. 37 (2012), pp. 1784-1786.

Cornaby et al., "Advances in X-ray Microfocusing with Monocapillary Optics at CHESS," CHESS News Magazine (2009), pp. 63-66.

Cornaby et al., "Design of Single-Bounce Monocapillary X-ray Optics," Advances in X-ray Analysis: Proceedings of the 55th Annual Conference on Applications of X-ray Analysis, vol. 50, (International Centre for Diffraction Data (ICDD), 2007), pp. 194-200.

Cornaby, "The Handbook of X-ray Single Bounce Monocapillary Optics, Including Optical Design and Synchrotron Applications" (PhD Dissertation, Cornell University, Ithaca, NY, May 2008).

David et al., "Fabrication of diffraction gratings for hard x-ray phase contrast imaging," Microelectron. Eng. vol. 84, (2007), pp. 1172-1177.

David et al., "Hard X-ray phase imaging and tomography using a grating interferometer," Spectrochimica Acta Part B vol. 62 (2007) pp. 626-630.

Davis et al., "Bridging the Micro-to-Macro Gap: A New Application for Micro X-Ray Fluorescence," Microsc Microanal., vol. 17(3) (Jun. 2011), pp. 410-417.

Diaz et al., "Monte Carlo Simulation of Scatter Field for Calculation of Contrast of Discs in Synthetic CDMAM Images," in: Digital Mammography, Proceedings 10th International Workshop IWDM 2010 (Springer Verlag, Berlin Heidelberg), (2010), pp. 628-635 (9 pages). Jun. 18, 2010.

Ding et al., "Reactive Ion Etching of CVD Diamond Films for MEMS Applications," Micromachining and Microfabrication, Proc. SPIE vol. 4230 (2000), pp. 224-230.

Dobrovinskaya et al., "Thermal Properties," Sect. 2.1.5 of "Sapphire: Material, Manufacturing, Applications" (Springer Science + Business Media, New York, 2009).

Dong et al., "Improving Molecular Sensitivity in X-Ray Fluorescence Molecular Imaging (XFMI) of Iodine Distribution in Mouse-Sized Phantoms via Excitation Spectrum Optimization," IEEE Access, vol. 6, pp. 56966-56976 (2018).

Erko et al., "X-ray Optics," Ch. 3 of "Handbook of Practical X-Ray Fluorescence Analysis," B. Beckhoff et al., eds. (Springer, Berlin, Germany, 2006), pp. 85-198.

Falcone et al., "New directions in X-ray microscopy," Contemporary Physics, vol. 52, No. 4, (Jul.-Aug. 2010), pp. 293-318.

Fernández-Ruiz, "TXRF Spectrometry as a Powerful Tool for the Study of Metallic Traces in Biological Systems," Development in Analytical Chemistry, vol. 1 (2014), pp. 1-14.

Freund, "Mirrors for Synchrotron Beamlines," Ch. 26 of "Handbook of Optics vol. III, 2nd Ed." (McGraw Hill, New York, 2001).

Ge et al., "Investigation of the partially coherent effects in a 2D Talbot interferometer," Anal. Bioanal. Chem. vol. 401, (2011), pp. 865-870. Apr. 29, 2011 pub Jun. 14, 2011.

Gibson et al., "Polycapillary Optics: An Enabling Technology for New Applications," Advances in X-ray Analysis, vol. 45 (2002), pp. 286-297.

Gonzales et al., "Angular Distribution of Bremsstrahlung Produced by 10-Kev and 20 Kev Electrons Incident On A Thick Au Target", in Application of Accelerators in Research and Industry, AIP Conf. Proc. 1221 (2013), pp. 114-117.

Gonzales et al., "Angular distribution of thick-target bremsstrahlung produced by electrons with initial energies ranging from 10 to 20 keV incident on Ag", Phys. Rev. A vol. 84 (2011): 052726.

Günther et al., "Full-field structured-illumination super-responution X-ray transmission microscopy," Nature Comm. 10:2494 (2019) and supplementary information.

Guttmann et al., "Ellipsoidal capillary as condenser for the Bessy full-field x-ray microscope," J. Phys. Conf. Ser. vol. 186 (2009): 012064.

Harasse et al., "Iterative reconstruction in x-ray computed laminography from differential phase measurements", Opt. Express. vol. 19 (2011), pp. 16560-16573.

Harasse et al., "X-ray Phase Laminography with a Grating Interferometer using Iterative Reconstruction", in International Workshop on X-ray and Neutron Phase Imaging with Gratings, AIP Conf. Proc. vol. 1466, (2012), pp. 163-168.

Harasse et al., "X-ray Phase Laminography with Talbot Interferometer", in Developments in X-Ray Tomography VII, Proc. SPIE vol. 7804 (2010), 780411.

Hasse et al., "New developments in laboratory-based x-ray sources and optics," Adv. In Laboratory-based X-Ray Sources, Optics, and Applications VI, ed. A.M. Khounsary, Proc. SPIE vol. 10387, 103870B-1 (2017).

Hemraj-Benny et al., "Near-Edge X-ray Absorption Fine Structure Spectroscopy as a Tool for Investigating Nanomaterials," Small, vol. 2(1), (2006), pp. 26-35.

Henke et al., "X-ray interactions: photoabsorption, scattering, transmission, and reflection at E=50-30000 eV, Z=1-92," Atomic Data and Nuclear Data Tables, vol. 54 (No. 2) (Jul. 1993), pp. 181-342.

Hennekam et al., "Trace metal analysis of sediment cores using a novel X-ray fluorescence core scanning method," Quaternary Int'l, https://doi.org/10.1016/j.quaint.2018.10.018 (2018).

Honma et al., Full-automatic XAFS Measurement System of the Engineering Science Research II beamline BL14B2 at Spring-8, 2011, AIP Conference Proceedings 1234, pp. 13-16.

Howard et al., "High-Definition X-ray Fluorescence Elemental Mapping of Paintings," Anal. Chem., 2012, vol. 84(7), pp. 3278-3286.

(56) References Cited

OTHER PUBLICATIONS

Howells, "Gratings and Monochromators in the VUV and Soft X-Ray Spectral Region," Ch. 21 of Handbook of Optics vol. III, 2nd Ed. (McGraw Hill, New York, 2001).

Howells, "Mirrors for Synchrotron-Radiation Beamlines," Publication LBL-34750 (Lawrence Berkeley Laboratory, Berkeley, CA, Sep. 1993).

Hrdy et al, "Diffractive-Refractive Optics: X-ray Crystal Monochromators with Profiled Diffracting Surfaces," Ch. 20 of "Modern Developments in X-Ray and Neutron Optics," A. Erko et al., eds. (Springer, Berlin Heidelberg New York, 2008).

Hwang et al, "New etching process for device fabrication using diamond," Diamond & Related Materials, vol. 13 (2004) pp. 2207-2210.

Ide-Ektessabi et al., "The role of trace metallic elements in neurodegenerative disorders: quantitative analysis using XRF and XANES spectroscopy," Anal. Sci., vol. 21(7) (Jul. 2005), pp. 885-892.

Ihsan et al., "A microfocus X-ray tube based on a microstructured X-ray target", Nuclear Instruments and Methods in Physics Research B vol. 267 (2009) pp. 3566-3573.

Ishisaka et al., "A New Method of Analyzing Edge Effect in Phase Contrast Imaging with Incoherent X-rays," Optical Review, vol. 7, No. 6, (2000), pp. 566-572.

Ito et al., "A Stable In-Laboratory EXAFS Measurement System," Jap. J. Appl. Phys., vol. 22, No. 2, Feb. 1, 1983, pp. 357-360.

Itoh et al., "Two-dimensional grating-based X-ray phase-contrast imaging using Fourier transform phase retrieval," Op. Express, vol. 19, No. 4 (2011) pp. 3339-3346.

Janssens et al, "Recent trends in quantitative aspects of microscopic X-ray fluorescence analysis," TrAC Trends in Analytical Chemistry 29.6 (Jun. 2010): 464-478.

Jahrman et al., "Vacuum formed temporary spherically and toroidally bent crystal analyzers for x-ray absorption and x-ray emission spectroscopy," Rev. Sci. Inst. vol. 90, 013106 (2019).

Jiang et al., "X-Ray Phase-Contrast Imaging with Three 2D Gratings," Int. J. Biomed. Imaging, (2008), 827152, 8 pages.

Jin et al., "Development of an X-ray tube with two selective targets modulated by a magnetic field," Rev. Sci. Inst. vol. 90, 083105 (2019).

Joy, "Astronomical X-ray Optics," Ch. 28 of "Handbook of Optics vol. III, 2nd Ed.," (McGraw Hill, New York, 2001).

Kalasová et al., "Characterization of a laboratory-based X-ray computed nonotomography system for propagation-based method of phase contrast imaging," IEEE Trans. On Instr. And Meas., DOI 10.1109/TIM.2019.2910338 (2019).

Keyrilainen et al., "Phase contrast X-ray imaging of breast," Acta Radiologica, vol. 51 (8), (2010), pp. 866-884. Jan. 18, 2010 pub Jun. 15, 2010.

Kidalov et al., "Thermal Conductivity of Diamond Composites," Materials, vol. 2 (2009) pp. 2467-2495.

Kido et al., "Bone Cartilage Imaging with X-ray Interferometry using a Practical X-ray Tube", in Medical Imaging 2010: Physics of Medical Imaging, Proc. SPIE vol. 7622 (2010), 762240.

Kim, "Talbot images of wavelength-scale amplitude gratings," Opt. Express vol. 20(5), (2012), pp. 4904-4920.

Kim et al., "Observation of the Talbot Effect at Beamline 6C Bio Medical Imaging of he Pohang Light Source-II," J. Korean Phys. Soc., vol. 74, No. 10, pp. 935-940 (May 2019).

Kirkpatrick et al., "Formation of Optical Images by X-Rays", J. Opt. Soc. Am. vol. 38(9) (1948), pp. 766-774.

Kirz, "Phase zone plates for x rays and the extreme uv," J. Op. Soc. Am. vol. 64 (Mar. 1974), pp. 301-309.

Kirz et al., "The History and Future of X-ray Microscopy", J. Physics: Conden. Series vol. 186 (2009): 012001.

Kiyohara et al., "Development of the Talbot-Lau Interferometry System Available for Clinical Use", in International Workshop on X-ray and Neutron Phase Imaging with Gratings, AIP Cong. Proc. vol. 1466, (2012), pp. 97-102.

Klockenkämper et al., "7.1 Instrumental Developments" and "7.3 Future Prospects by Combinations," from Chapter 7 of Total Reflection X-ray Fluorescence Analysis and Related Methods 2nd Ed. (J. Wiley and Sons, Hoboken, NJ, 2015).

Klockenkämper et al., "Chapter 3: Instrumentation for TXRF and GI-XRF," Total Reflection X-ray Fluorescence Analysis and Related Methods 2nd Ed. (J. Wiley and Sons, Hoboken, NJ, 2015).

Kottler et al., "A two-directional approach for grating based differential phase contrast imaging using hard x-rays," Opt. Express vol. 15(3), (2007), pp. 1175-1181.

Kottler et al., "Dual energy phase contrast x-ray imaging with Talbot-Lau interferometer," J. Appl. Phys. vol. 108(11), (2010), 114906. Jul. 7, 2010 pub Dec. 7, 2010.

Kumakhov et al., "Multiple reflection from surface X-ray optics," Physics Reports, vol. 191(5), (1990), pp. 289-350.

Kumakhov, "X-ray Capillary Optics. History of Development and Present Status" in Kumakhov Optics and Application, Proc. SPIE 4155 (2000), pp. 2-12.

Kuwabara et al., "Hard-X-ray Phase-Difference Microscopy with a Low-Brilliance Laboratory X-ray Source", Appl. Phys. Express vol. 4 (2011) 062502.

Kuznetsov, "X-Ray Optics Calculator," Institute of Microelectronics Technology and High Purity Materials, Russian Academy of Sciences (IMT RAS), Chernogolovka, Russia (6 pages submitted); 2016.

Lagomarsino et al., "Reflective Optical Arrays," Ch. 19 of "Modern Developments in X-Ray and Neutron Optics," A. Erko et al. eds. (Springer, Berlin, Germany, 2008), pp. 307-317.

Lai, "X-Ray Microfocusing Optics," Slide Presentation from Argonne National Laboratory, 71 slides, Cheiron Summer School 2007.

Langhoff et al., "X-ray Sources," Ch. 2 of "Handbook of Practical X-Ray Fluorescence Analysis," B. Beckhoff et al., eds. (Springer, Berlin Heidelberg New York, 2006), pp. 33-82.

Lechner et al., "Silicon drift detectors for high count rate X-ray spectroscopy at room temperature," Nuclear Instruments and Methods, vol. 458A (2001), pp. 281-287.

Leenaers et al., "Application of Glancing Incidence X-ray Analysis," 1997, X-ray Spectrometry, vol. 26, pp. 115-121.

Lengeler et al., "Refractive X-ray Optics," Ch. 20 of "Handbook of Optics vol. III, 2nd Ed." (McGraw Hill, New York, 2001.

Li et al., "Source-optic-crystal optimisation for compact monochromatic imaging," Proc. SPIE 5537 (2004), pp. 105-114.

Li et al., "X-ray phase-contrast imaging using cascade Talbot-Lau interferometers," Proc. SPIE 10964 (2018), pp. 1096469-1-1096469-6.

Li et al., "Study on High Thermal Conductivity of X-ray Anode with Composite Diamond Substrate," J. Phys.: Conf. Ser., vol. 1300, 012115 (2019).

Lohmann et al., "An interferometer based on the Talbot effect," Optics Communications vol. 2 (1971), pp. 413-415.

Lübcke et al., "Soft X-ray nanoscale imaging using a sub-pixel resolution charge coupled device (CCD) camera," Ref. Sci. Instrum. vol. 90, 043111 (2019).

Lühl et al., "Scanning transmission X-ray microscopy with efficient X-ray fluorescence detection (STXM-XRF) for biomedical applications in the soft and tender energy range," J. Synch. Rad. vol. 26, https://doi.org/10.1107/S1600577518016879, (2019).

MacDonald et al., "An Introduction to X-ray and Neutron Optics," Ch. 19 of "Handbook of Optics vol. III, 2nd Ed." (McGraw Hill, New York, 2001).

MacDonald et al., "Polycapillary and Multichannel Plate X-Ray Optics," Ch. 30 of "Handbook of Optics vol. III, 2nd Ed.," (McGraw Hill, New York, 2001).

MacDonald et al., "Polycapillary X-ray Optics for Microdiffraction," J. Appl. Cryst., vol. 32 (1999) pp. 160-167.

MacDonald, "Focusing Polycapillary Optics and Their Applications," X-Ray Optics and Instrumentation, vol. 2010, (Oct. 2010): 867049.

Maj et al., "Etching methods for improving surface imperfections of diamonds used for x-ray monochromators," Adv. X-ray Anal., vol. 48 (2005), pp. 176-182.

Malgrange, "X-ray Optics for Synchrotron Radiation," ACTA Physica Polonica A, vol. 82(1) (1992) pp. 13-32.

(56) References Cited

OTHER PUBLICATIONS

Malzer et al., "A laboratory spectrometer for high throughput X-ray emission spectroscopy in catalysis research," Rev. Sci. Inst. 89, 113111 (2018).

Masuda et al., "Fabrication of Through-Hole Diamond Membranes by Plasma Etching Using Anodic Porous Alumina Mask," Electrochemical and Solid-State Letters, vol. 4(11) (2001) pp. G101-G103.

Matsushita, "Mirrors and Multilayers," Slide Presentation from Photon Factor, Tsukuba, Japan, 65 slides, (Cheiron School 2009, Sprint-8, Japan, Nov. 2009).

Matsushita, "X-ray monochromators," Slide Presentation from Photon Factory, Tsukuba, Japan, 70 slides, (Cheiron School 2009, Spring-8, Japan, Nov. 2009).

Matsuyama et al., "Wavefront measurement for a hard-X-ray nanobeam using single-grating interferometry", Opt Express vol. 20 (2012), pp. 24977-24986.

Miao et al., "Motionless phase stepping in X-ray phase contrast imaging with a compact source," Proceedings of the National Academy of Sciences, vol. 110(48), (2013), pp. 19268-19272.

Michette, "Zone and Phase Plates, Bragg-Fresnel Optics," Ch. 23 of "Handbook of Optics vol. III, 2nd Ed.," (McGraw Hill, New York, 2001).

Mizutani et al., X-ray microscopy for neural circuit reconstruction in 9th International Conference on X-Ray Microscopy, J. Phys: Conf. Ser. 186 (2009) 012092.

Modregger et al., "Grating-Based X-ray Phase Contrast Imaging," Ch. 3 of Emerging Imaging Technologies in Medicine, M. Anastasio & P. La Riviere, ed., CRC Press, Boca Raton, FL, (2012), pp. 43-56.

Momose et al., "Biomedical Imaging by Talbot-Type X-Ray Phase Tomography" in Developments in X-Ray Tomography V, Proc. SPIE vol. 6318 (2006) 63180T.

Momose et al., "Grating-Based X-ray Phase Imaging Using Multiline X-ray Source", Jpn. J. Appl. Phys. vol. 48 (2009), 076512.

Momose et al., "Phase Tomography by X-ray Talbot Interferometry for Biological Imaging" Jpn. J. Appl. Phys. vol. 45 2006 pp. 5254-5262.

Momose et al., "Phase Tomography Using X-ray Talbot Interferometer", in Synchrotron Radiation Instrumentation: Ninth International Conference, AIP Conf. Proc. vol. 879 (2007), pp. 1365-1368.

Momose et al., "Phase-Contrast X-Ray Imaging Using an X-Ray Interferometer for Biological Imaging", Analytical Sciences vol. 17 Supplement (2001), pp. i527-i530.

Momose et al., "Sensitivity of X-ray Phase Imaging Based on Talbot Interferometry", Jpn. J. Appl. Phys. vol. 47 (2008), pp. 8077-8080.

Momose et al., "X-ray Phase Measurements with Talbot Interferometry and Its Applications", in International Conference on Advanced Phase Measurement Methods in Optics and Imaging, AIP Conf. Proc. vol. 1236 (2010), pp. 195-199.

Momose et al., "X-ray Phase Imaging—From Static Observation to Dynamic Observation—", in International Workshop on X-ray and Neutron Phase Imaging with Gratings AIP Conf. Proc. vol. 1466, (2012), pp. 67-77.

Momose et al., "X-ray Phase Imaging Using Lau Effect", Appl. Phys. Express vol. 4 (2011) 066603.

Momose et al., "X-Ray Phase Imaging with Talbot Interferometry", in "Biomedical Mathematics: Promising Directions in Imaging, Therapy Planning, and Inverse Problems", Y. Censor, M. Jiang & G.Wang, eds. (Medical Physics Publishing, Madison, WI, USA, 2010), pp. 281-320.

Momose et al., "X-ray phase tomography with a Talbot interferometer in combination with an X-ray imaging microscope", in 9th International Conference on X-Ray Microscopy, J. Phys: Conf. Ser. 186 (2009) 012044.

Momose et al., "X-ray Talbot Interferometry with Capillary Plates", Jpn. J. Appl. Phys. vol. 45 (2006), pp. 314-316.

Momose et al., "Four-dimensional X-ray phase tomography with Talbot interferometry and white synchrotron radiation: dynamic observation of a living worm", Opt. Express vol. 19 (2011), pp. 8423-8432.

Momose et al., "High-speed X-ray phase imaging and X-ray phase tomography with Talbot interferometer and white synchrotron radiation", Opt. Express vol. 17 (2009), pp. 12540-12545.

Momose et al., "Phase Imaging with an X-ray Talbot Interferometer", Advances in X-ray Analysis vol. 49(3) (2006), pp. 21-30.

Momose et al.,"Demonstration of X-Ray Talbot Interferometry", Jpn. J. Appl. Phys. vol. 42 (2003), pp. L866-L868.

Momose et al., Phase Tomography Using an X-ray Talbot Interferometer, in Developments in X-Ray Tomography IV, Proc. SPIE vol. 5535 (2004), pp. 352-360.

Momose, "Recent Advances in X-ray Phase Imaging", Jpn. J. Appl. Phys. vol. 44 (2005), pp. 6355-6367.

Montgomery, "Self Imaging Objects of Infinite Aperture," J. Opt. Soc. Am. vol. 57(6), (1967), pp. 772-778.

Morimoto et al., "Development of multiline embedded X-ray targets for X-ray phase contrast imaging," XTOP 2012 Book of Abstracts, (Ioffe Physical-Technical Institute of the Russian Academy of Sciences, St. Petersburg, Russia, 2012), pp. 74-75.

Morimoto et al., "X-ray phase contrast imaging by compact Talbot-Lau interferometer with a signal transmission grating," 2014, Optics Letters, vol. 39, No. 15, pp. 4297-4300.

Morimoto et al., "Design and demonstration of phase gratings for 2D single grating interferometer," Optics Express vol. 23, No. 23, 29399 (2015).

Munro et al., Design of a novel phase contrast imaging system for mammography, 2010, Physics in Medicine and Biology, vol. 55, No. 14, pp. 4169-4185.

Nango et al., "Talbot-defocus multiscan tomography using the synchrotron X-ray microscope to study the lacuno-canalicular network in mouse bone", Biomed. Opt. Express vol. 4 (2013), pp. 917-923.

Neuhausler et al., "Non-destructive high-resolution X-ray imaging of ULSI micro-electronics using keV X-ray microscopy in Zernike phase contrast," Microelectronic Engineering, Elsevier Publishers BV., Amsterdam, NO, vol. 83, No. 4-9 (Apr. 1, 2006) pp. 1043-1046.

Newville, "Fundamentals of XAFS," (Univ. of Chicago, Chicago, IL, Jul. 23, 2004).

Noda et al., "Fabrication of Diffraction Grating with High Aspect Ratio Using X-ray Lithography Technique for X-ray Phase Imaging," Jpn. J. Appl. Phys. vol. 46, (2007), pp. 849-851.

Noda et al., "Fabrication of High Aspect Ratio X-ray Grating Using X-ray Lithography" J. Solid Mech_Mater. Eng. vol. 3 (2009), pp. 416-423.

Nojeh, "Carbon Nanotube Electron Sources: From Electron Beams to Energy Conversion and Optophononics", ISRN Nanomaterials vol. 2014 (2014): 879827.

Nuhn, "From storage rings to free electron lasers for hard x-rays", J.A37 Phys.: Condens. Matter vol. 16 (2004), pp. S3413-S34121.

Nykanen et al., "X-ray scattering in full-field digital mammography," Med. Phys. vol. 30(7), (2003), pp. 1864-1873.

Office Action received in Chinese Application No. 201580021722.8, dated Jan. 28, 2019.

Office Action received in Japanese Application No. 2016-564245, dated Oct. 23, 2018.

Oji et al., Automatic XAFS measurement system developed at BL14B2 in SPring-8, Available online Nov. 15, 2011, Journal of Synchrotron Radiation, vol. 19, pp. 54-59.

Olbinado et al., "Demonstration of Stroboscopic X-ray Talbot Interferometry Using Polychromatic Synchrotron and Laboratory X-ray Sources", Appl. Phys. Express vol. 6 (2013), 096601.

Ortega et al., "Bio-metals imaging and speciation in cells using proton and synchrotron radiation X-ray microspectroscopy," J. Royal Society Interface vol. 6 suppl. 5 (Oct. 6, 2009), pp. 6S649-58.

Otendal et al., A 9 keV electron-impact liquid-gallium-jet x-ray source, Rev. Sci. Instrum. vol. 79 (2008): 016102.

Oxford Instruments Inc., Series 5000 Model XTF5011 X-ray Tube information, Jun. 1998, 3 pages.

Parrill et al., "GISAXS—Glancing Incidence Small Angle X-ray Scattering," Journal de Physique IV, vol. 3 (Dec. 1993), pp. 411-417.

Paxscan Flat Panel X-ray Imaging, Varian Sales Brochure, (Varian Medical Systems, Palo Alto, CA, Nov. 11, 2004).

(56) References Cited

OTHER PUBLICATIONS

Pfeiffer et al., " Hard-X-ray dark-field imaging using a grating interferometer," Nature Materials vol. 7, (2008), pp. 134-137.

Pfeiffer et al., "Hard x-ray phase tomography with low brilliance x-ray sources," Phys. Rev. Lett. vol. 98, (2007), 108105.

Pfeiffer et al., "Phase retrieval and differential phase-contrast imaging with low-brilliance X-ray sources," Nature Physics vol. 2, (2006), pp. 258-261.

Pfeiffer, "Milestones and basic principles of grating-based x-ray and neutron phase-contrast imaging," in International Workshop on X-ray and Neutron Phase Imaging with Gratings AIP Conf. Proc. vol. 1466, (2012), pp. 2-11.

Pianetta et al., "Application of synchrotron radiation to TXRF analysis of metal contamination on silicon wafer surfaces," Thin Solid Films, vol. 373(1-2), 2000, pp. 222-226.

Potts, "Electron Probe Microanalysis", Ch. 10 of "A Handbook of Silicate Rock Analysis" (Springer Science + Business Media, New York, 1987), pp. 326-382 (equation quoted from p. 336).

Prewitt et al., "FIB Repair of 5X Reticles and Effects on IC Quality," Integrated Circuit Metrology, Inspection, and Process Control VII, Proc. SPIE vol. 1926 (1993), pp. 517-526.

Prewitt et al., "Focused ion beam repair: staining of photomasks and reticles," J. Phys. D Appl. Phys. vol. 26 (1993), pp. 1135-1137.

Prewitt et al., "Gallium Staining in FIB Repair of Photomasks," Microelectronic Engineering, vol. 21 (1993), pp. 191-196.

Pushie et al., "Elemental and Chemically Specific X-ray Fluorescence Imaging of Biological Systems," Chem. Rev. 114:17, 8499-8541 (2014).

Pushie et al., "Prion protein expression level alters regional copper, iron and zinc content in the mouse brain," Metallomics vol. 3, 206-214 (2011).

Qin et al., "Trace metal imaging with high spatial resolution: Applications in biomedicine," Metallomics, vol. 3 (Jan. 2011), pp. 28-37.

Rayleigh, "On copying diffraction gratings and some phenomena connected therewith," Philos. Mag. vol. 11 (1881), pp. 196-205.

Renaud et al., "Probing surface and interface morphology with Grazing Incidence Small Angle X-ray Scattering," Surface Science Reports, vol. 64:8 (2009), pp. 255-380.

Riege, "Electron Emission from Ferroelectrics—A Review", CERN Report CERN AT/93-18 (CERN, Geneva, Switzerland, Jul. 1993).

Rix et al., "Super-Resolution X-ray phase-contrast and dark-field imaging with a single 2D grating and electromagnetic source stepping," Phys. Med. Biol. In press https://doi.org/10.1088/1361-6560/ab2ff5 (2019).

Röntgen, Ueber eine neue Art von Strahlen (Wurzburg Verlag, Wurzburg, Germany, 1896) also, in English, "On a New Kind of Rays," Nature vol. 53 (Jan. 23, 1896). pp. 274-276.

Rovezzi, "Study of the local order around magnetic impurities in semiconductors for spintronics." PhD Dissertation, Condensed Matter, Université Joseph-Fourier—Grenoble I, 2009, English <tel-00442852>.

Rutishauser, "X-ray grating interferometry for imaging and metrology," 2003, Eth Zurich, Diss. ETH No. 20939.

Sato et al., Two-dimensional gratings-based phase-contrast imaging using a conventional x-ray tube, 2011, Optics Letters, vol. 36, No. 18, pp. 3551-3553.

Scherer et al., "Bi-Directional X-Ray Phase-Contrast Mammography," PLoS One, vol. 9, Issue 5 (May 2014) e93502.

Scholz, "X-ray Tubes and Monochromators," Technical Workshop EPIC, Universitat Würzburg (2007); 41 slides, 2007.

Scholze et al., "X-ray Detectors and XRF Detection Channels," Ch. 4 of "Handbook of Practical X-Ray Fluorescence Analysis," B. Beckhoff et al., eds. (Springer, Berlin Heidelberg, Germany, 2006), pp. 85-198.

Scordo et al., "Pyrolitic Graphite Mosaic Drystal Thickness and Mosaicity Optimization for an Extended Source Von Hamos X-ray Spectrometer," Condens. Matter Vo. 4, pp. 38-52 (2019).

Scott, "Hybrid Semiconductor Detectors for High Spatial Resolution Phase-contrast X-ray Imaging," Thesis, University of Waterloo, Department of Electrical and Computer Engineering, 2019.

Sebert, "Flat-panel detectors:how much better are they?" Pediatr. Radiol. vol. 36 (Suppl 2), (2006), pp. 173-181.

Seifert et al., "Talbot-Lau x-ray phase-contrast setup for fast scanning of large samples," Sci. Rep. 9:4199, pp. 1-11 (2019).

Shen, "Polarizing Crystal Optics," Ch. 25 of "Handbook of Optics vol. III, 2nd Ed.," (McGraw Hill, New York, 2001).

Shields et al., "Overview of Polycapillary X-ray Optics," Powder Diffraction, vol. 17(2) (Jun. 2002), pp. 70-80.

Shimura et al., "Hard x-ray phase contrast imaging using a tabletop Talbot-Lau interferometer with multiline embedded x-ray targets", Opt. Lett. vol. 38(2) (2013), pp. 157-159.

Siddons, "Crystal Monochromators and Bent Crystals," Ch. 22 of "Handbook of Optics vol. III, 2nd Ed.," (McGraw Hill, New York, 2001).

Smith, "Fundamentals of Digital Mammography:Physics, Technology and Practical Considerations," Publication R-BI-016 (Hologic, Inc., Bedford, MA, Mar. 2005).

Snigirev et al., "Hard X-Ray Microoptics," Ch. 17 of "Modern Developments in X-Ray and Neutron Optics," A. Erko et al., eds (Springer, Berlin, Germany, 2008), pp. 255-285.

Sparks Jr., "X-ray Fluorescence Microprobe for Chemical Analysis," in Synchrotron Radiation Research, H. Winick & S. Doniach, eds. (Plenum Press, New York, NY 1980), pp. 459-512.

Spiller, "Multilayers," Ch. 24 of "Handbook of Optics vol. III, 2nd Ed.," (McGraw Hill, New York, 2001).

Stampanoni et al., "The First Analysis and Clinical Evaluation of Native Breast Tissue Using Differential Phase-Contrast Mammography," Investigative Radiology, vol. 46, pp. 801-806. pub 2011-12-xx.

Strüder et al., "Silicon Drift Detectors for X-ray Imaging," Presentation at Detector Workshop on Synchrotron Radiation Instrumentation, 54 slides, (Argonne Nat'l Lab, Argonne, IL Dec. 8, 2005), available at: <http://www.aps.anl.gov/News/Conferences/2005/Synchrotron_Radiation_Instrumentation/Presentations/Strueder.pdf>.

Strüder et al., "X-Ray Detectors," Ch. 4 of "X-ray Spectrometry: Recent Technological Advances," K. Tsuji et al. eds. (John Wiley & Sons, Ltd. Chichester, West Sussex, UK, 2004), pp. 63-131.

Stupple et al., "Modeling of Heat Transfer in an Aluminum X-Ray Anode Employing a Chemical Vapor Deposited Diamond Heat Spreader," J. Heat Transfer, Vo. 140, 124501-1-5 (Dec. 2018).

Sun et al., "Combined optic system based on polycapillary X-ray optics and single-bounce monocapillary optics for focusing X-rays from a conventional laboratory X-ray source," Nucl. Inst. and Methods in Phys. Res. A 802 (2015) pp. 5-9.

Sun et al., "Numerical design of in-line X-ray phase-contrast imaging based on ellipsoidal single-bounce monocapillary," Nucl. Inst. And Methods in Phys. Res. A746 (2014) pp. 33-38.

Sunday et al., "X-ray Metrology for the Semiconductor Industry Tutorial," J. Res. Nat'l Inst. Stan. vol. 124: 124003 (2019); https://doi.org/10.6028/jres.124.003.

Suzuki et al., "Hard X-ray Imaging Microscopy using X-ray Guide Tube as Beam Condenser for Field Illumination," J. Phys.: Conf. Ser. vol. 463 (2013): 012028.

Suzuki, "Development of the DIGITEX Safire Cardiac System Equipped with Direct conversion Flat Panel Detector," Digital Angio Technical Report (Shimadzu Corp., Kyoto, Japan, no date, published 2004 with product release).

Takahama, "RADspeed safire Digital General Radiography System Equipped with New Direct—Conversion FPD," Medical Now, No. 62 (2007).

Takeda et al., "Differential Phase X-ray Imaging Microscopy with X-ray Talbot Interferometer" Appl. Phys. Express vol. 1 (2008) 117002.

Takeda et al., "X-Ray Phase Imaging with Single Phase Grating", Jpn. J. Appl. Phys. vol. 46 (2007), pp. L89-L91.

Takeda et al., "In vivo physiological saline-infused hepatic vessel imaging using a two-crystal-interferometer-based phase-contrast X-ray technique", J. Synchrotron Radiation vol. 19 (2012), pp. 252-256.

Talbot, "Facts relating to optical science No. IV," Philos. Mag. vol. 9 (1836), pp. 401-407.

(56) References Cited

OTHER PUBLICATIONS

Tanaka et al., "Cadaveric and in vivo human joint imaging based on differential phase contrast by X-ray Talbot-Lau interferometry", Z. Med. Phys. vol. 23 (2013), pp. 222-227.

Tang et al., "Micro-computed tomography (Micro-CT): a novel approach for intraoperative breast cancer specimen imaging," Breast Cancer Res. Treat. vol. 139, pp. 311-316 (2013).

Taniguchi et al., "Diamond nanoimprint lithography," Nanotechnology, vol. 13 (2002) pp. 592-596.

Terzano et al., Recent advances in analysis of trace elements in environmental samples by X-ray based techniques (IUPAC Technical Report), Pure Appl. Chem. 2019.

Tkachuk et al., "High-resolution x-ray tomography using laboratory sources", in Developments in X-Ray Tomography V, Proc. SPIE 6318 (2006): 631810.

Tkachuk et al., "Multi-length scale x-ray tomography using laboratory and synchrotron sources", Microsc. Microanal. vol. 13 (Suppl. 2) (2007), pp. 1570-1571.

Töpperwien et al., "Multiscale x-ray phase-contrast tomography in a mouse model of transient focal cerebral ischemia," Biomed. Op. Express, vol. 10, No. 1, Jan. 2019, pp. 92-103.

Touzelbaev et al., "Applications of micron-scale passive diamond layers for the integrated circuits and microelectromechanical systems industries," Diamond and Rel. Mat'ls, vol. 7 (1998) pp. 1-14.

Tsuji et al., "X-Ray Spectrometry: Recent Technological Advances," John Wiley & Sons Ltd. Chichester, West Susses, UK 2004), Chapters 1-7.

Udagawa, "An Introduction to In-House EXAFS Facilities," The Rigaku Journal, vol. 6, (1) (1989), pp. 20-27.

Udagawa, "An Introduction to X-ray Absorption Fine Structure," The Rigaku Journal, vol. 11(2)(1994), pp. 30-39.

Uehara et al., "Effectiveness of X-ray grating interferometry for non-destructive inspection of packaged devices", J. Appl. Phys. vol. 114 (2013), 134901.

Viermetz et al., "High resolution laboratory grating-based X-ray phase-contrast CT," Scientific Reports 8:15884 (2018).

Vogt, "X-ray Fluorescence Microscopy: A Tool for Biology, Life Science and Nanomedicine," Presentation on May 16, 2012 at James Madison Univ., Harrisonburg, VA (31 slides), 2012.

Wan et al.,"Fabrication of Multiple Slit Using Stacked-Sliced Method for Hard X-ray Talbot—Lau Interferometer", Jpn. J. Appl. Phys. vol. 47 (2008), pp. 7412-7414.

Wang et al., "Advantages of intermediate X-ray energies in Zernike phase contrast X-ray microscopy," Biotech. Adv., vol. 31 (2013) pp. 387-392.

Wang et al., "Non-invasive classification of microcalcifications with phase-contrast X-ray mammography," Nature Comm. vol. 5:3797, pp. 1-9 (2014).

Wang, On the single-photon-counting (SPC) modes of imaging using an XFEL source, presented at IWORLD2015.

Wang et al., "Precise patterning of diamond films for MEMS application" Journal of Materials Processing Technology vol. 127 (2002), pp. 230-233.

Wang et al., "Measuring the average slope error of a single-bounce ellopsoidal glass monocapillary X-ray condenser based on an X-ray source with an adjustable source size," Nucl. Inst. And Meth. A934, 36-40 (2019).

Wang et al., "High beam-current density of a 10-keV nano-focus X-ray source," Nucl. Inst. And Meth. A940, 475-478 (2019).

Wansleben et al., "Photon flux determination of a liquid-metal jet x-ray source by means of photon scattering," arXiv:1903.06024v1, Mar. 14, 2019.

Weitkamp et al., "Design aspects of X-ray grating interferometry," in International Workshop on X-ray and Neutron Phase Imaging with Gratings AIP Conf. Proc. vol. 1466, (2012), pp. 84-89.

Weitkamp et al., "Hard X-ray phase imaging and tomography with a grating interferometer," Proc. SPIE vol. 5535, (2004), pp. 137-142.

Weitkamp et al., "X-ray wavefront diagnostics with Talbot interferometers," International Workshop on X-Ray Diagnostics and Scientific Application of the European XFEL, Ryn, Poland, (2010), 36 slides.

Weitkamp et al., Tomography with grating interferometers at low-brilliance sources, 2006, SPIE, vol. 6318, pp. 0S-1 to 0S-10.

Weitkamp et al., "X-ray phase imaging with a grating interferometer," Opt. Express vol. 13(16), (2005), pp. 6296-6304.

Weitkamp et al., "X-ray wavefront analysis and optics characterization with a grating interferometer," Appl. Phys. Lett. vol. 86, (2005), 054101.

Wen et al., "Fourier X-ray Scattering Radiography Yields Bone Structural Information," Radiology, vol. 251 (2009) pp. 910-918.

Wen et al., "Single-shot x-ray differential phase-contrast and diffraction imaging using two-dimensional transmission gratings," Op. Lett. vol. 35, No. 12, (2010) pp. 1932-1934.

Wittry et al., "Properties of fixed-position Bragg diffractors for parallel detection of x-ray spectra," Rev. Sci. Instr. vol. 64, pp. 2195-2200 (1993).

Wobrauschek et al., "Energy Dispersive, X-Ray Fluorescence Analysis," Encyclopedia of Analytical Chemistry, R.A. Meyers, Ed. (Wiley 2010).

Wobrauschek et al., "Micro XRF of light elements using a polycapillary lens and an ultra-thin window Silicon Drift Detector inside a vacuum chamber," 2005, International Centre for Diffraction Data 2005, Advances in X-ray Analysis, vol. 48, pp. 229-235.

Wolter, "Spiegelsysteme streifenden Einfalls als abbildende Optiken fur Rontgenstrahlen" [Grazing Incidence Reflector Systems as Imaging Optics for X-rays] Annalen der Physik vol. 445, Issue 1-2 (1952), pp. 94-114.

X-ray-Optics.de Website, http://www.x-ray-optics.de/, accessed Feb. 13, 2016.

Yakimchuk et al., "Ellipsoidal Concentrators for Laboratory X-ray Sources: Analytical approaches for optimization," Mar. 22, 2013, Crystallography Reports, vol. 58, No. 2, pp. 355-364.

Yamamoto, "Fundamental physics of vacuum electron sources", Reports on Progress in Physics vol. 69, (2006), pp. 181-232.

Yanagihara et al., "X-Ray Optics," Ch. 3 of "X-ray Spectrometry: Recent Technological Advances," K. Tsuji et al. eds. (John Wiley & Sons, Ltd. Chichester, West Sussex, UK, 2004), pp. 63-131.

Yang et al., "Analysis of Intrinsic Stress in Diamond Films by X-ray Diffraction," Advances in X-ray Analysis, vol. 43 (2000), pp. 151-156.

Yashiro et al., "Distribution of unresolvable anisotropic microstructures revealed in visibility-contrast images using x-ray Talbot interferometry", Phys. Rev. B vol. 84 (2011), 094106.

Yashiro et al., "Hard x-ray phase-imaging microscopy using the self-imaging phenomenon of a transmission grating", Phys. Rev. A vol. 82 (2010), 043822.

Yashiro et al., "Theoretical Aspect of X-ray Phase Microscopy with Transmission Gratings" in International Workshop on X-ray and Neutron Phase Imaging with Gratings, AIP Conf. Proc. vol. 1466, (2012), pp. 144-149.

Yashiro et al., "X-ray Phase Imaging and Tomography Using a Fresnel Zone Plate and a Transmission Grating", in "The 10th International Conference on X-ray Microscopy Radiation Instrumentation", AIP Conf. Proc. vol. 1365 (2011) pp. 317-320.

Yashiro et al., "Efficiency of capturing a phase image using cone-beam x-ray Talbot interferometry", J. Opt. Soc. Am. A vol. 25 (2008), pp. 2025-2039.

Yashiro et al., "On the origin of visibility contrast in x-ray Talbot interferometry", Opt. Express (2010), pp. 16890-16901.

Yashiro et al., "Optimal Design of Transmission Grating for X-ray Talbot Interferometer", Advances in X-ray Analysis vol. 49(3) (2006), pp. 375-379.

Yashiro et al., "X-ray Phase Imaging Microscopy using a Fresnel Zone Plate and a Transmission Grating", in the 10th International Conference on Synchrotron Radiation Instrumentation, AIP Conf. Proc. vol. 1234 (2010), pp. 473-476.

Yashiro et. al., "Hard-X-Ray Phase-Difference Microscopy Using a Fresnel Zone Plate and a Transmission Grating", Phys. Rev. Lett. vol. 103 (2009), 180801.

(56) **References Cited**

OTHER PUBLICATIONS

Yu et al., “Morphology and Microstructure of Tungsten Films by Magnetron Sputtering,” Mat. Sci. Forum, vol. 913, pp. 416-423 (2018).
Zanette et al., “Two-Dimensional X-Ray Grating interferometer,” Phys. Rev. Lett. vol. 105 (2010) pp. 248102-1 248102-4.
Zeeshan et al., “In-house setup for laboratory-based x-ray absorption fine structure spectroscopy measurements,” Rev. Sci. Inst. 90, 073105 (2019).
Zeng et al., “Ellipsoidal and parabolic glass capillaries as condensers for x-ray microscopes,” Appl. Opt. vol. 47 (May 2008), pp. 2376-2381.
Zeng et al., “Glass Monocapillary X-ray Optics and Their Applications in X-Ray Microscopy,” X-ray Optics and Microanalysis: Proceedings of the 20th International Congress, AIP Conf. Proc. vol. 1221, (2010), pp. 41-47.
Zhang et al., “Application of confocal X-ray fluorescence based on capillary X-ray optics in nondestructively measuring the inner diameter of monocapillary optics,” Optics Comm. (2018) https://doi.org/10.1016/j.optcom.2018.11.064.
Zhang et al., “Fabrication of Diamond Microstructures by Using Dry and Wet Etching Methods”, Plasma Science and Technology vol. 15(6) (Jun. 2013), pp. 552-554.
Zhang et al., “Measurement of the inner diameter of monocapillary with confocal X-ray scattering technology based on capillary X-ray optics,” Appl. Opt. (Jan. 8, 2019), doc ID 351489, pp. 1-10.
Behling, “Medical X-ray sources Now and for the Future,” Nucl. Inst. and Methods in Physics Research A 873, pp. 43-50 (2017).
Chang et al., “Ultra-high aspect ratio high-resolution nanofabrication of hard X-ray diffractive optics,” Nature Comm. 5:4243, doi: 10.1038/ncomms5243 (2014).
Dittler et al., “A mail-in and user facility for X-ray absorption near-edge structure: the CEI-XANES laboratory X-ray spectrometer at University of Washington,” J. Synch. Rad. vol. 26, eight pages, (2019).
Huang et al., “Theoretical analysis and optimization of highly efficient multilayer-coated blazed gratings with high fix-focus constant for the tender X-ray region,” Op. Express Vo. 28, No. 2, pp. 821-845 (2020).
Kim et al., “A Simulation Study on the Transfer Characteristics of the Talbot Pattern Through Scintillation Screens in the Grating Interferometer,” J. Rad. Sci. and Tech. 42(1), pp. 67-75 (2019).
Kulow et al., “On the Way to Full-Field X-ray Fluorescence Spectroscopy Imaging with Coded Apertures,” J. Anal. At. Spectrom. Doi: 10.1039/C9JA00232D (2019).
Li et al., “Production and Heat Properties of an X-ray Reflective Anode Based on a Diamond Heat Buffer Layer,” Materials vol. 13, p. 241 (2020).
Zhou et al., “Quasi-parallel X-ray microbeam obtained using a parabolic monocapillary X-ray lens with an embedded square-shaped lead occluder,” arXiv:2001.04667 (2020).
Akan et al., “Metal-Assisted Chemical Etching and Electroless Deposition for Fabrication of Hard X-ray Pd/Si Zone Plates,” Micromachines, vol. 11, 301; doi:10.3390/mil 1030301 (2020).
Hashimoto et al., “Improved reconstruction method for phase stepping data with stepping errors and dose fluctuations,” Optics Express, vol. 28, No. 11, pp. 16363-16384 (2020).
Momose et al., “Recent Progress in X-ray and Neutron Phase Imaging with Gratings,” Quantum Beam Science, vol. 4, No. 9; doi:10.3390/qubs4010009 (2020).
Takeo et al., “Soft x-ray nanobeam formed by an ellipsoidal mirror,” Appl. Phys. Lett., vol. 116, 121102 (2020).
Wang et al., “Double-spherically bent crystal high-resolution X-ray spectroscopy of spatially extended sources,” Chinese Optics Lett., vol. 18(6), 061101 (2020).
Yamada et al., “Compact full-field hard x-ray microscope based on advanced Kirkpatrick-Baez mirrors,” Optica, vol. 7, No. 4 pp. 367-370 (2020).
Yoshioka et al., “Imaging evaluation of the cartilage in rheumatoid arthritis patients with an x-ray phase imaging apparatus based on Talbot-Lau interferometry,” Scientific Reports, 10:6561, https://doi.org/10.1038/s41598-020-63155-9 (2020).
Morimoto et a., “X-ray phase contrast imaging by compact Talbot-Lau interferometer with a signal transmission grating”, Jul. 16, 2014, Optics Letters, vol. 39, No. 15. pp. 4297-4300.
Shimura et al., Hard x-ray phase contrast imaging using a tabletop Talbot-Lau interferometer with multiple embedded x-ray targets, Jan. 9, 2013, Optics Letters, vol. 38, No. 2, pp. 157-159.

* cited by examiner

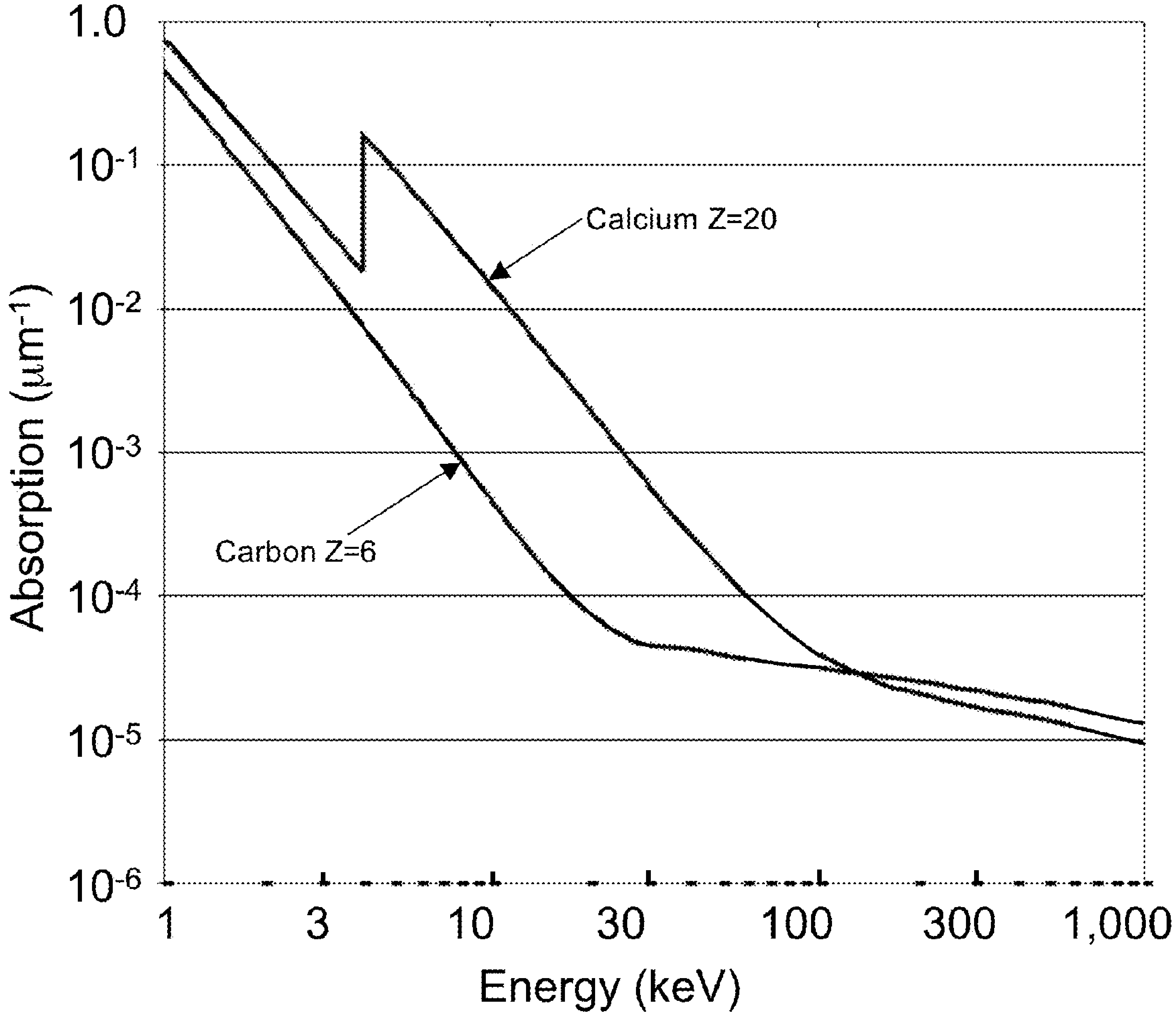
1.0
10^{-1}
10^{-2}
10^{-3}
10^{-4}
10^{-5}
10^{-6}
Absorption (μm^{-1})
Calcium Z=20
Carbon Z=6
1
3
10
30
100
300
1,000
Energy (keV)

FIG. 1

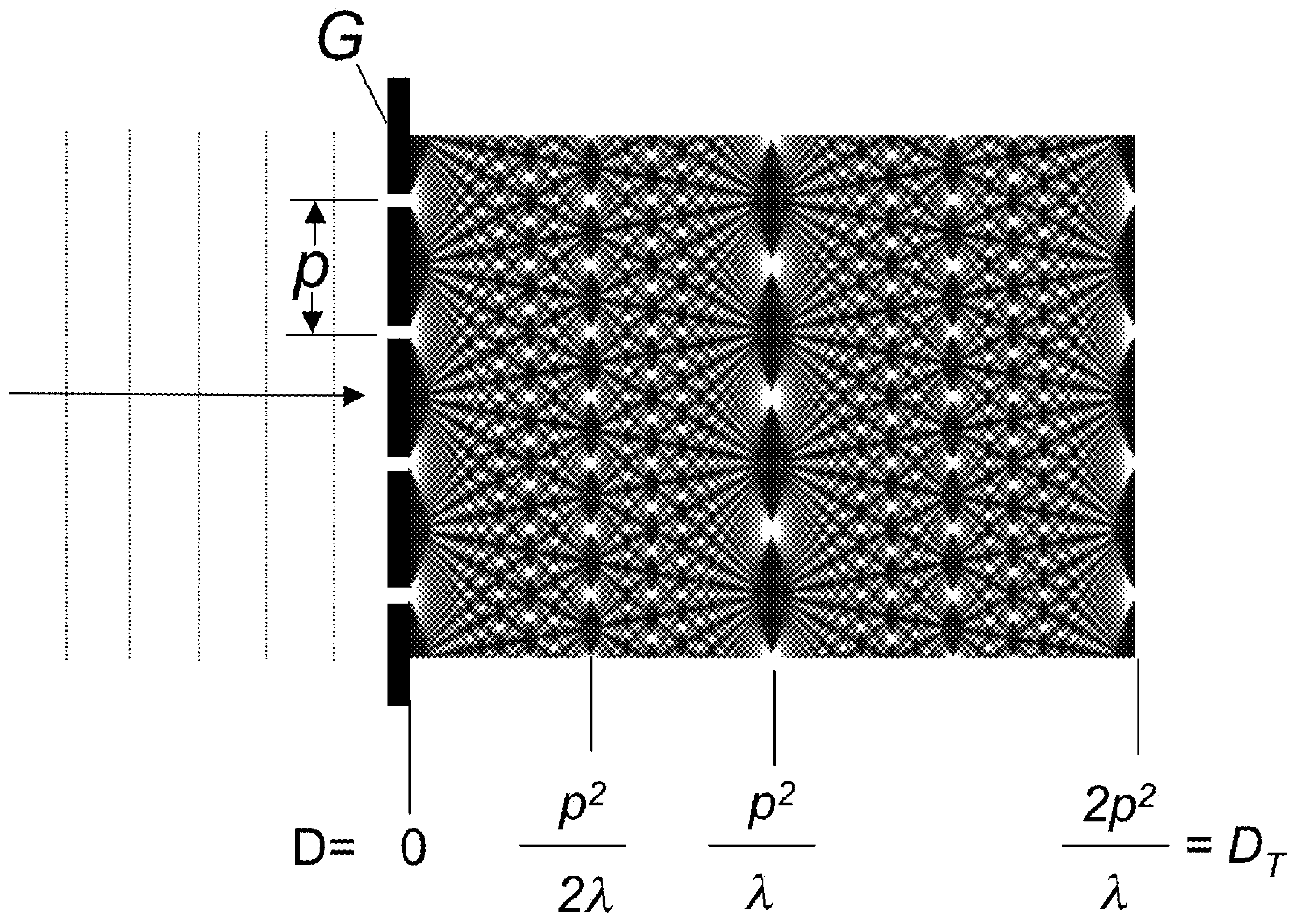

FIG. 2

Prior Art

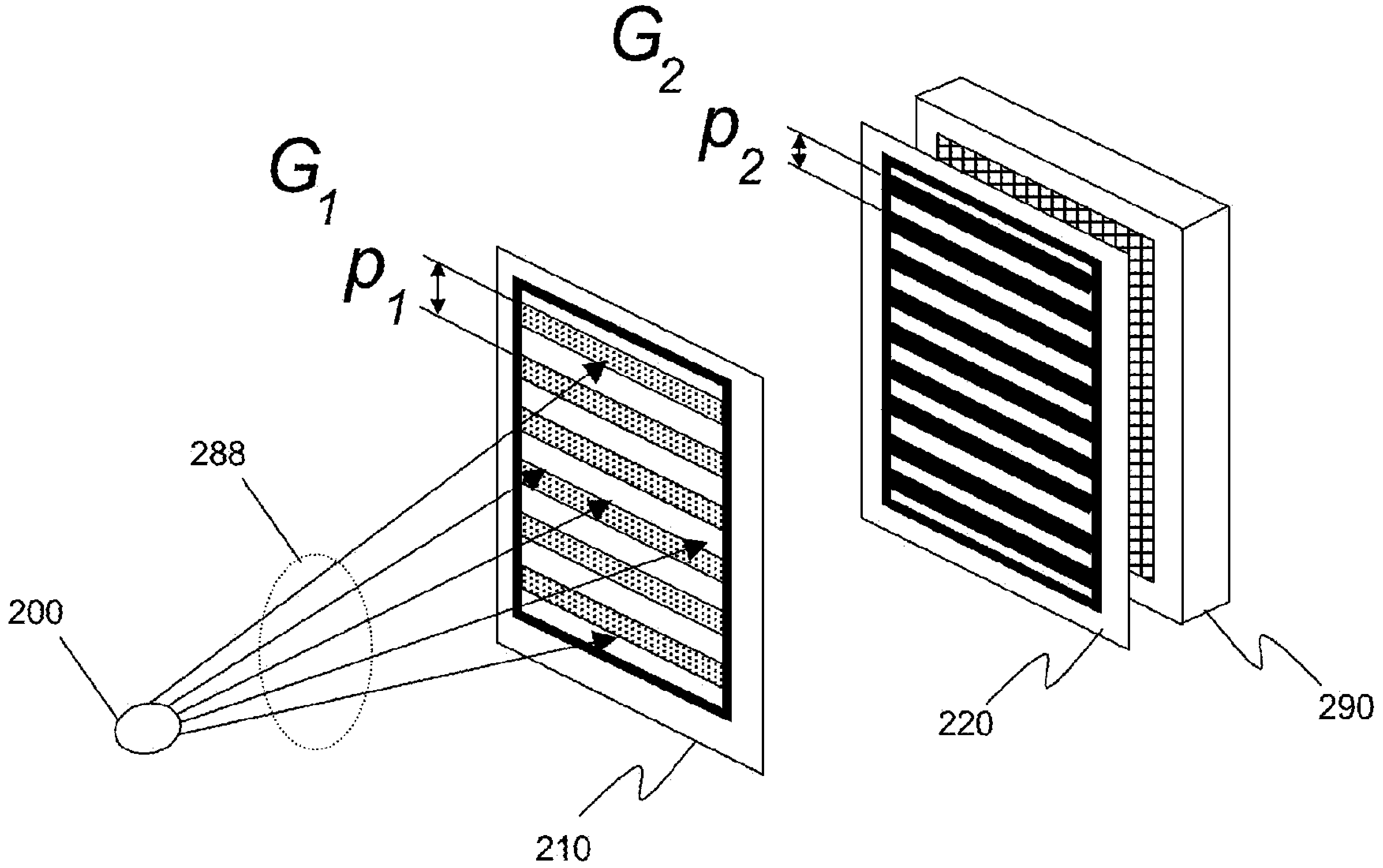

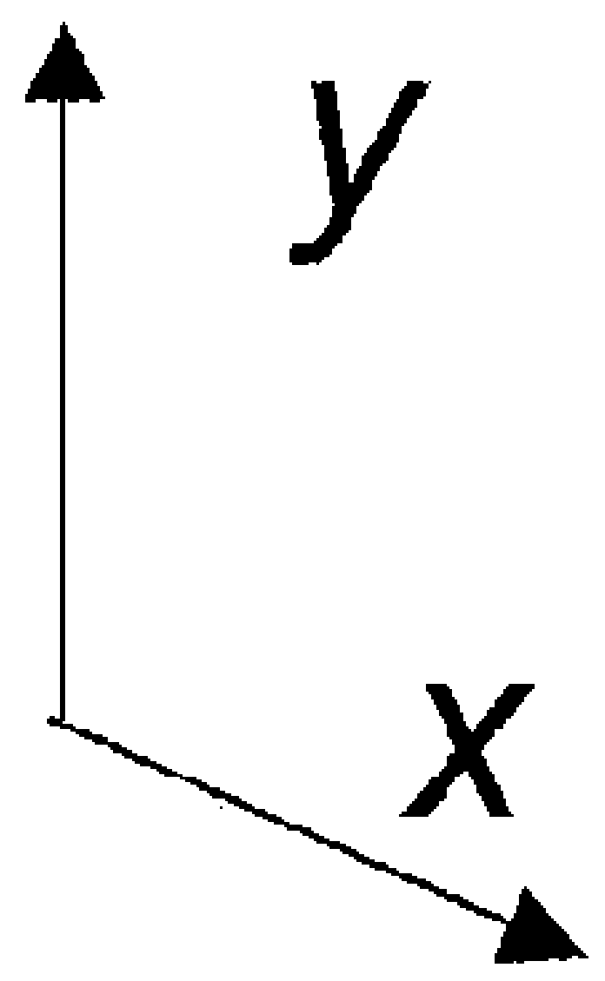

FIG. 3

Prior Art

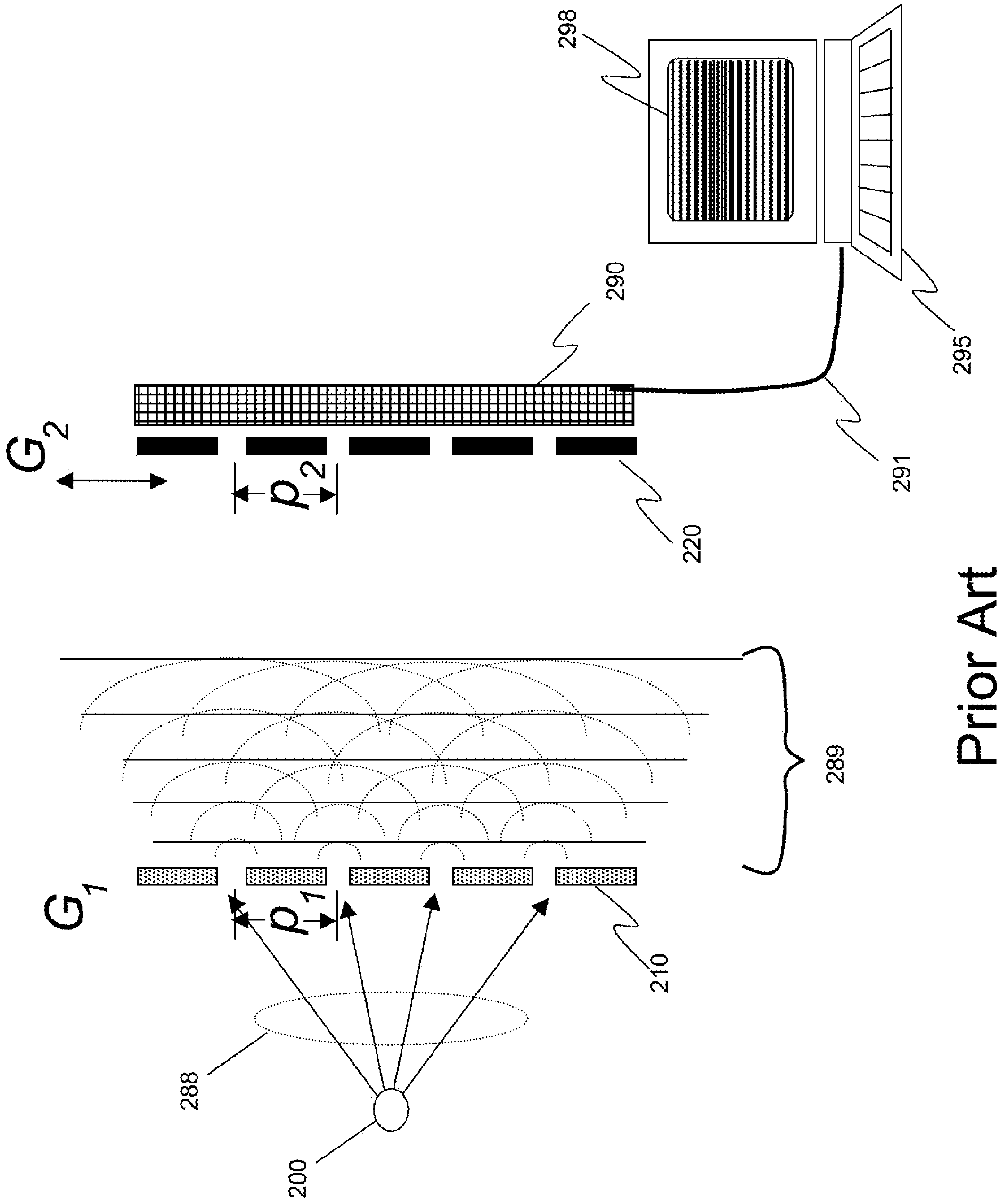

Prior Art

FIG. 4

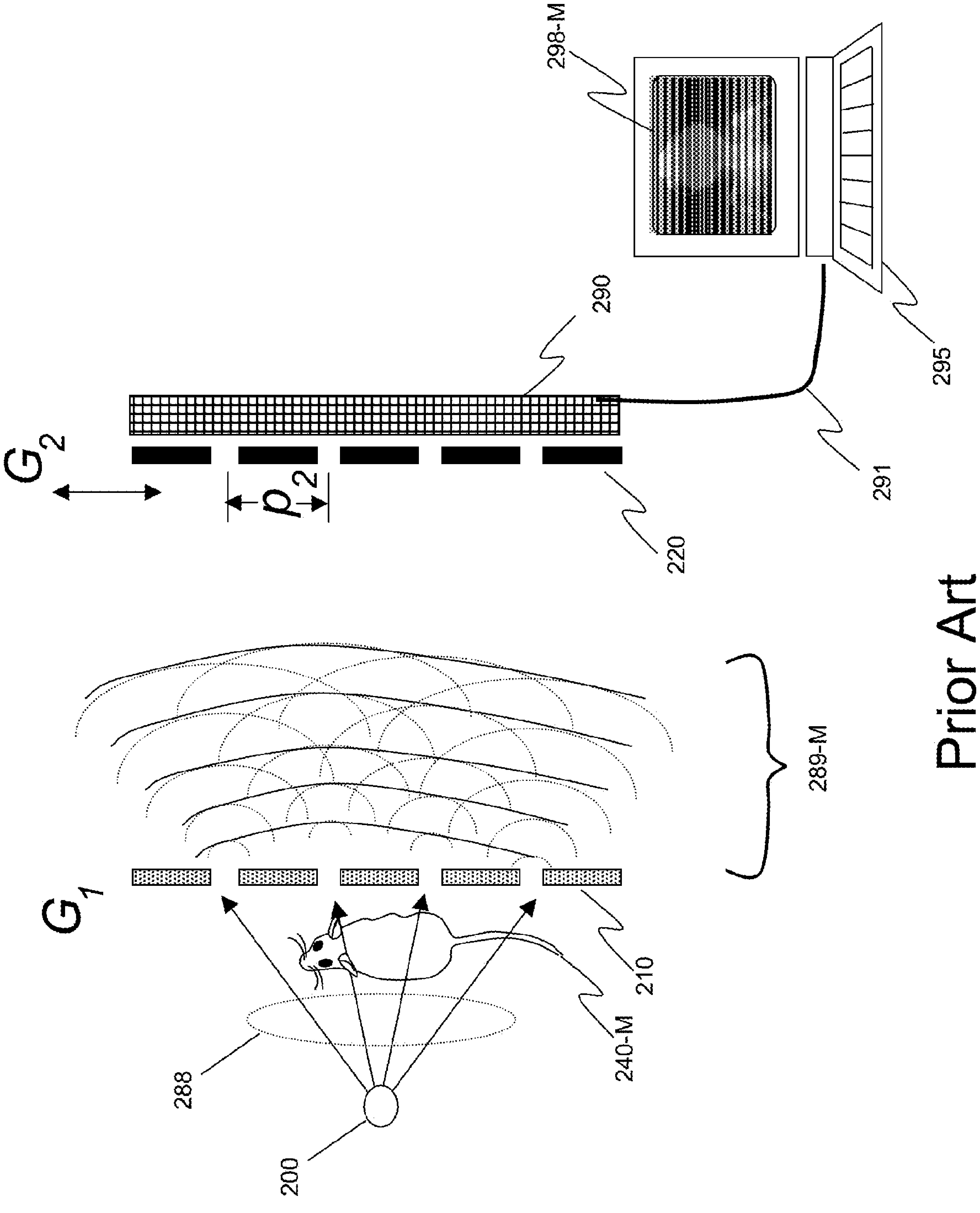

FIG. 5

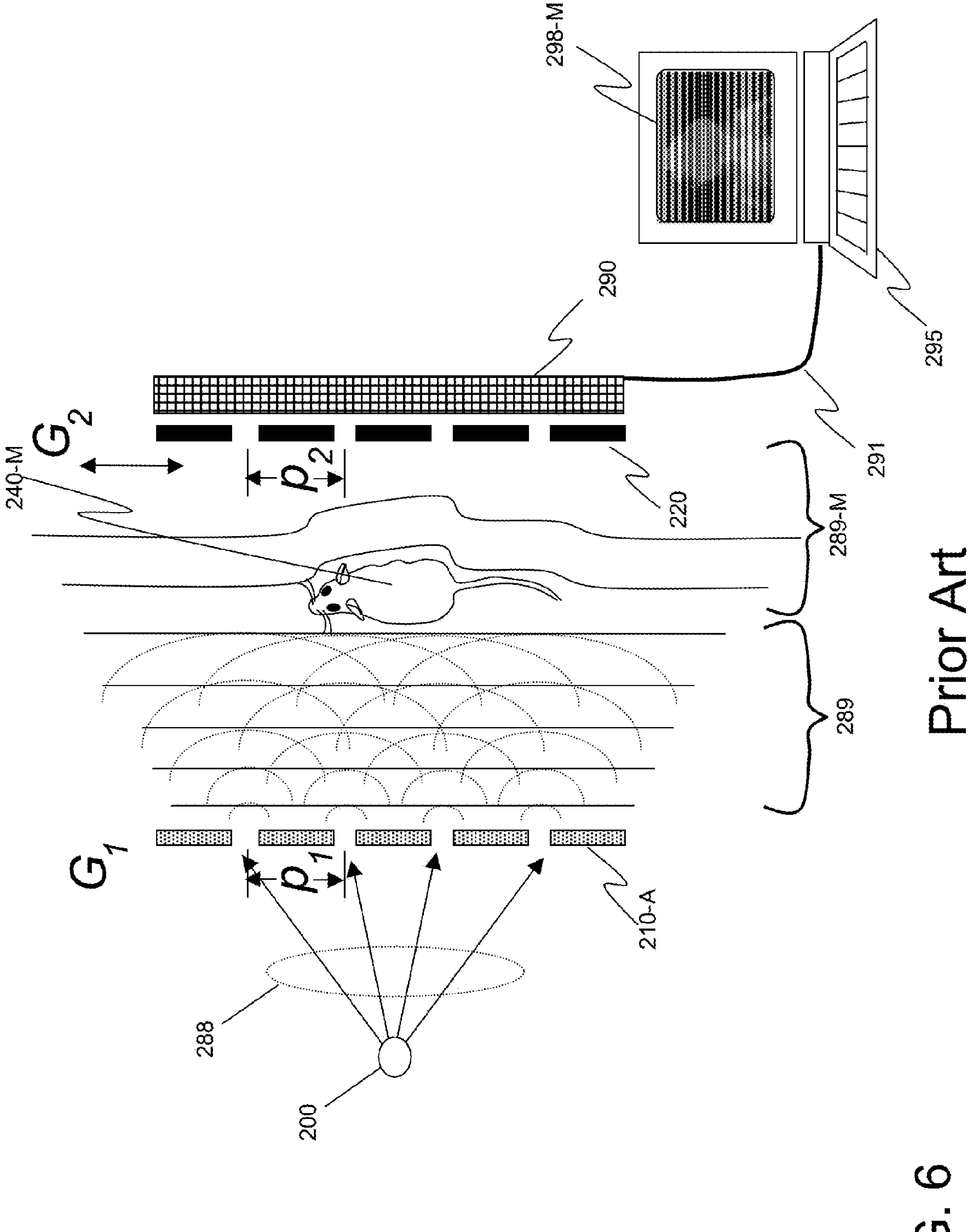

Prior Art

FIG. 6

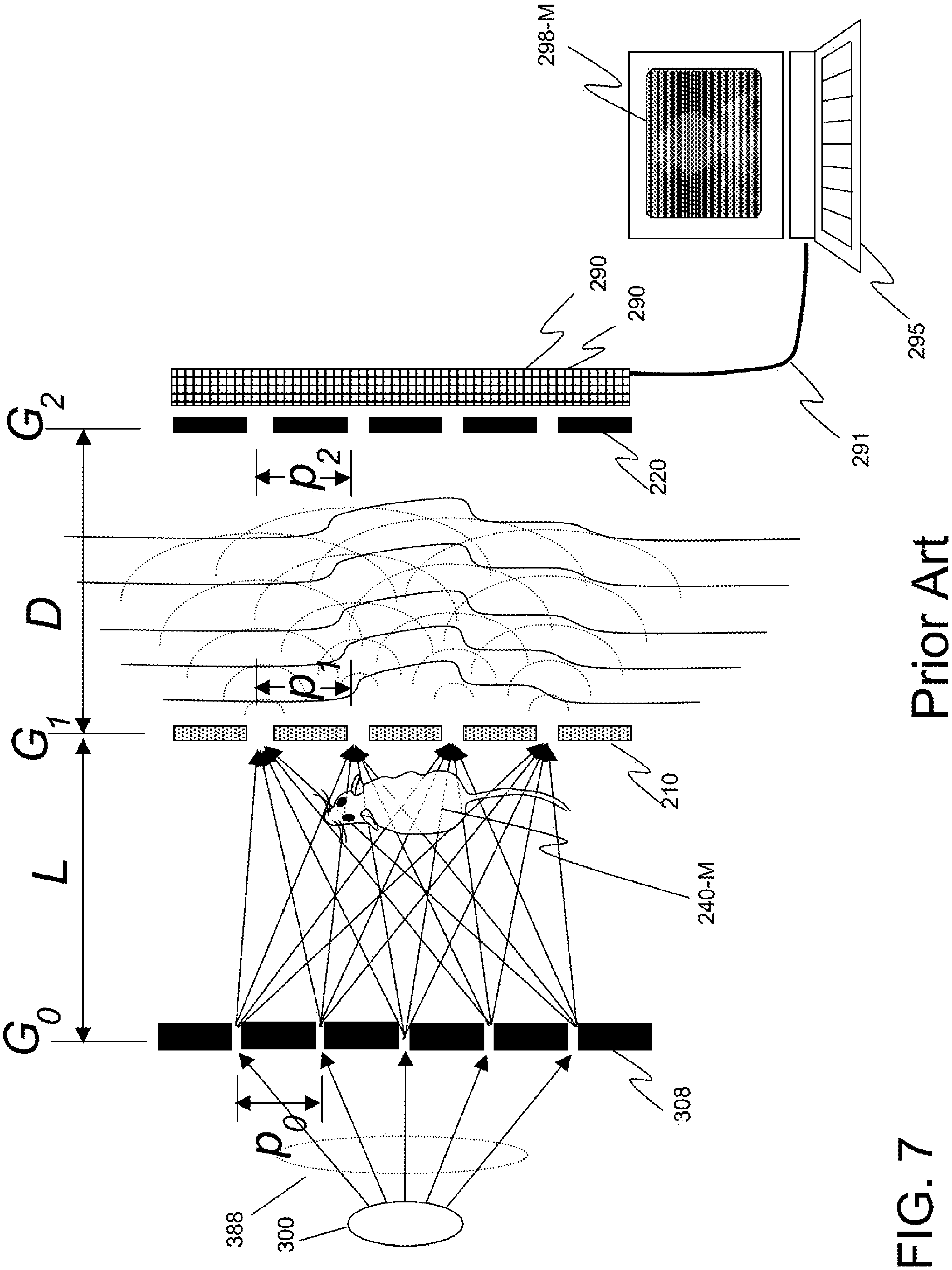

Prior Art

FIG. 7

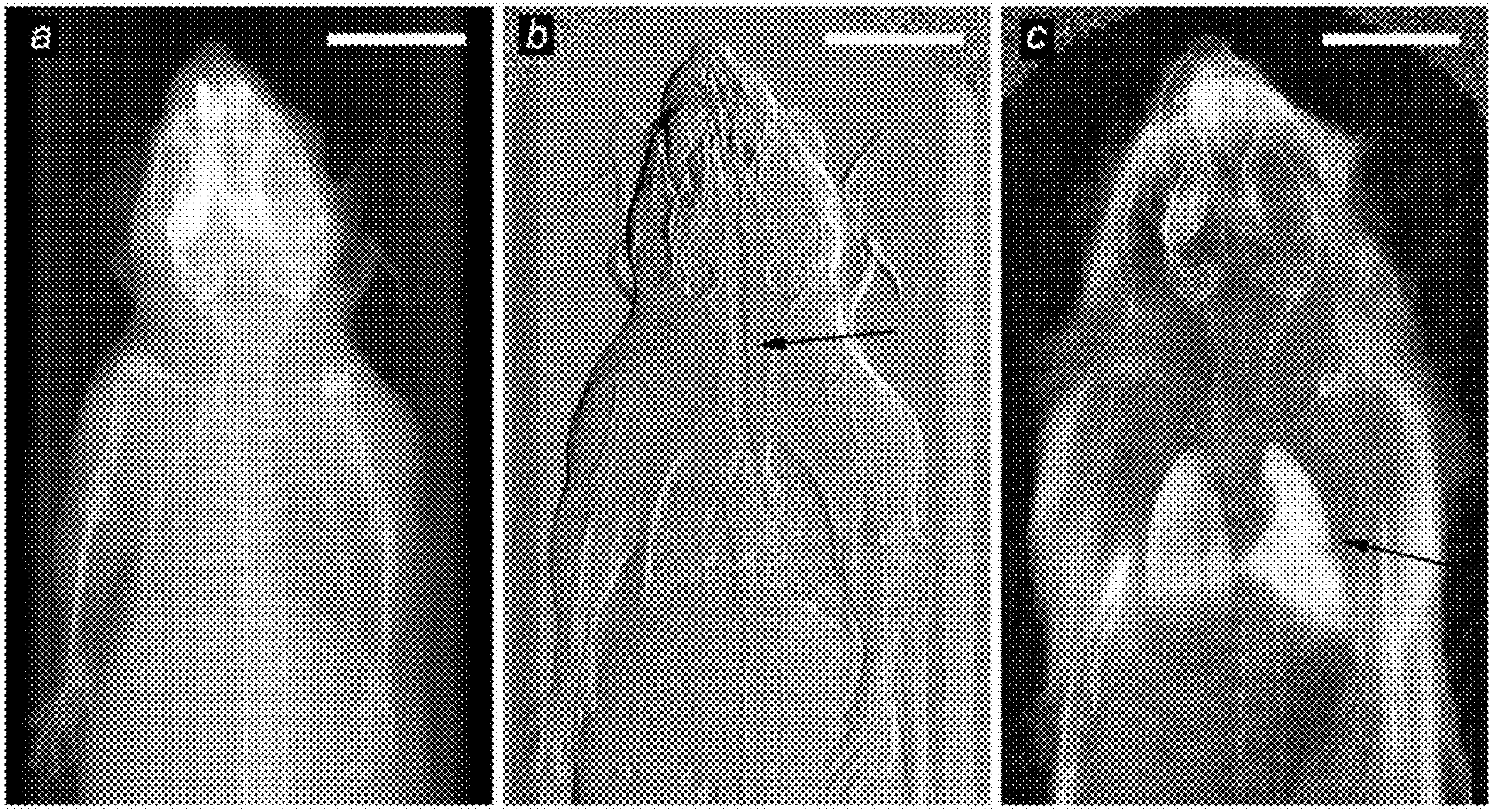

FIG. 8A FIG. 8B FIG. 8C

Prior Art

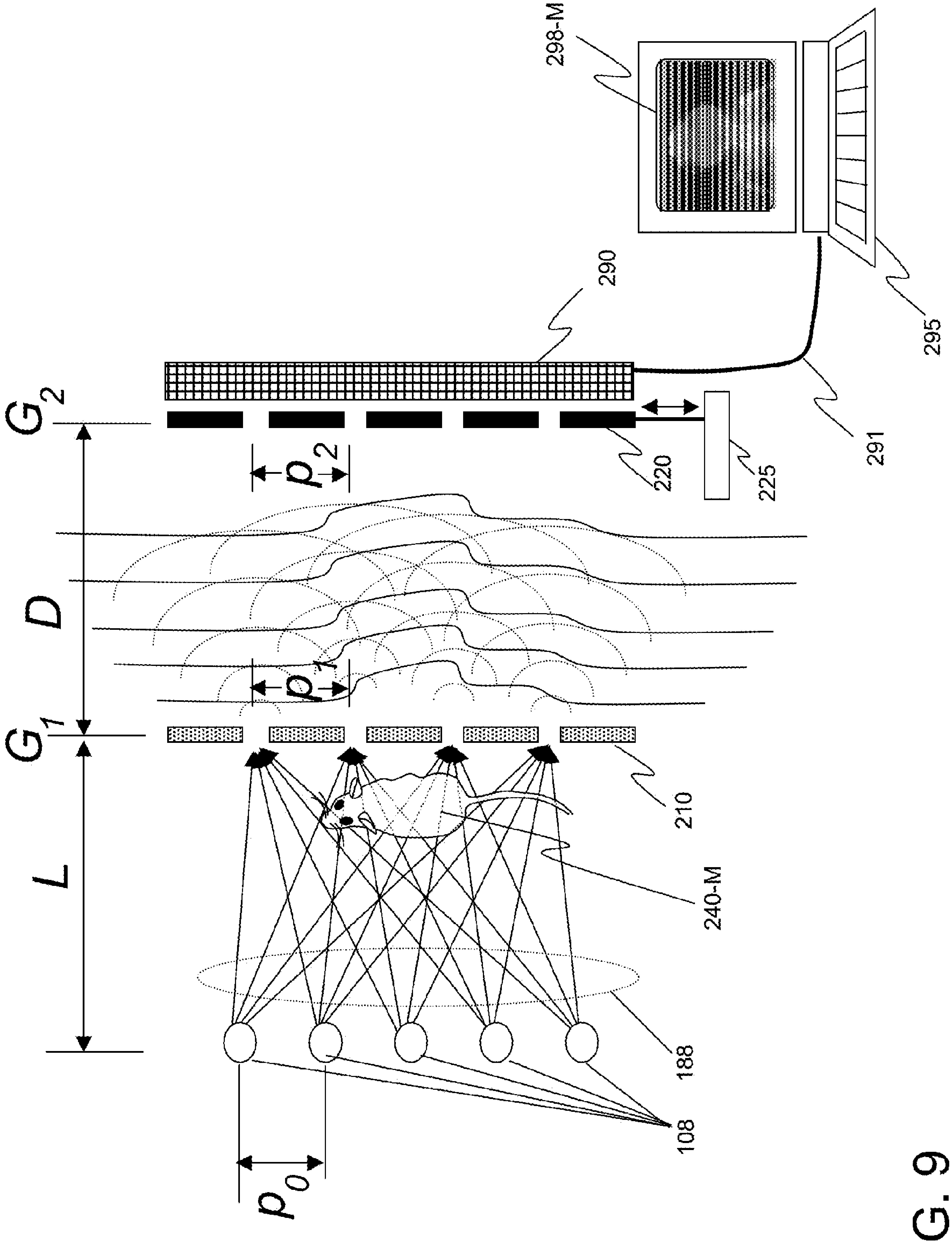

FIG. 9

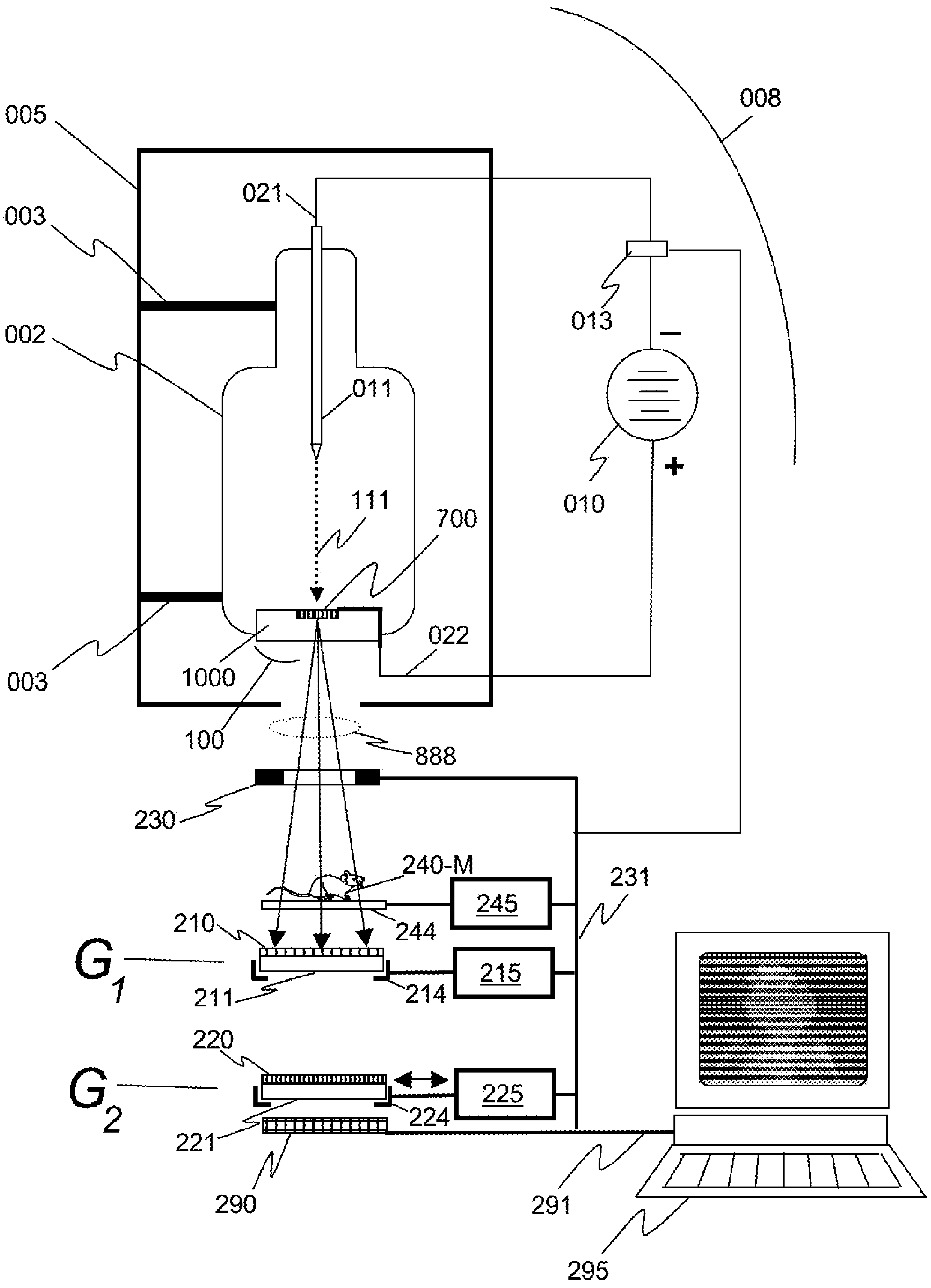
005
003
002
003
021
011
111
700
1000
100
022
888
008
013
010
–
+
230
240-M
245
244
231
210
G1
215
211
214
220
G2
225
224
221
290
291
295

FIG. 10

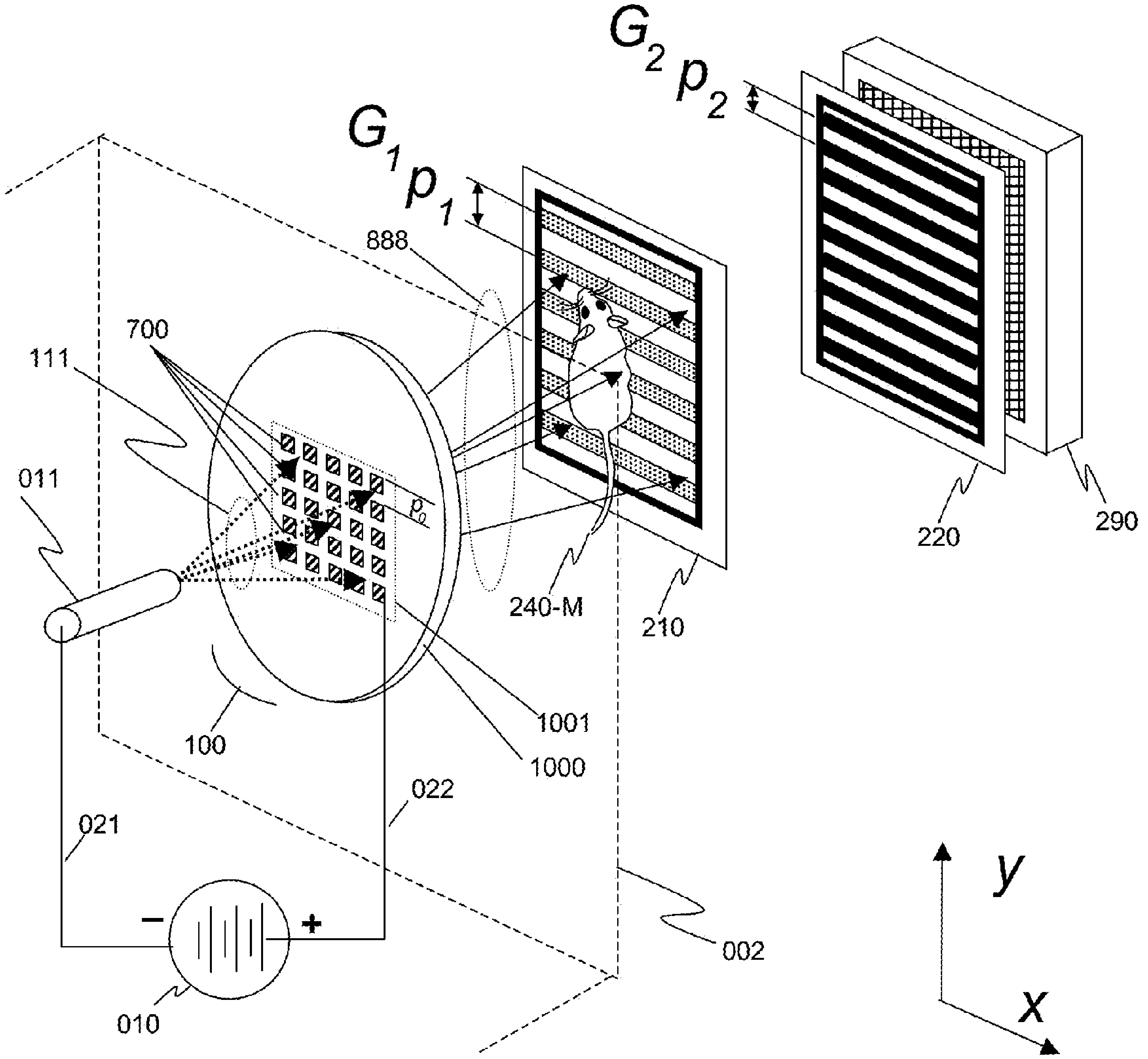
G_2 p_2
G_1 p_1
888
700
111
011
p_0
240-M
210
220
290
100
1001
1000
022
021
−
+
010
002
y
x

FIG. 11

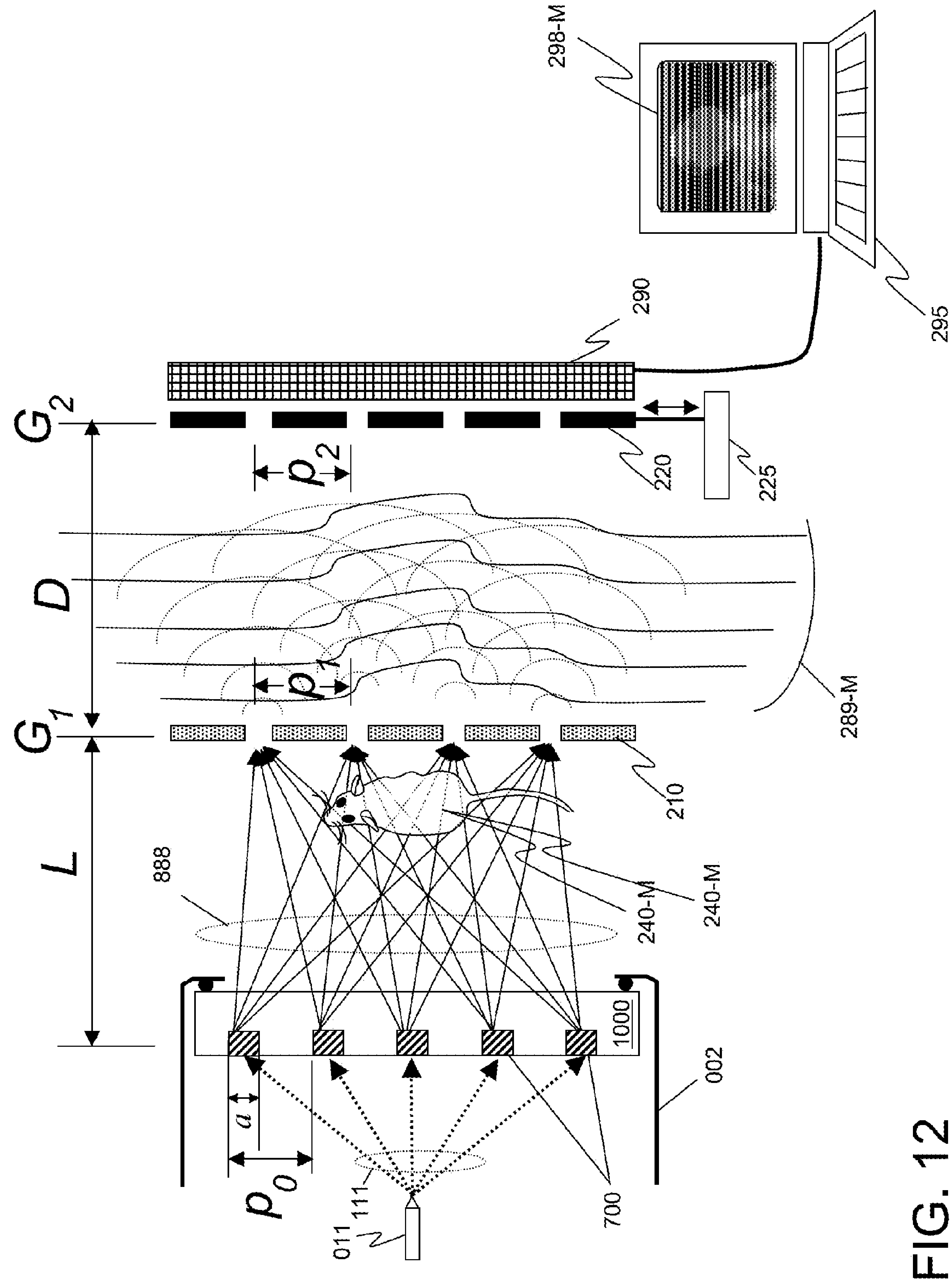
298-M
290
295
G_2
p_2
220
225
D
p_1
289-M
G_1
210
L
888
240-M
240-M
1000
002
a
p_0
111
011
700

FIG. 12

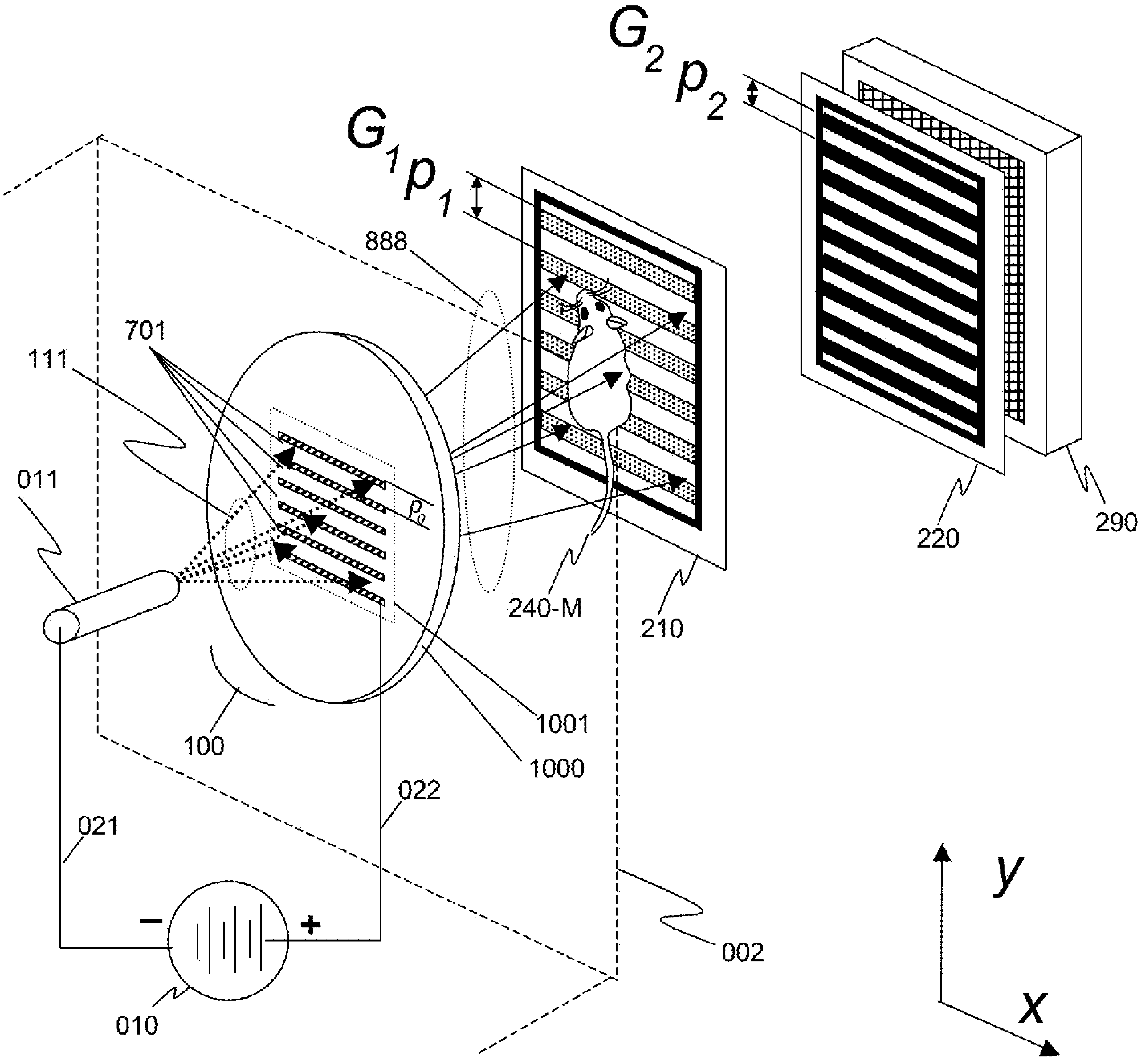
G_2
p_2
G_1
p_1
888
701
111
011
p_0
240-M
210
220
290
100
1001
1000
022
021
−
+
002
010
y
x

FIG. 13

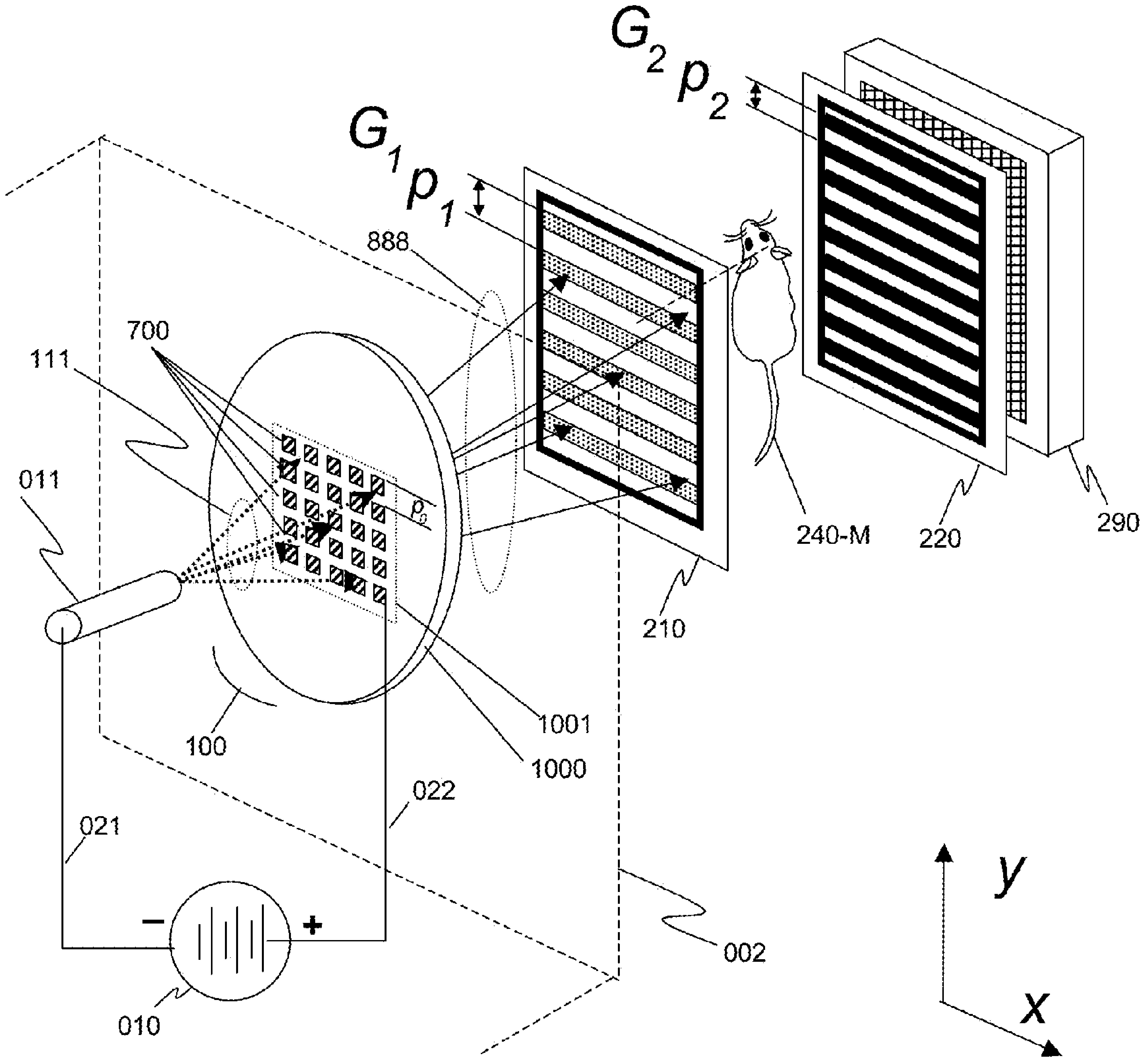
G_2
p_2
G_1
p_1
888
700
111
011
p_0
240-M
220
290
210
1001
100
1000
022
021
−
+
002
010
y
x

FIG. 14

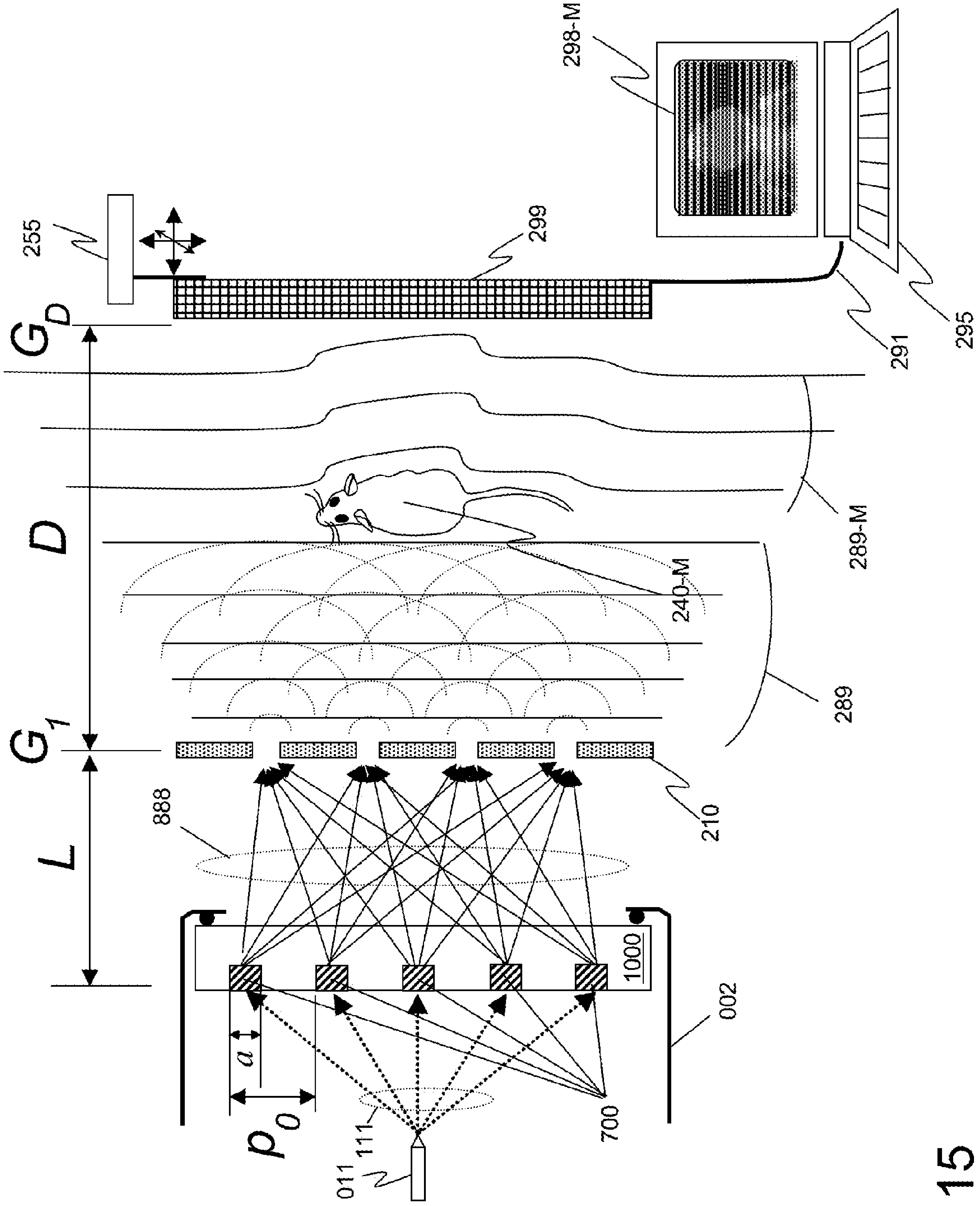
298-M
255
299
G_D
291
295
D
289-M
240-M
289
G_1
210
888
L
1000
002
700
a
p_0
111
011

FIG. 15

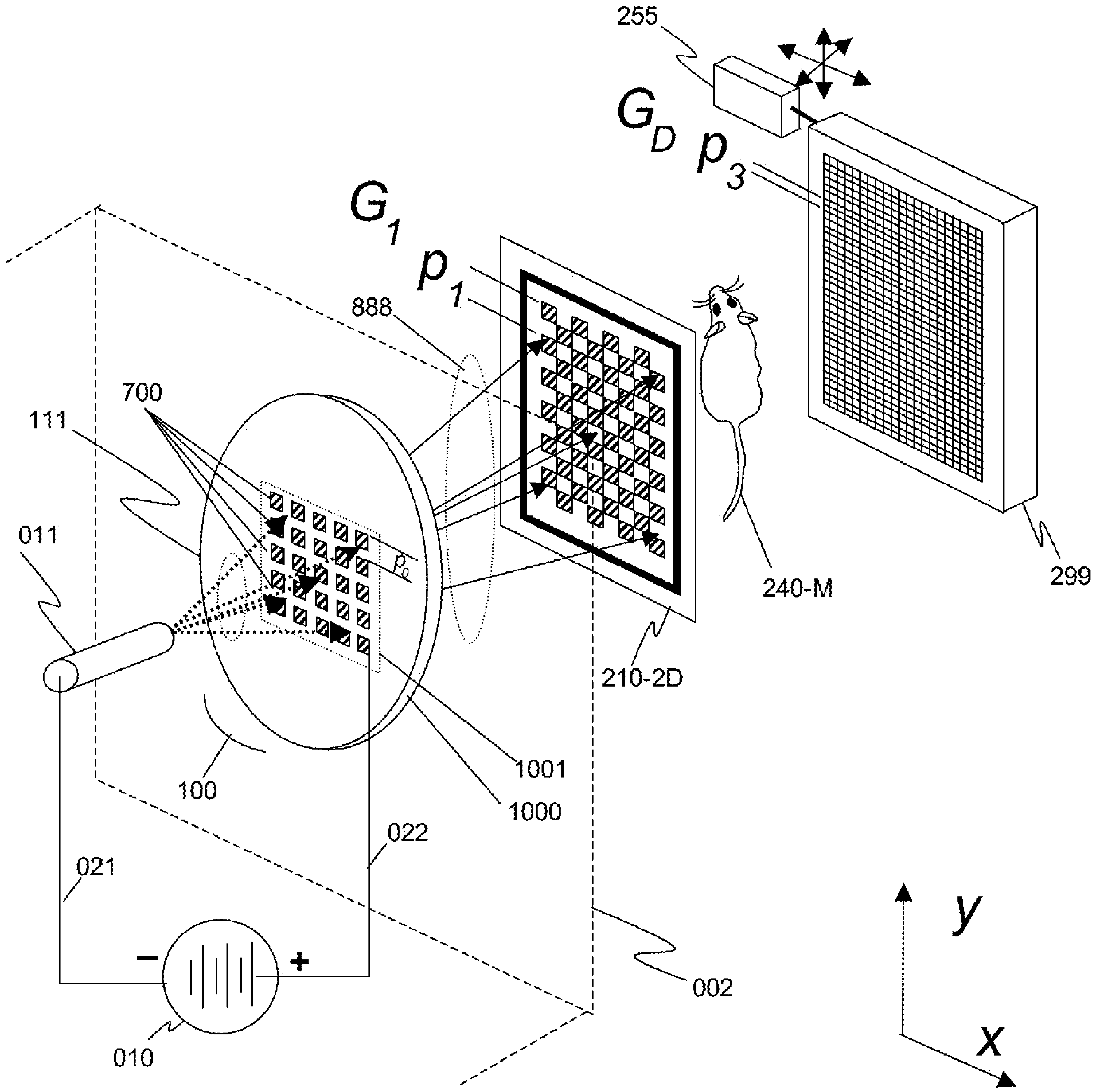
255
G_D
p_3
G_1
p_1
888
700
111
011
p_0
240-M
299
210-2D
1001
100
1000
022
021
−
+
002
010
y
x

FIG. 16

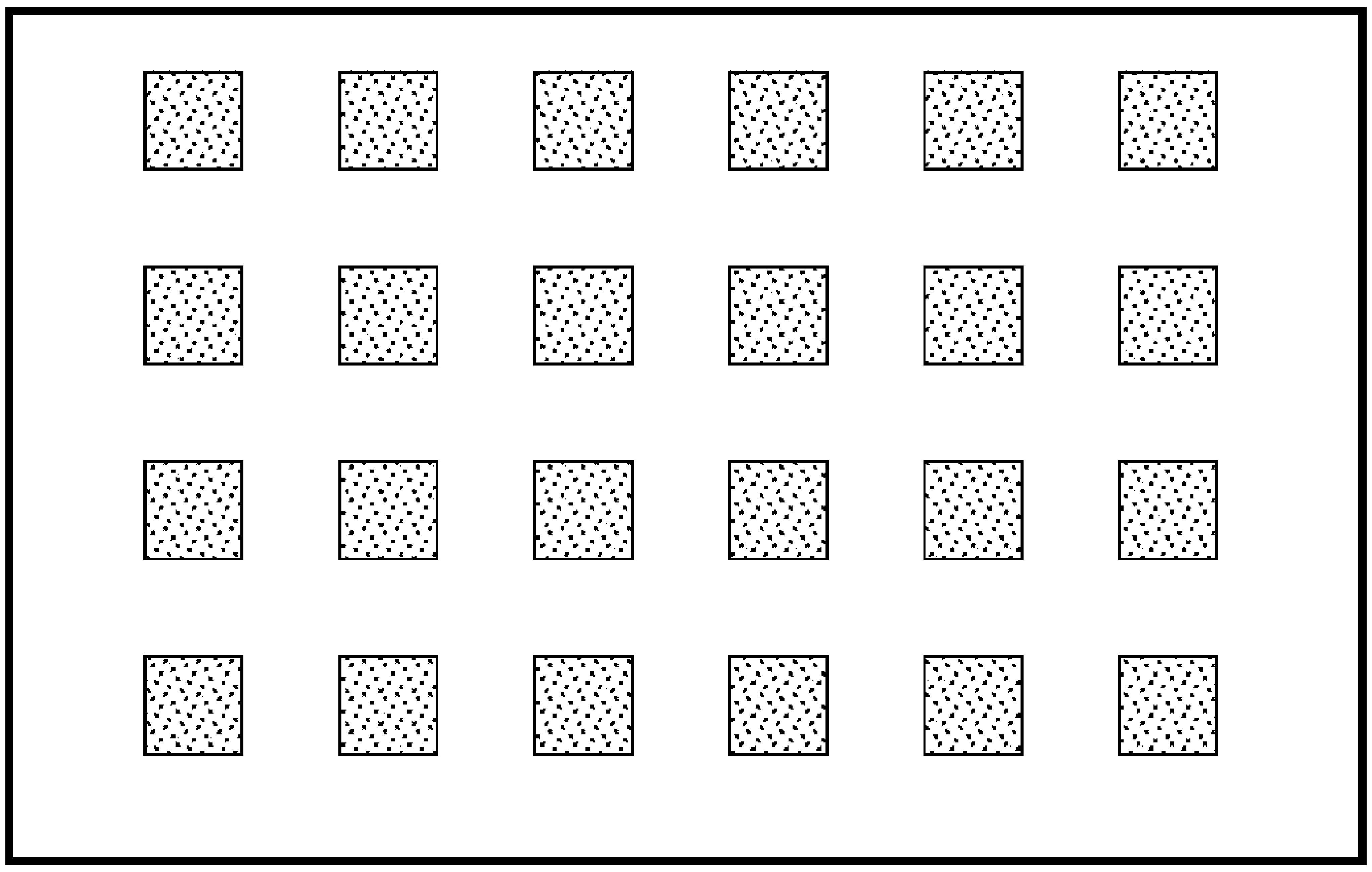

▨ Phase shift

☐ No Phase shift

FIG. 17

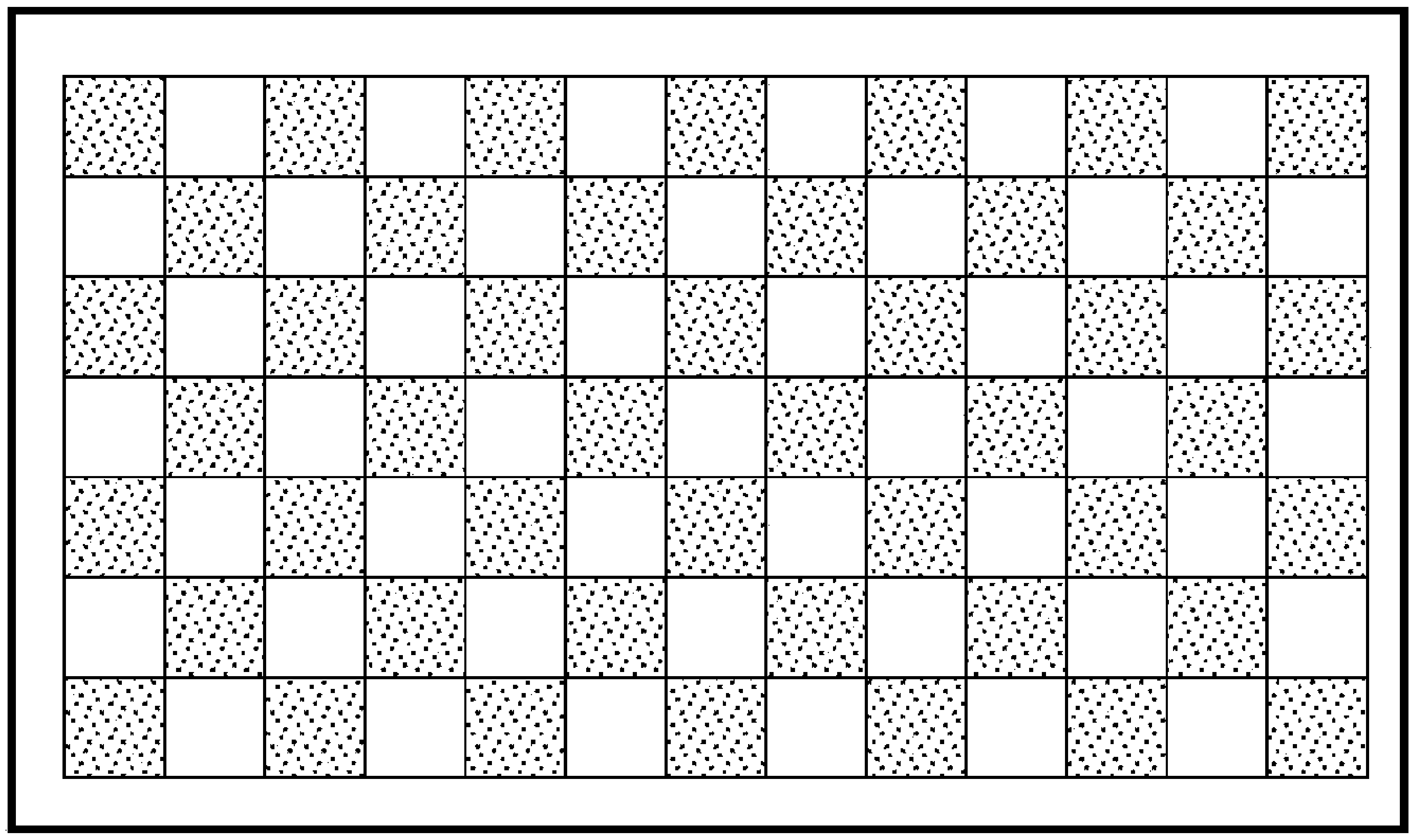

▨ Phase shift

☐ No Phase shift

FIG. 18

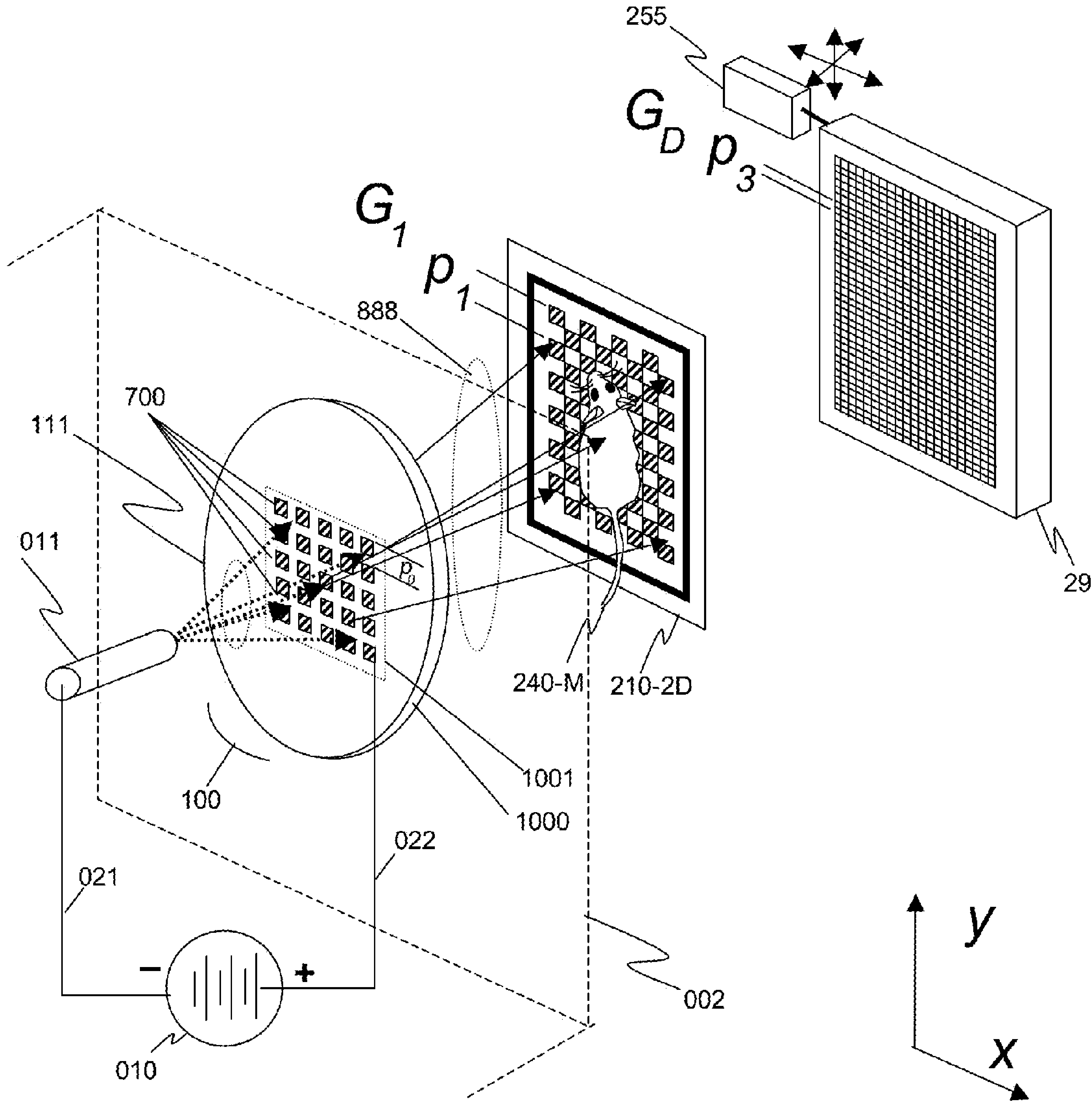
255
G_D
p_3
G_1
p_1
888
700
111
011
p_0
240-M
210-2D
299
1001
100
1000
022
021
−
+
002
010
y
x

FIG. 19

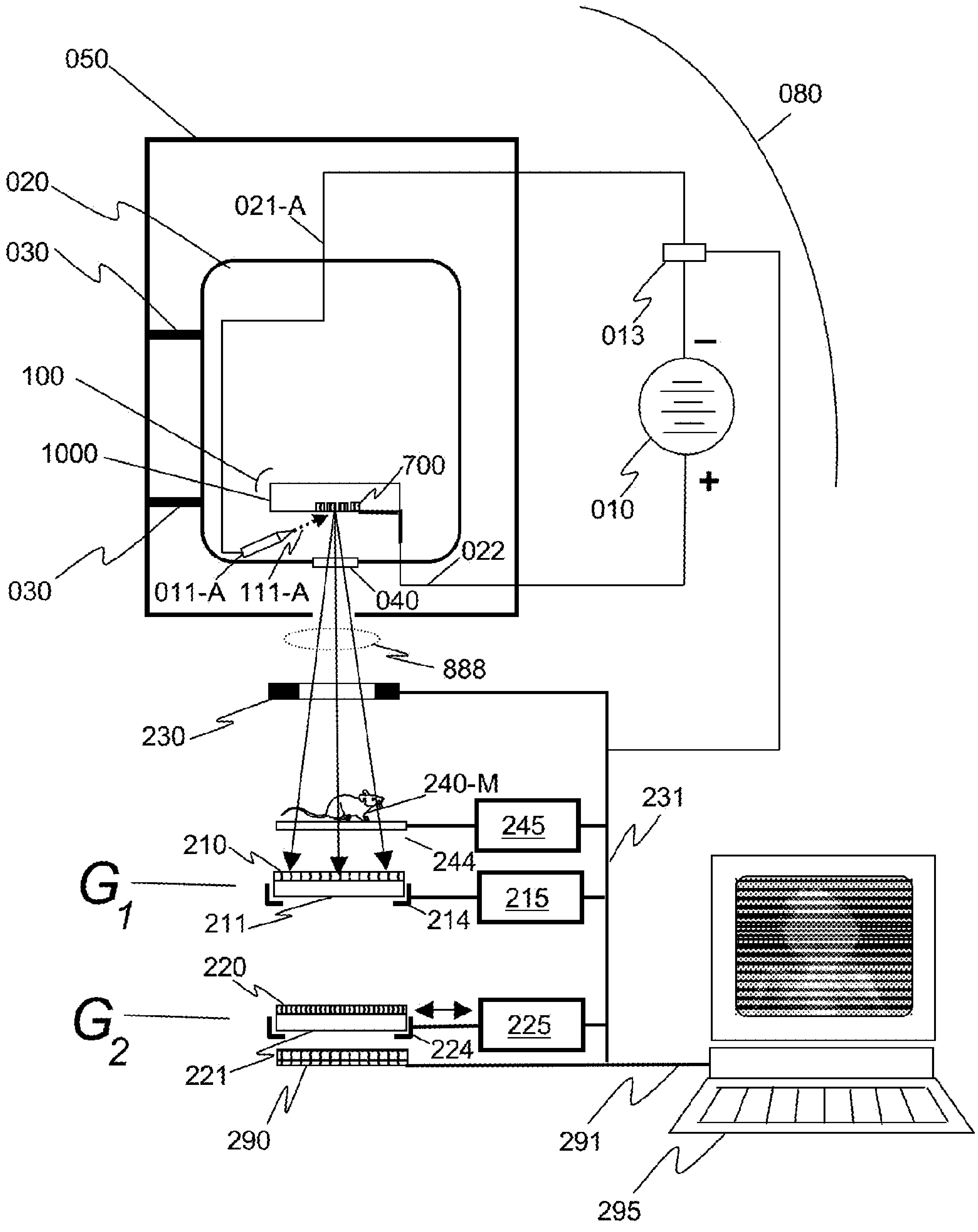
050
080
020
021-A
030
013
100
1000
700
010
022
030
011-A
111-A
040
888
230
240-M
231
245
210
244
G1
215
211
214
220
G2
225
224
221
290
291
295

FIG. 20

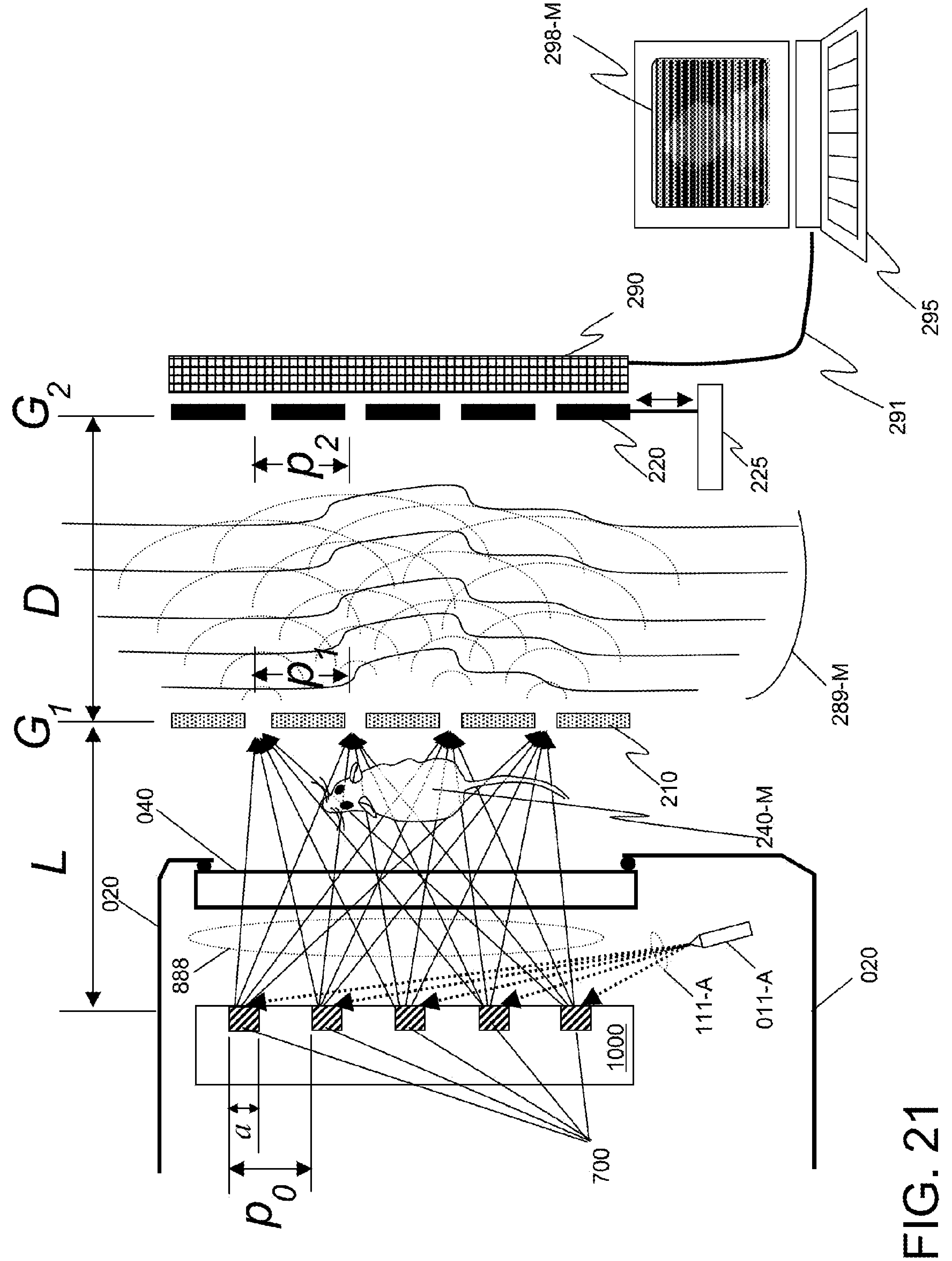
298-M
290
295
291
G_2
p_2
220
225
D
p_1
289-M
G_1
210
240-M
040
L
020
888
111-A
011-A
020
1000
a
p_0
700

FIG. 21

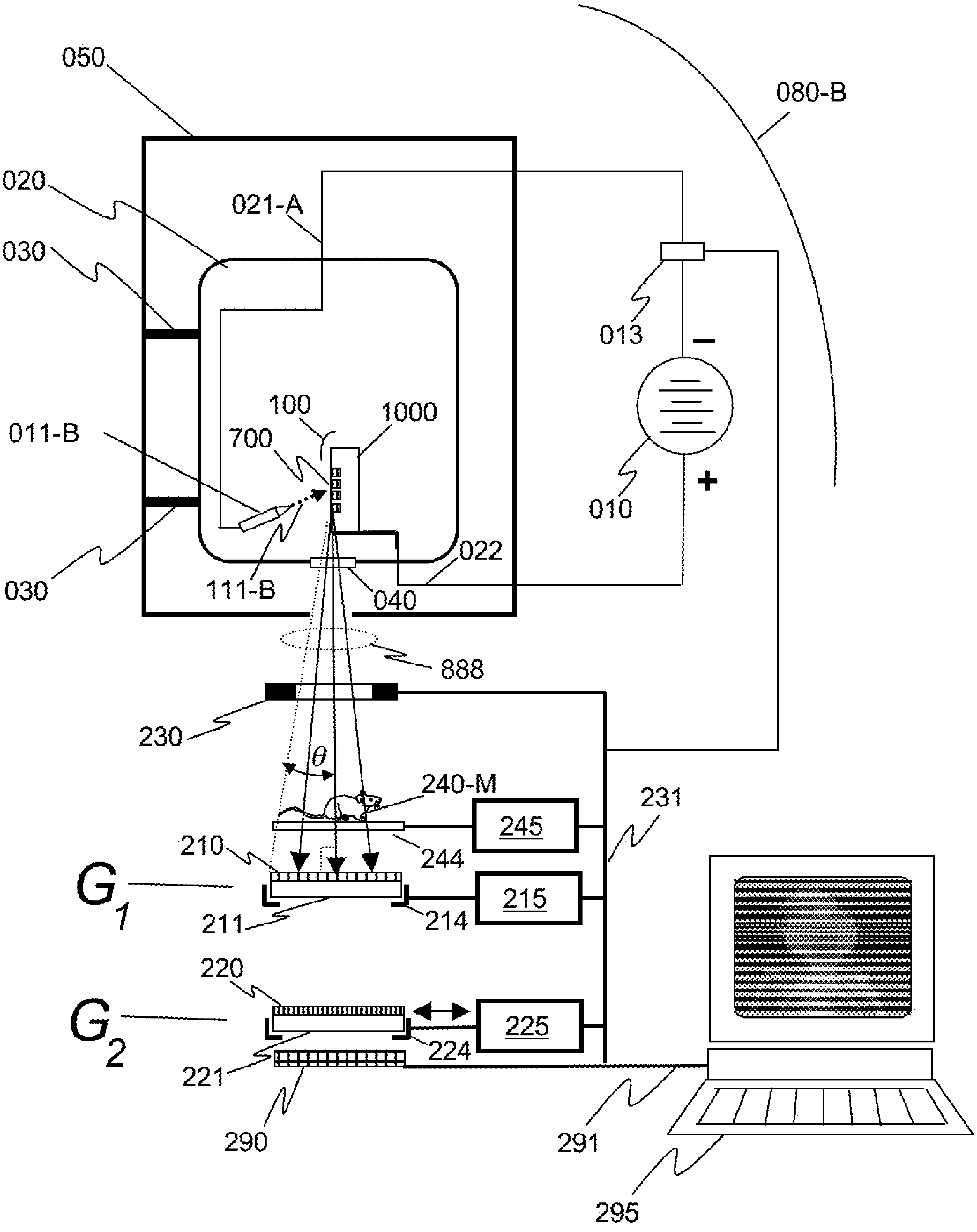
050
080-B
020
021-A
030
013
100
1000
011-B
700
010
030
111-B
040
022
888
230
θ
240-M
231
245
210
244
G1
215
211
214
220
G2
225
221
224
290
291
295

FIG. 22

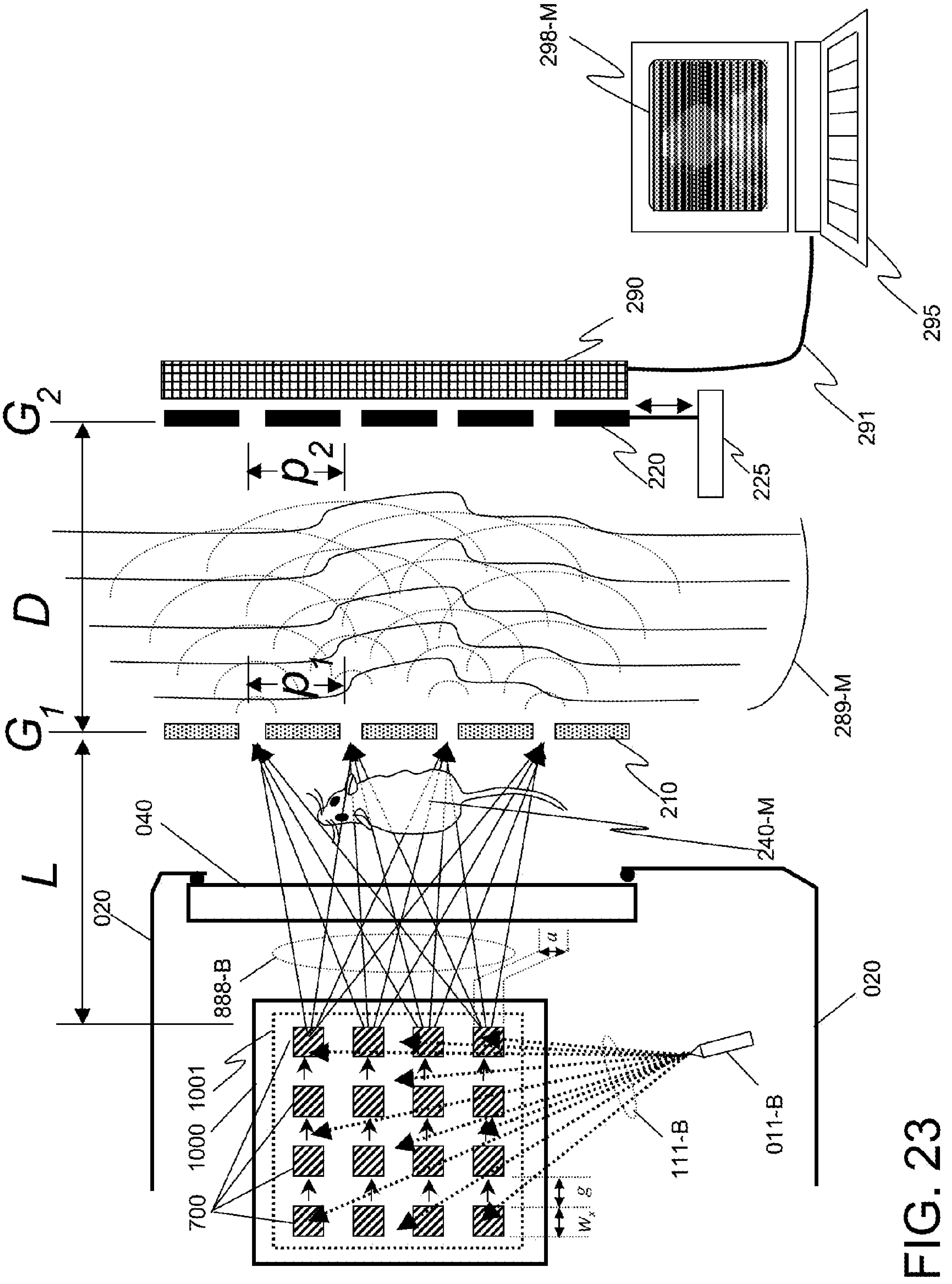
298-M
290
295
291
G_2
p_2
220
225
D
p_1
289-M
G_1
210
040
240-M
L
020
888-B
u
020
1000
1001
700
111-B
011-B
g
w_x

FIG. 23

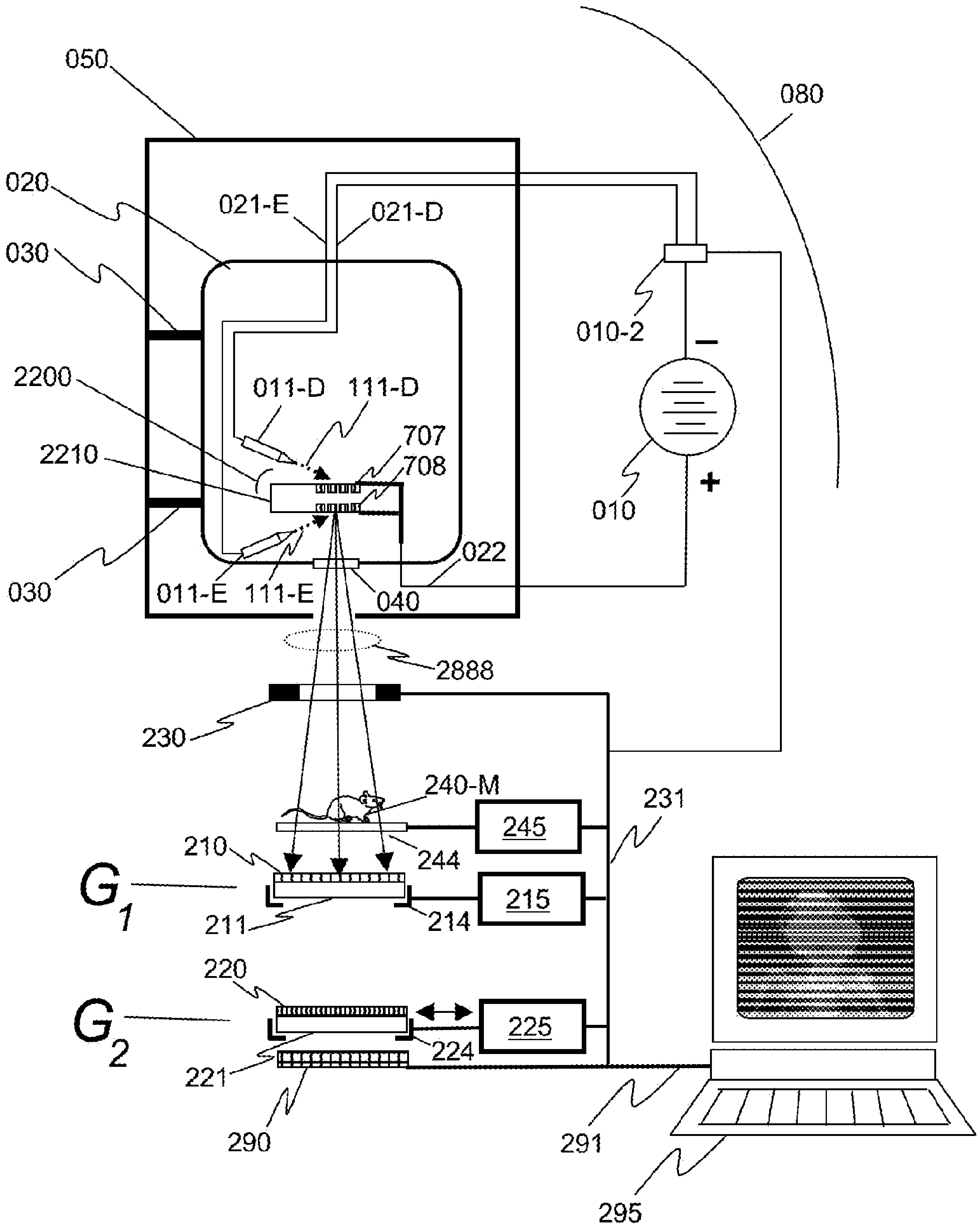
050
080
020
021-E
021-D
030
010-2
2200
011-D
111-D
707
708
2210
010
022
030
011-E
111-E
040
2888
230
240-M
231
245
210
244
G_1
215
211
214
220
G_2
225
224
221
290
291
295

FIG. 24

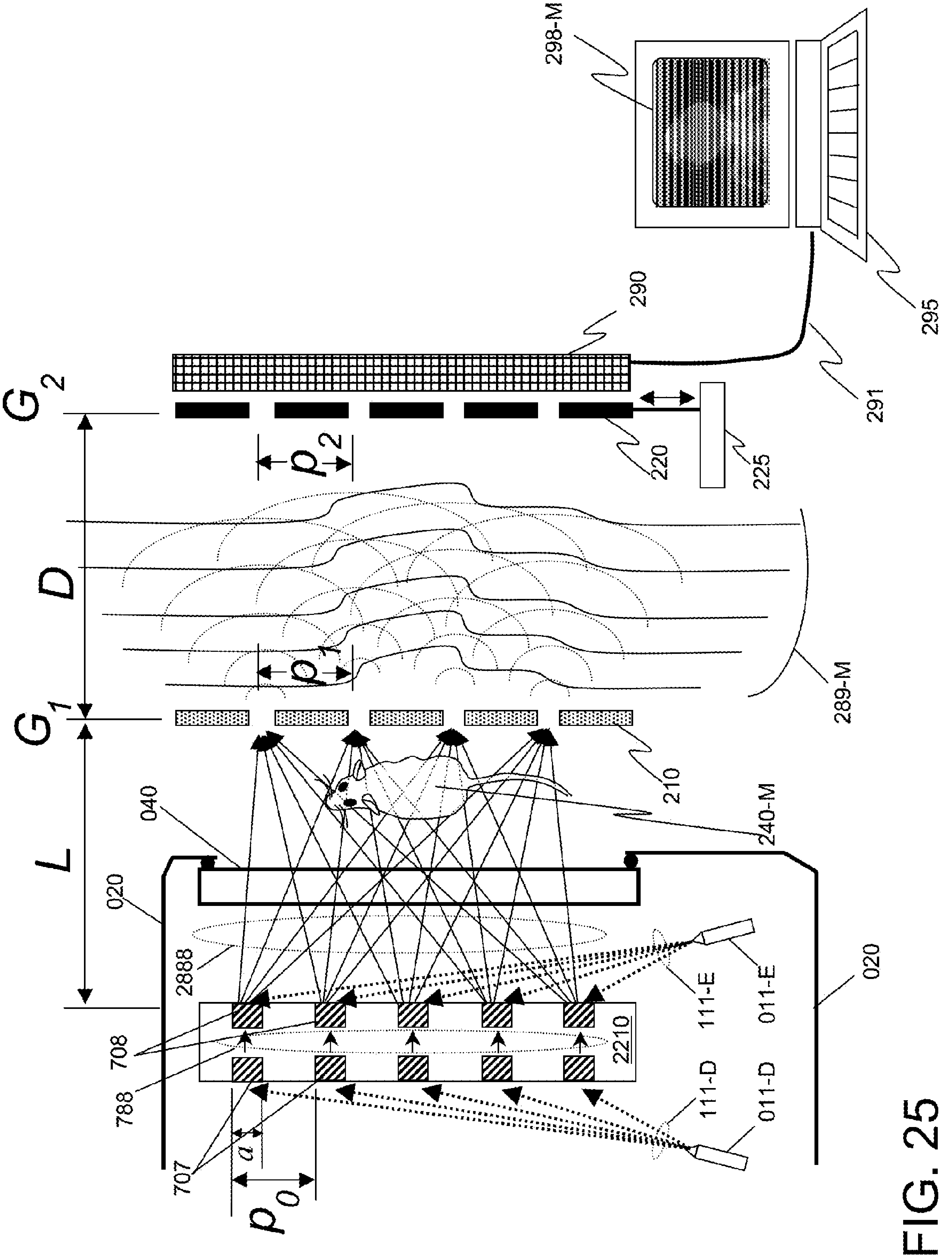
298-M
290
295
291
G_2
p_2
220
225
D
p_1
289-M
G_1
210
240-M
040
L
020
2888
111-E
011-E
020
708
788
2210
111-D
011-D
707
a
p_0

FIG. 25

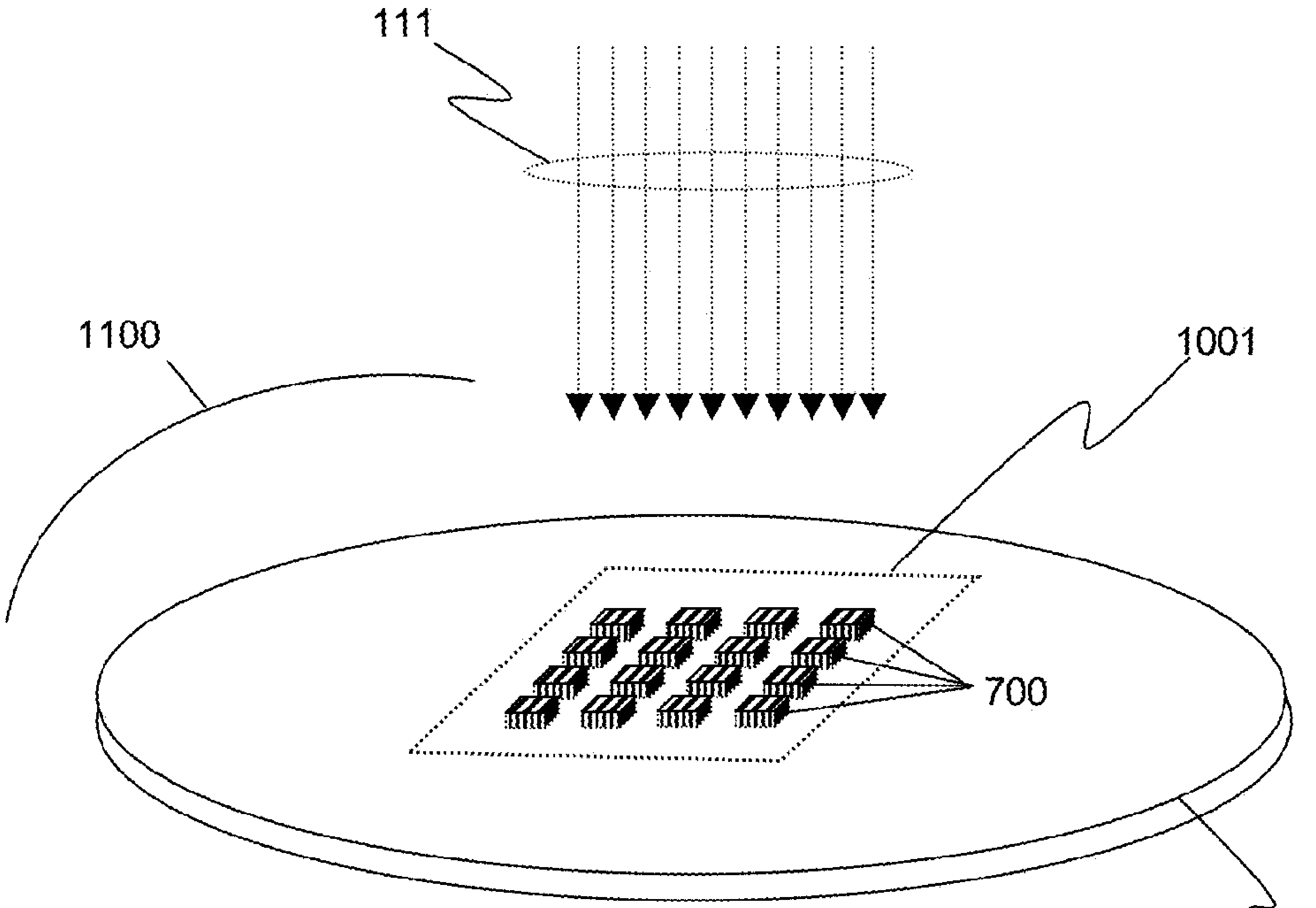

FIG. 26

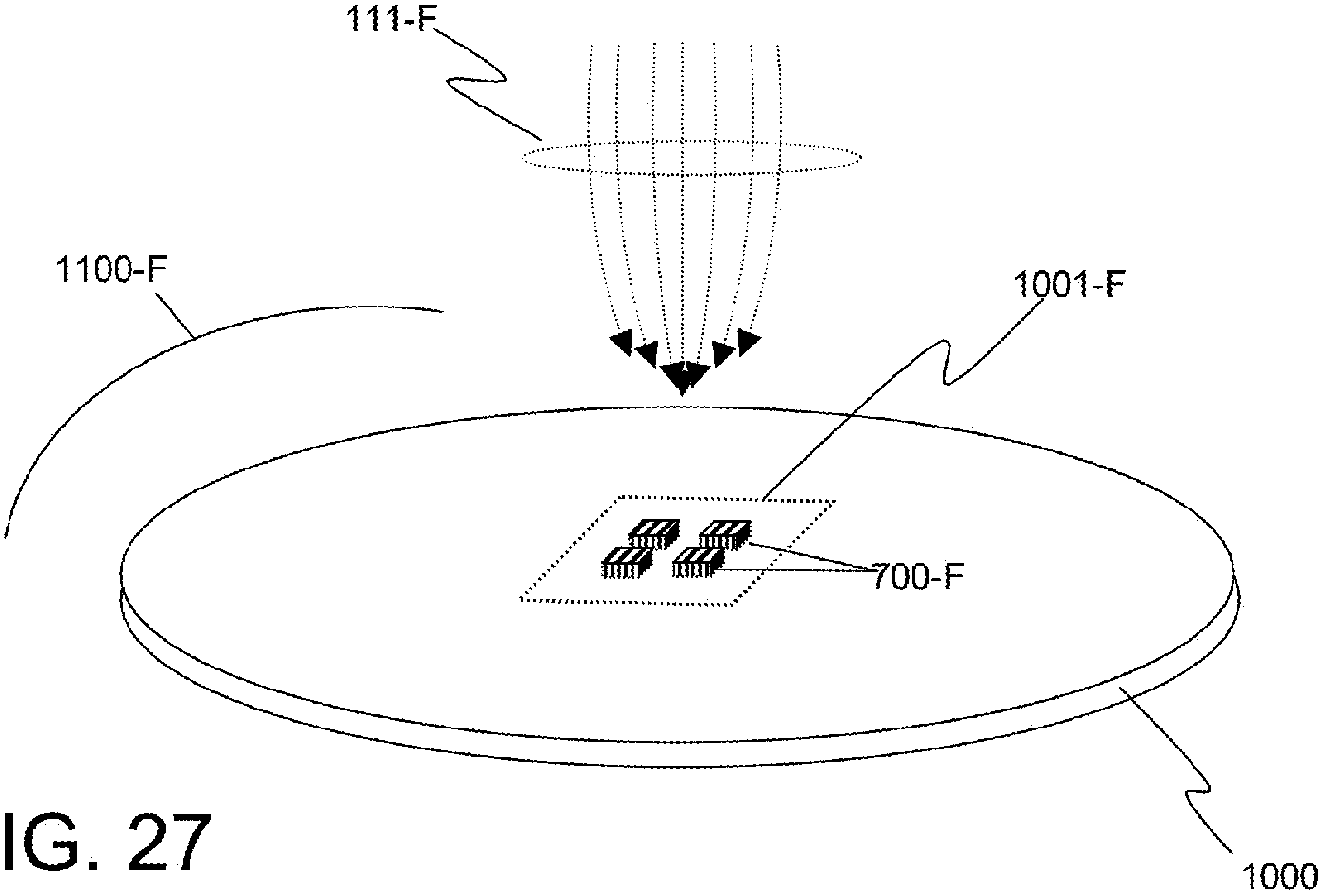

FIG. 27

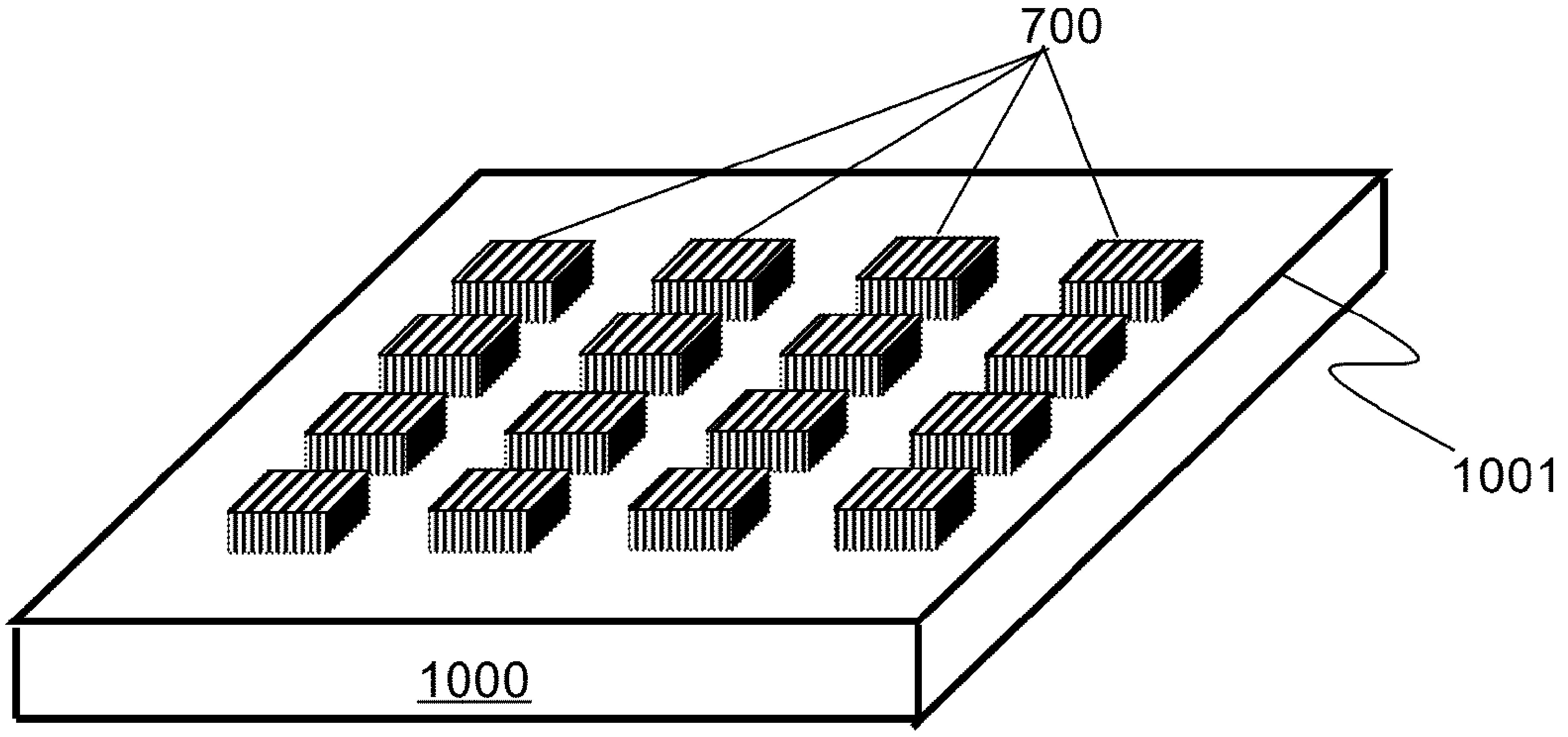

FIG. 28A

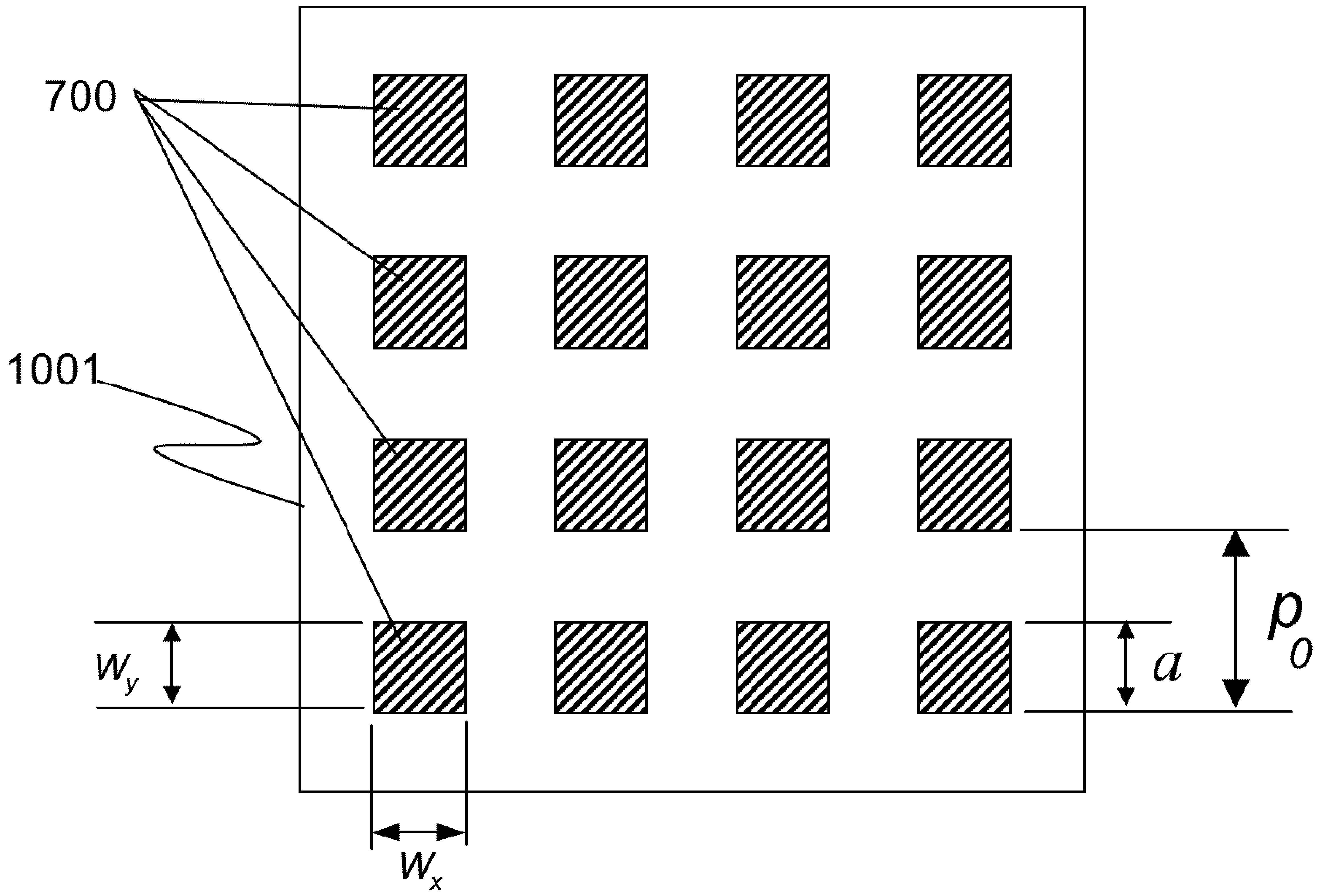

FIG. 28B

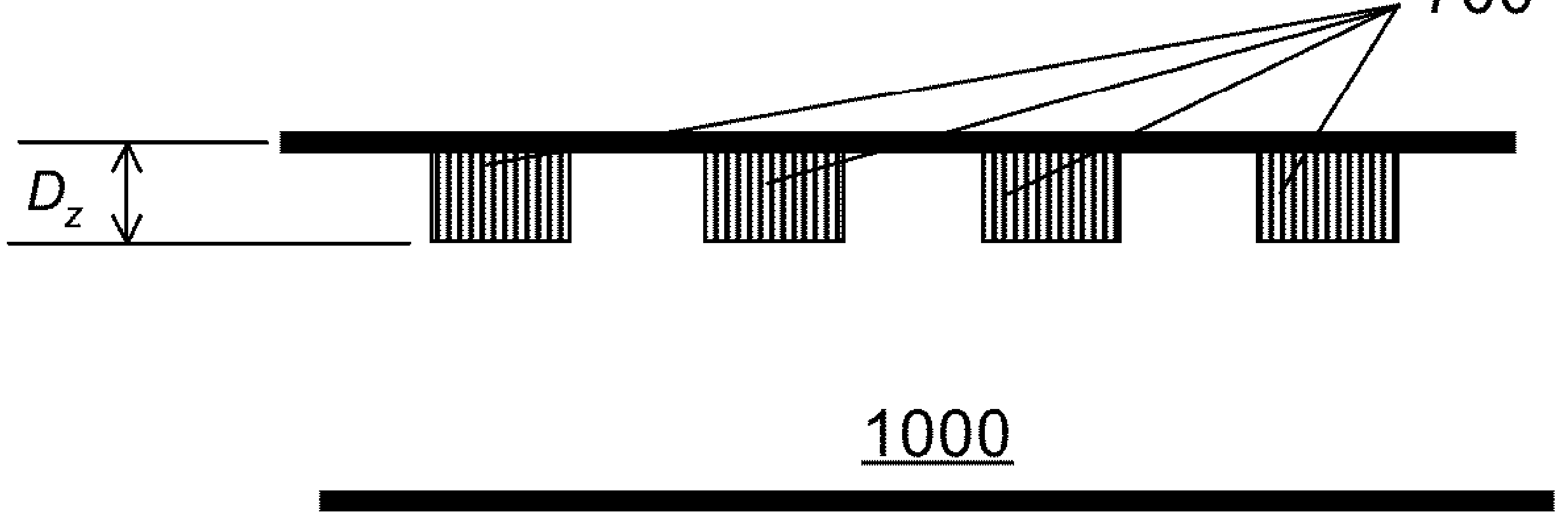

FIG. 28C

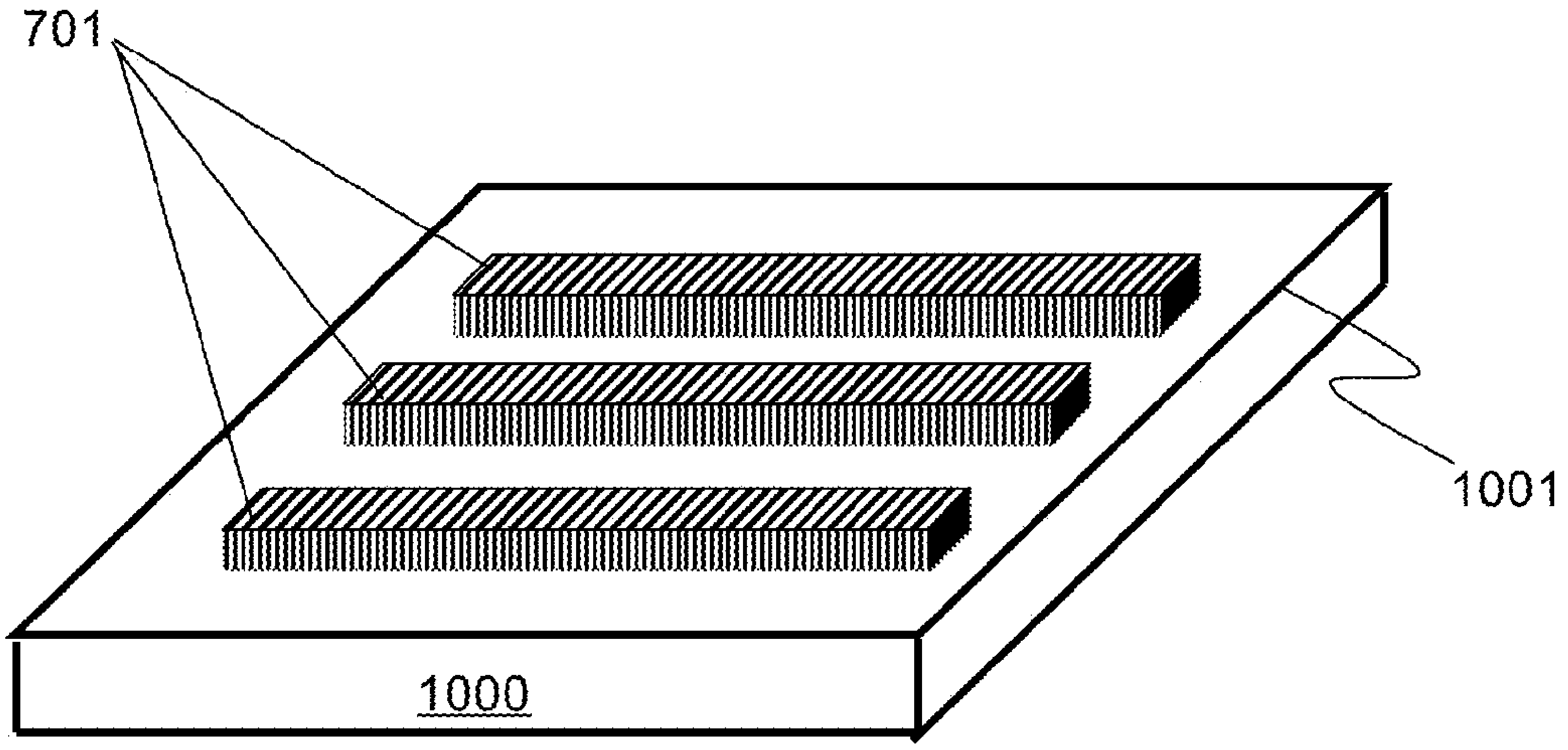

FIG. 29A

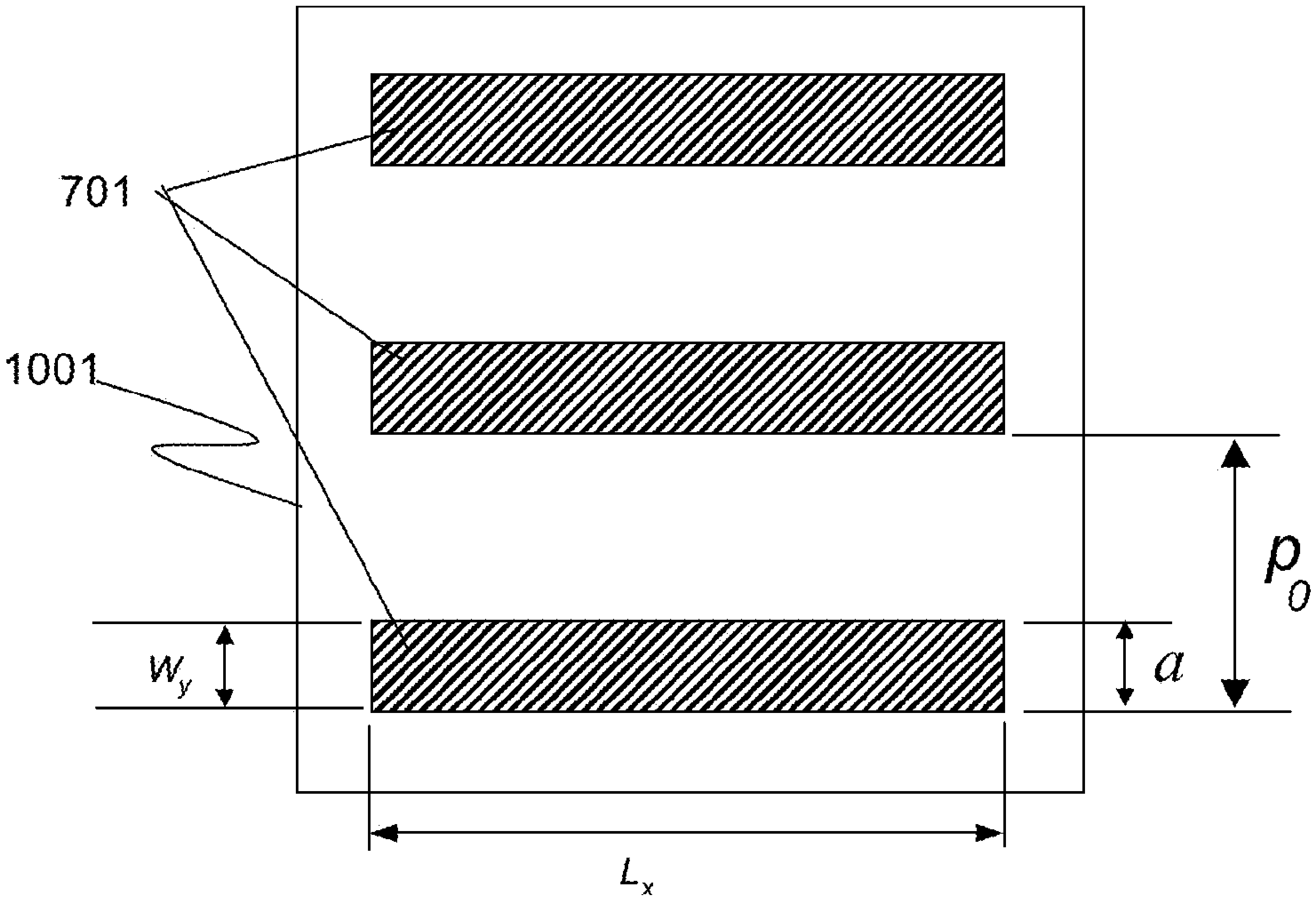

FIG. 29B

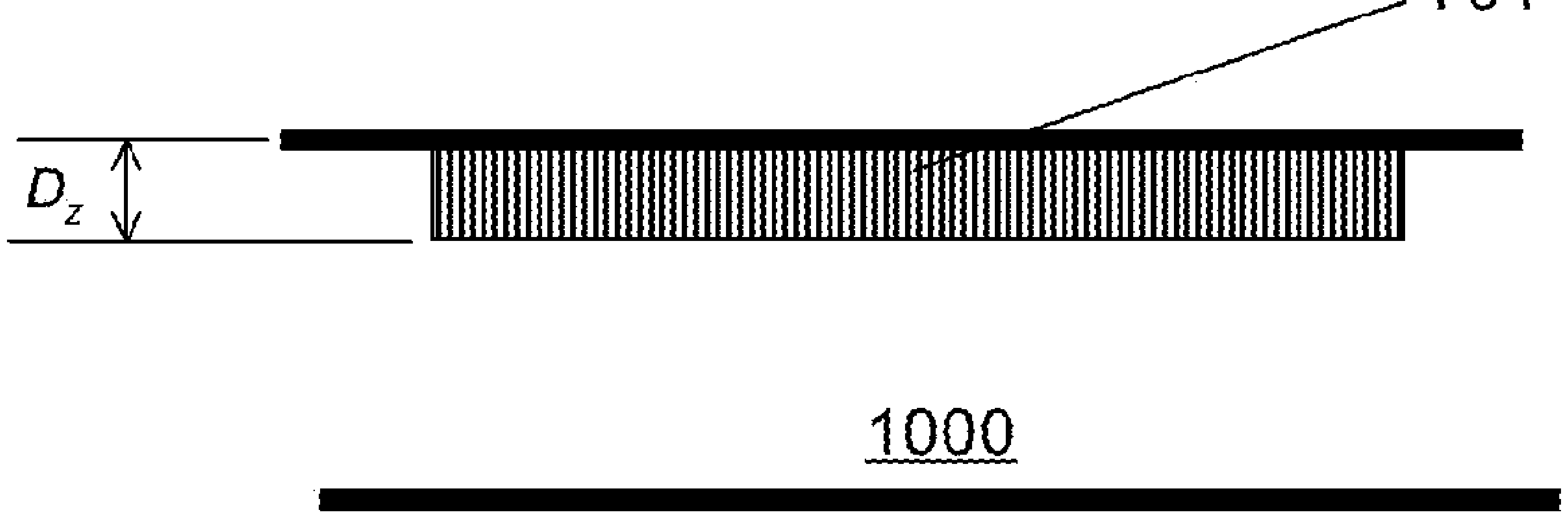

FIG. 29C

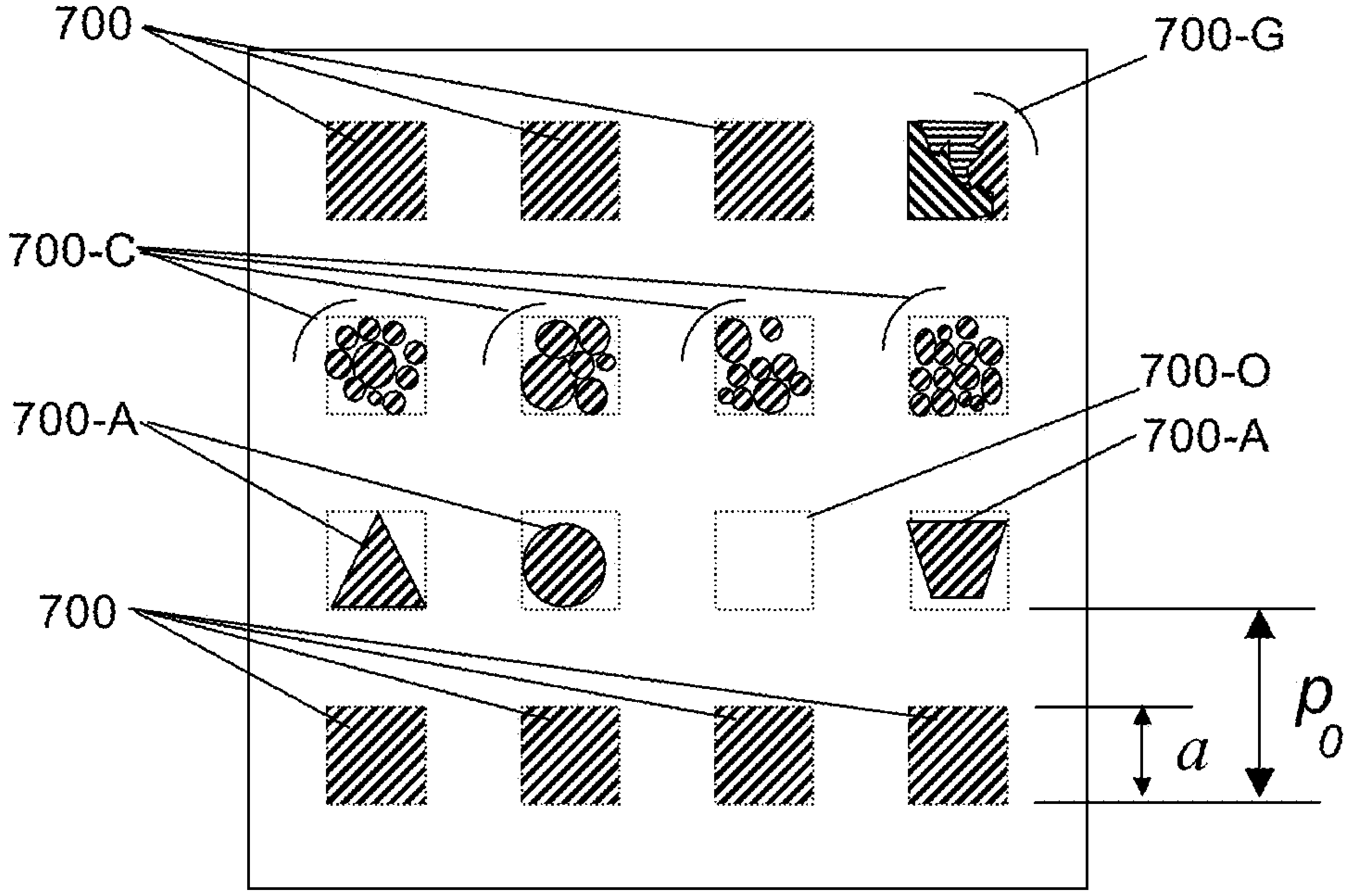
700
700-G
700-C
700-O
700-A
700-A
700
p_0
a

FIG. 30

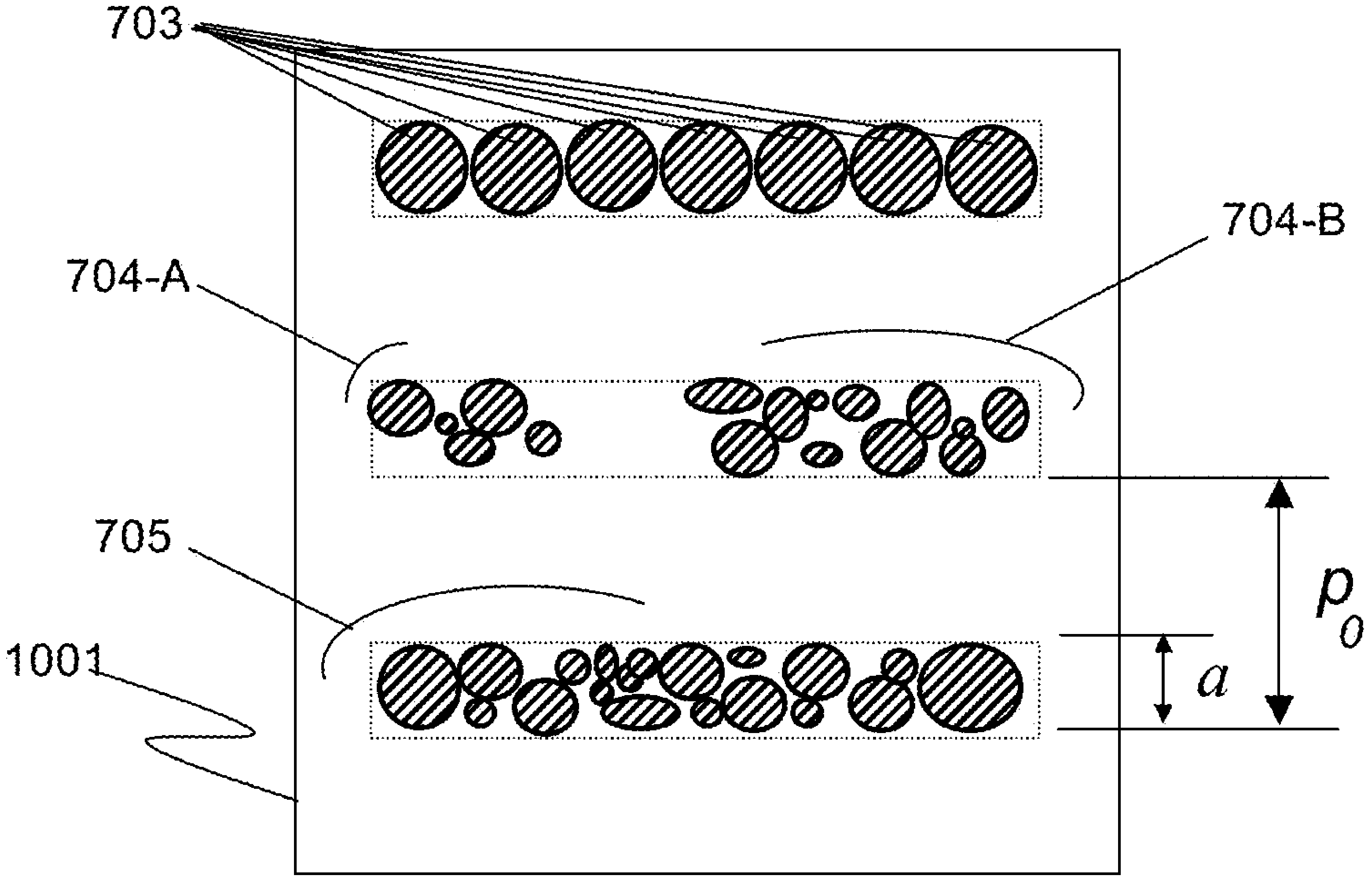
703
704-B
704-A
705
1001
p_0
a

FIG. 31

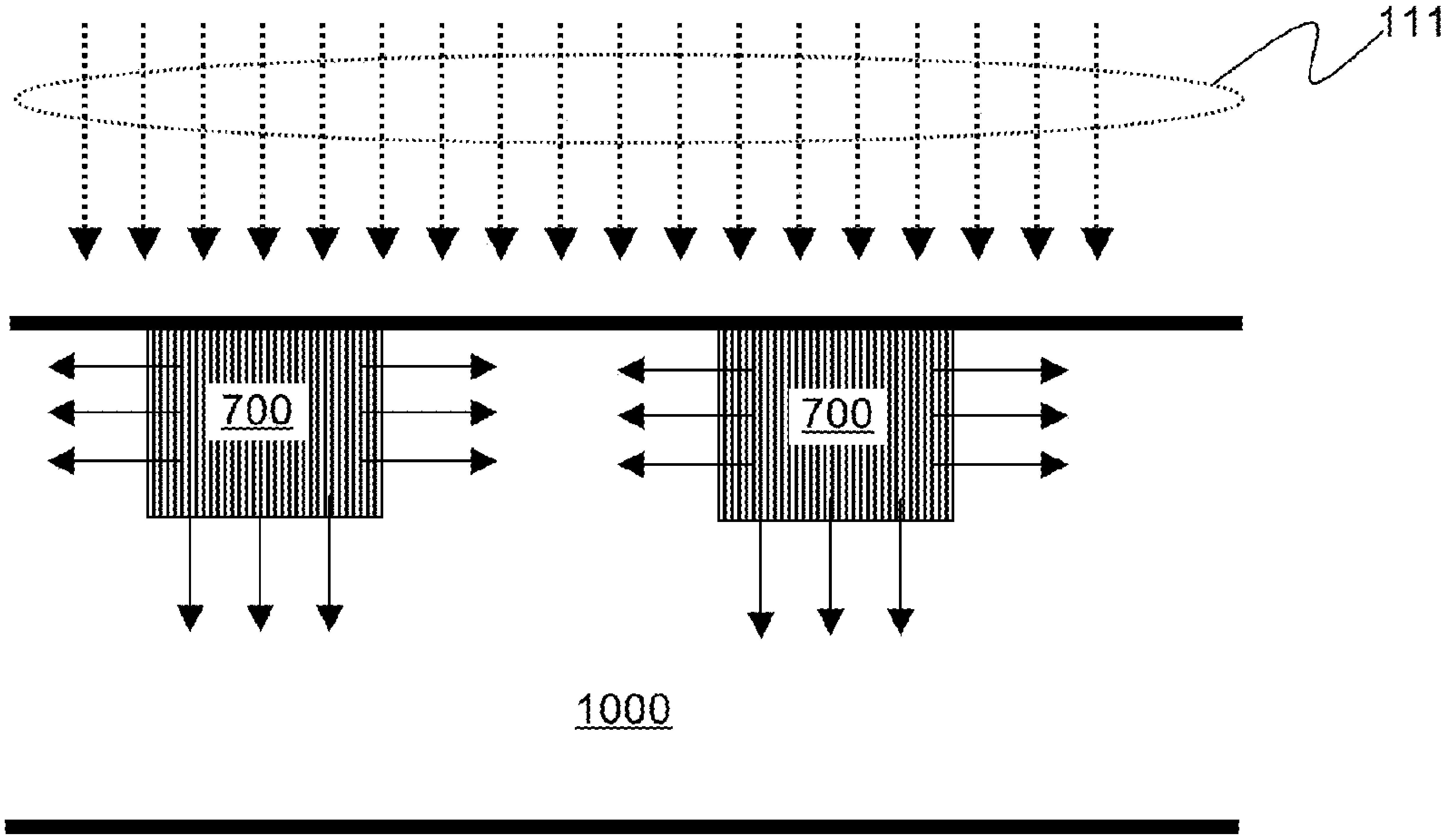

FIG. 32

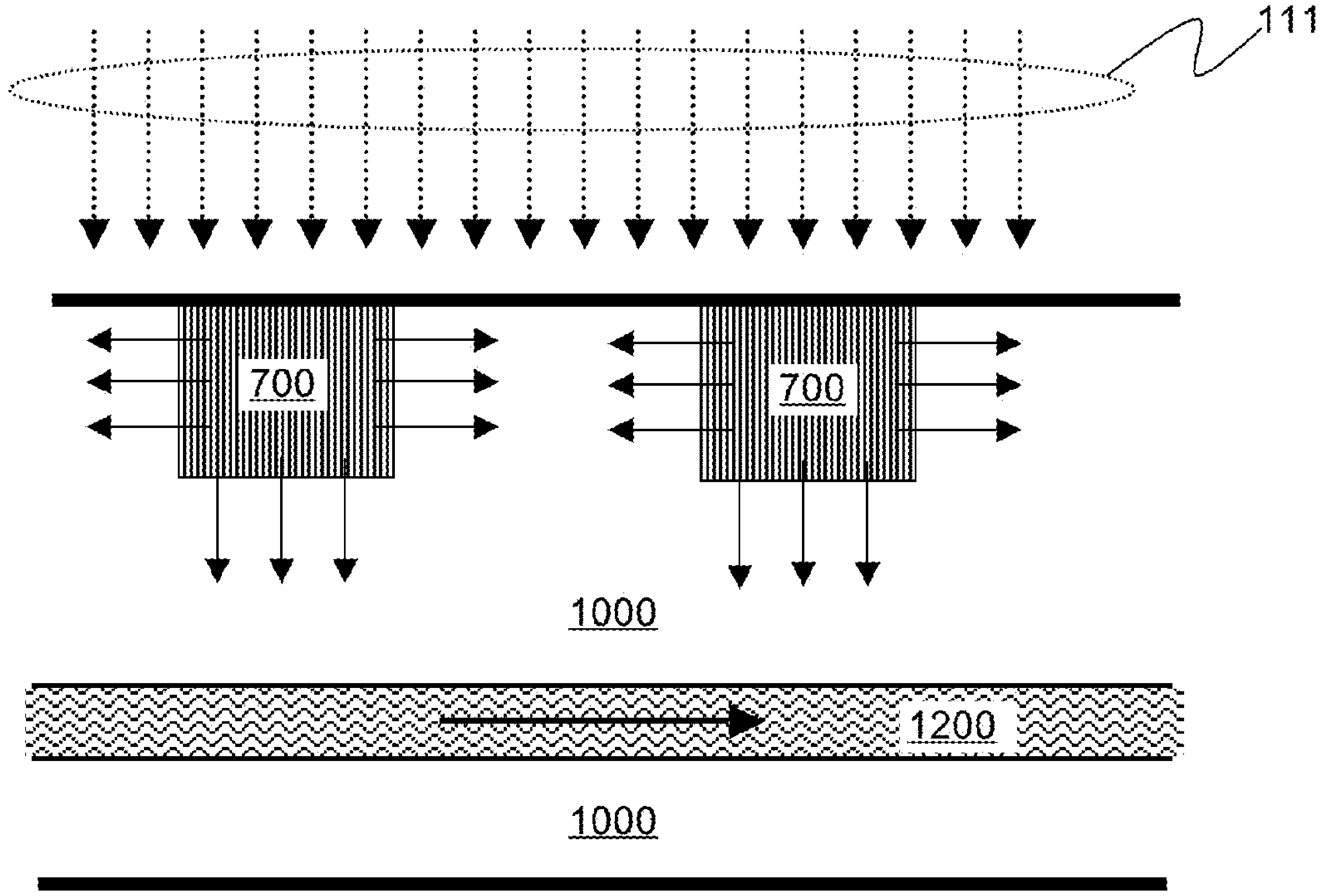

FIG. 33

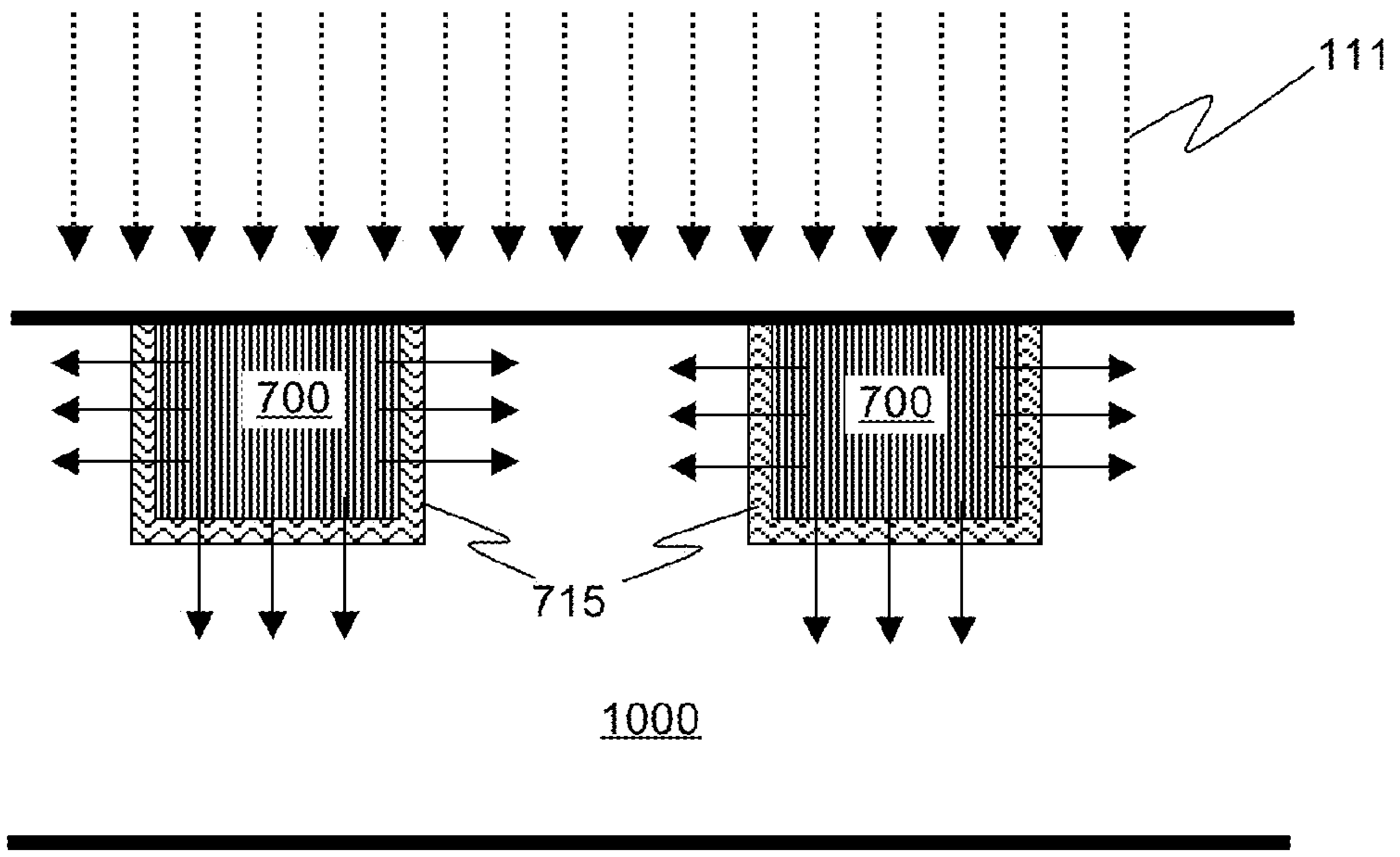

FIG. 34

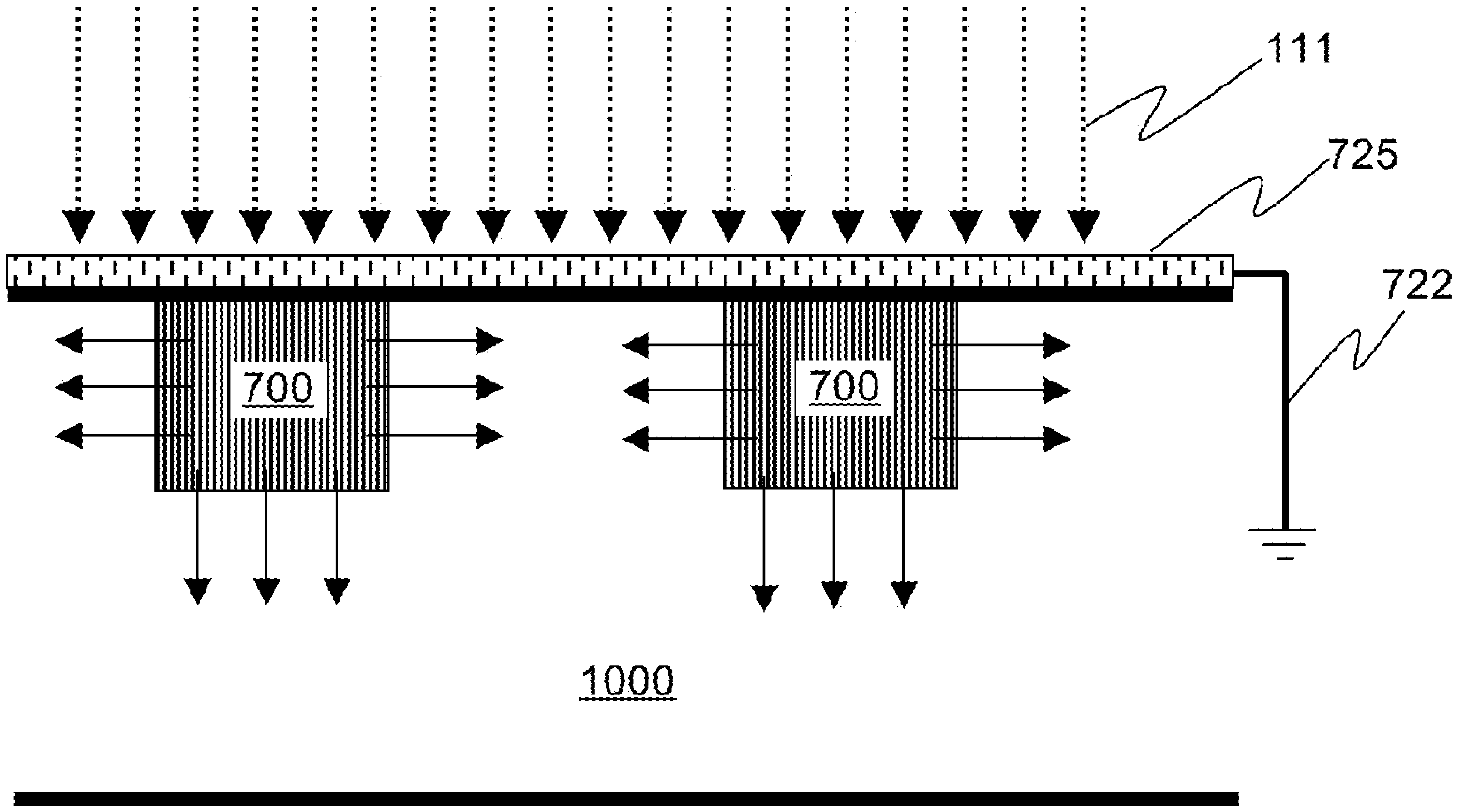

FIG. 35

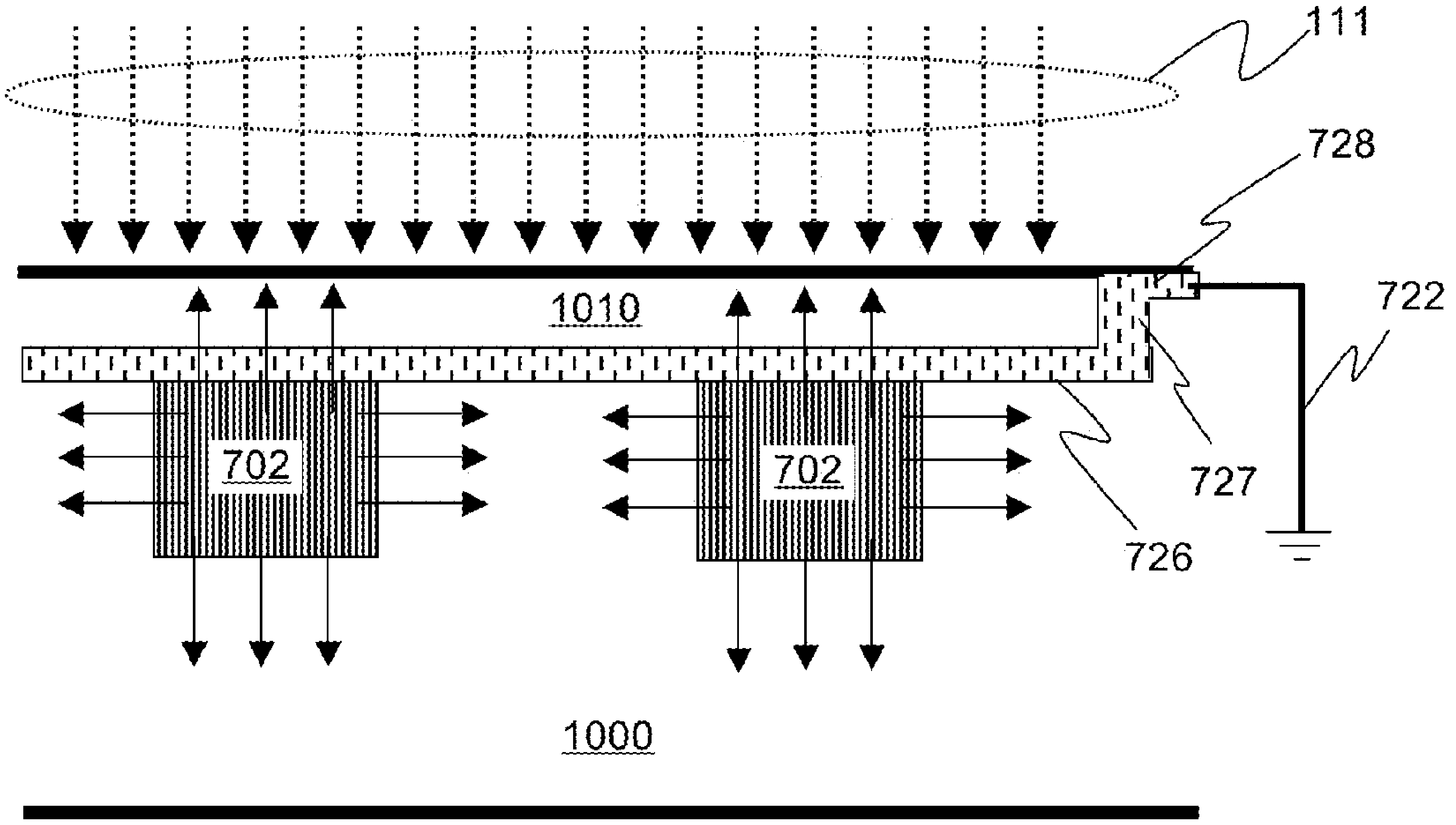

FIG. 36

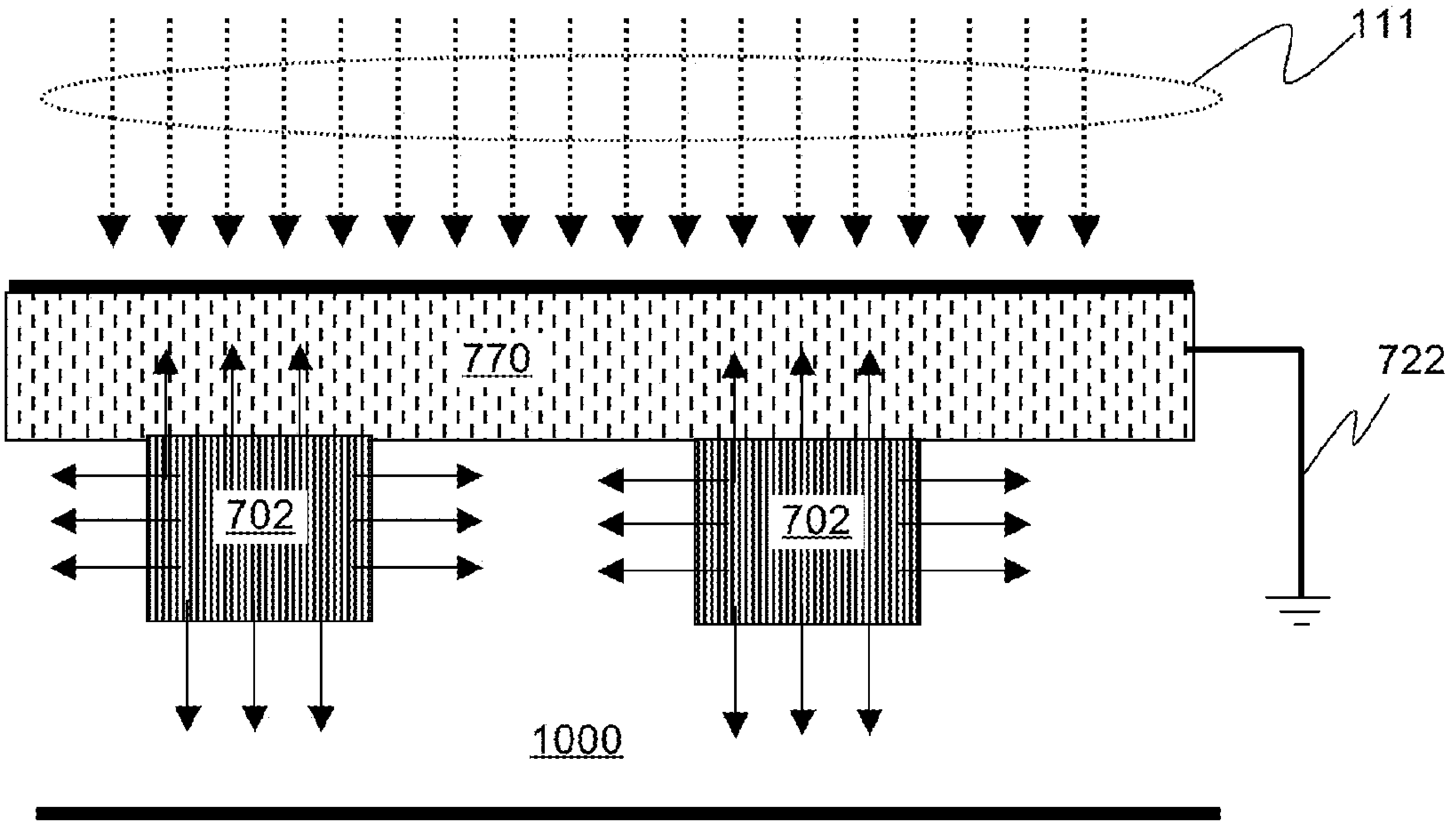

FIG. 37

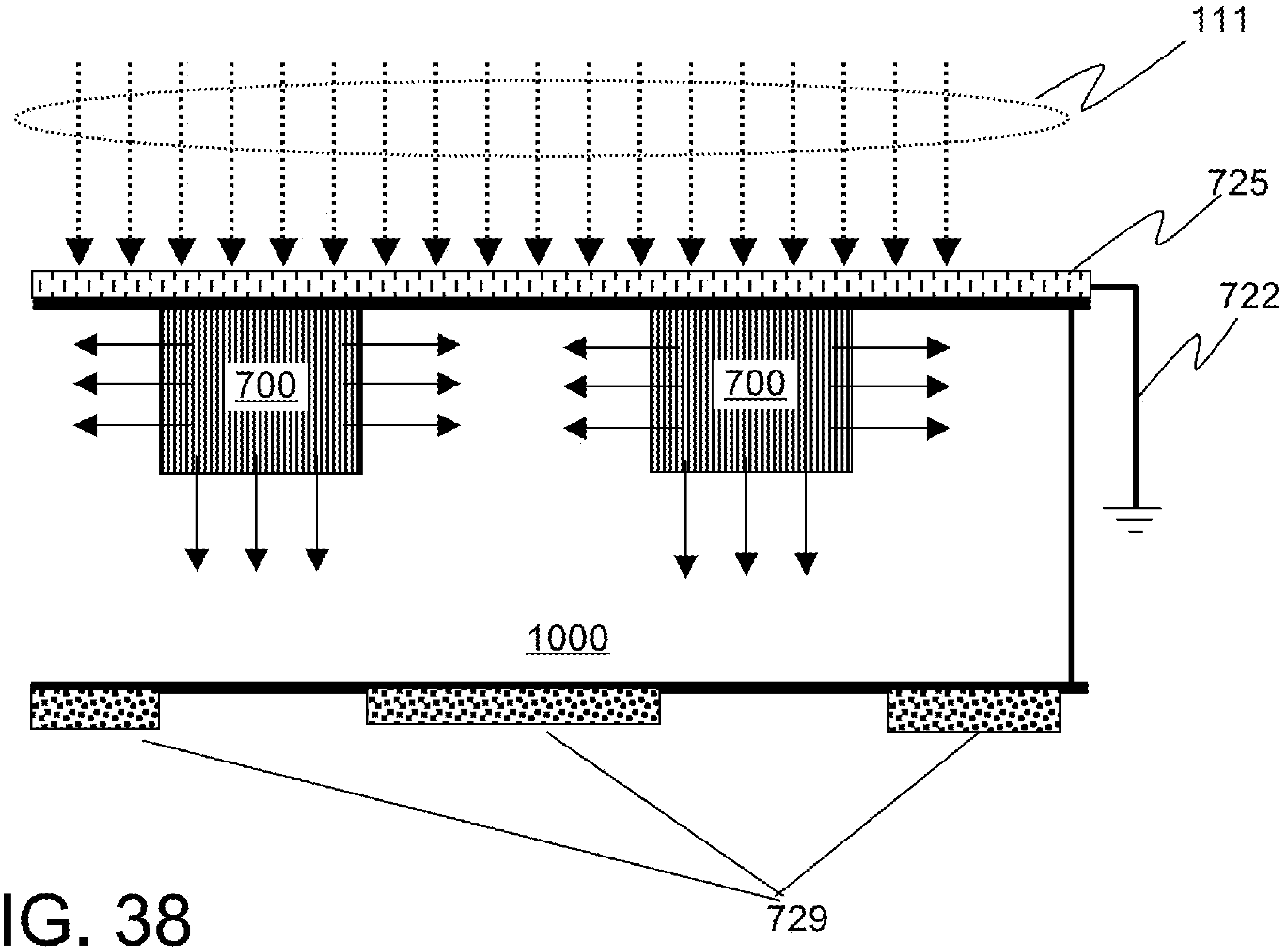

FIG. 38

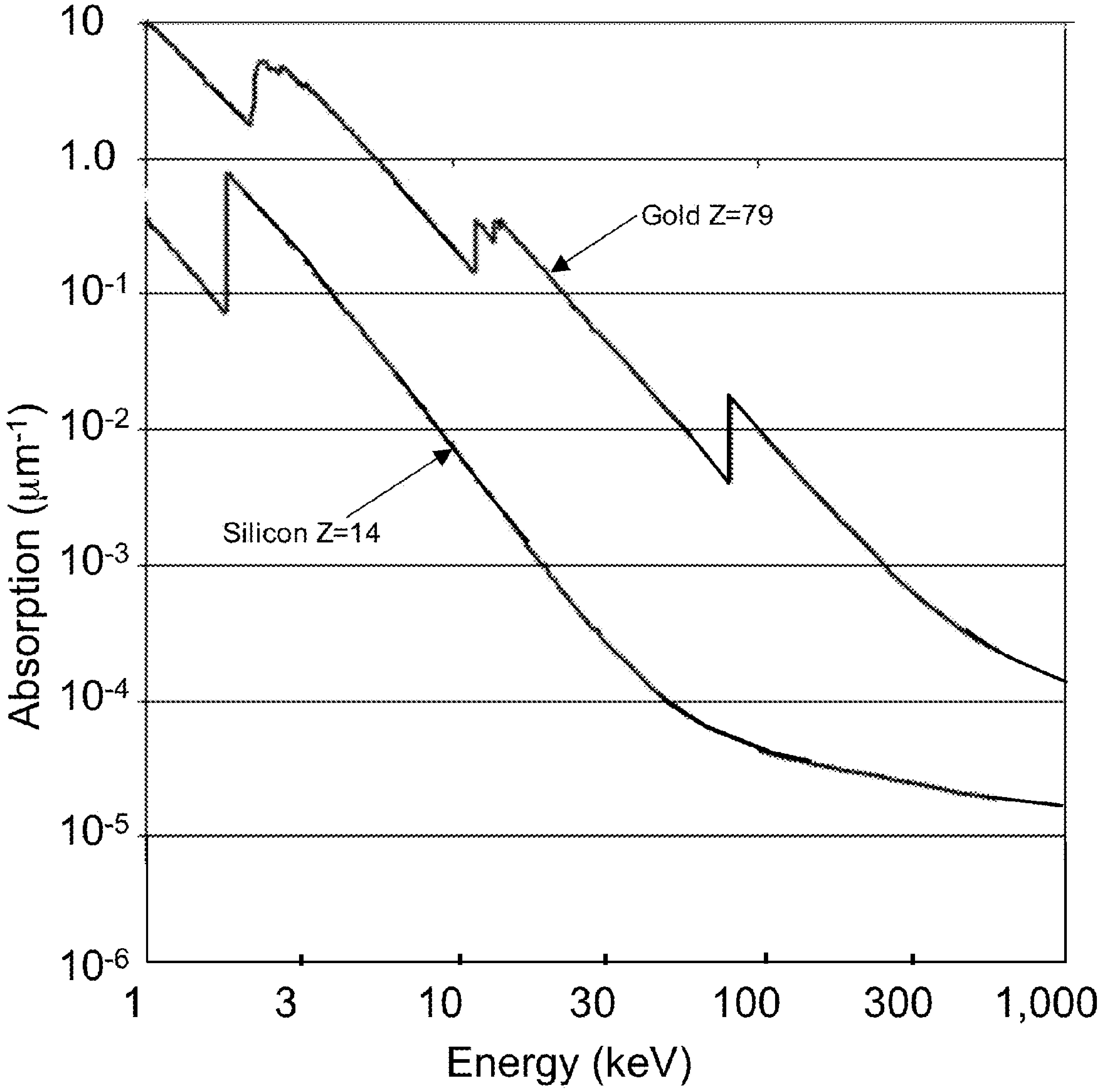
10
1.0
10^{-1}
10^{-2}
10^{-3}
10^{-4}
10^{-5}
10^{-6}
Absorption (μm^{-1})
Gold Z=79
Silicon Z=14
1
3
10
30
100
300
1,000
Energy (keV)

FIG. 39

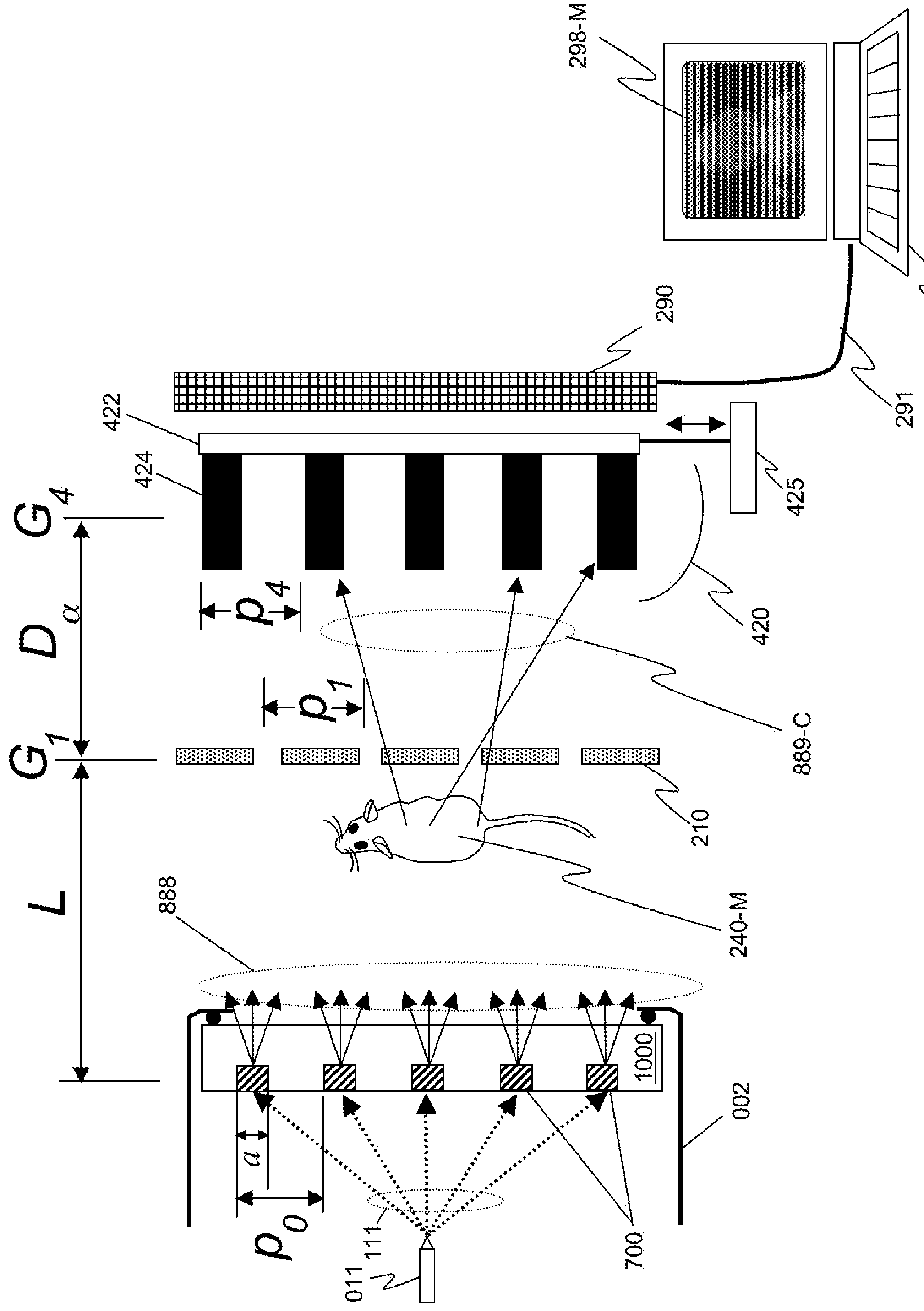
298-M
290
295
291
422
424
425
420
G_4
D_α
G_1
L
p_4
p_1
889-C
210
240-M
888
1000
002
a
p_0
700
111
011

FIG. 40

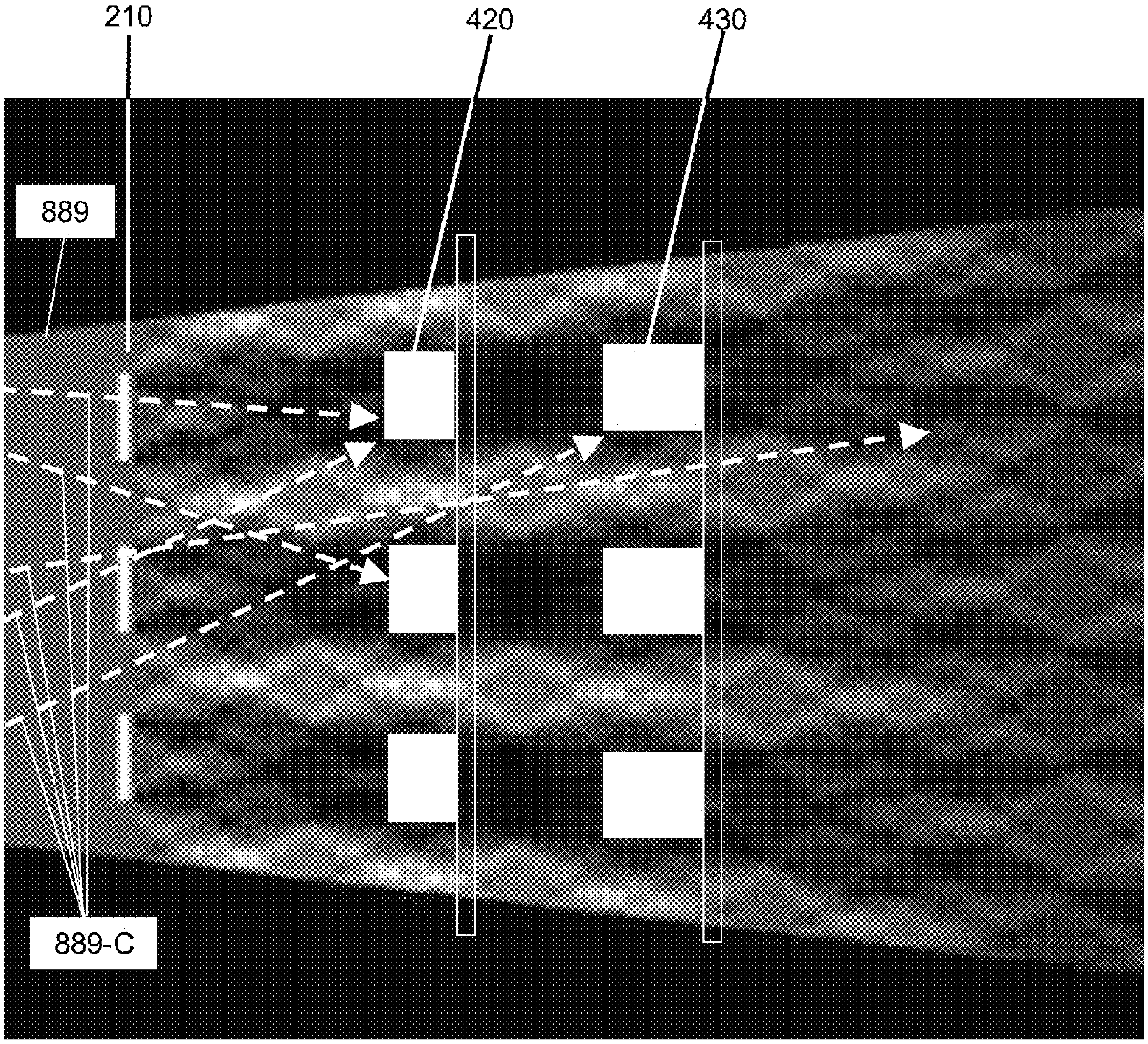

FIG. 41

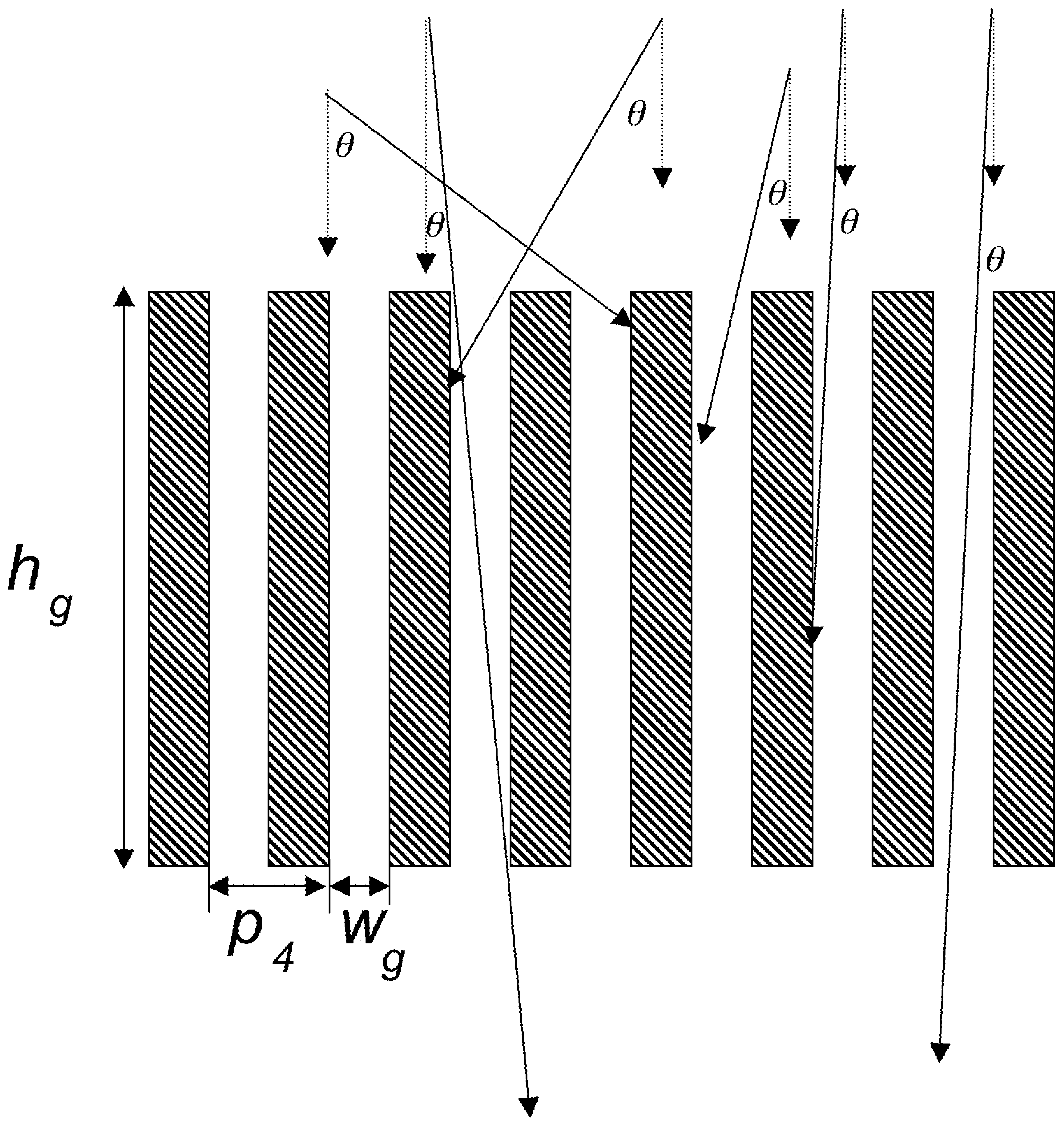

FIG. 42

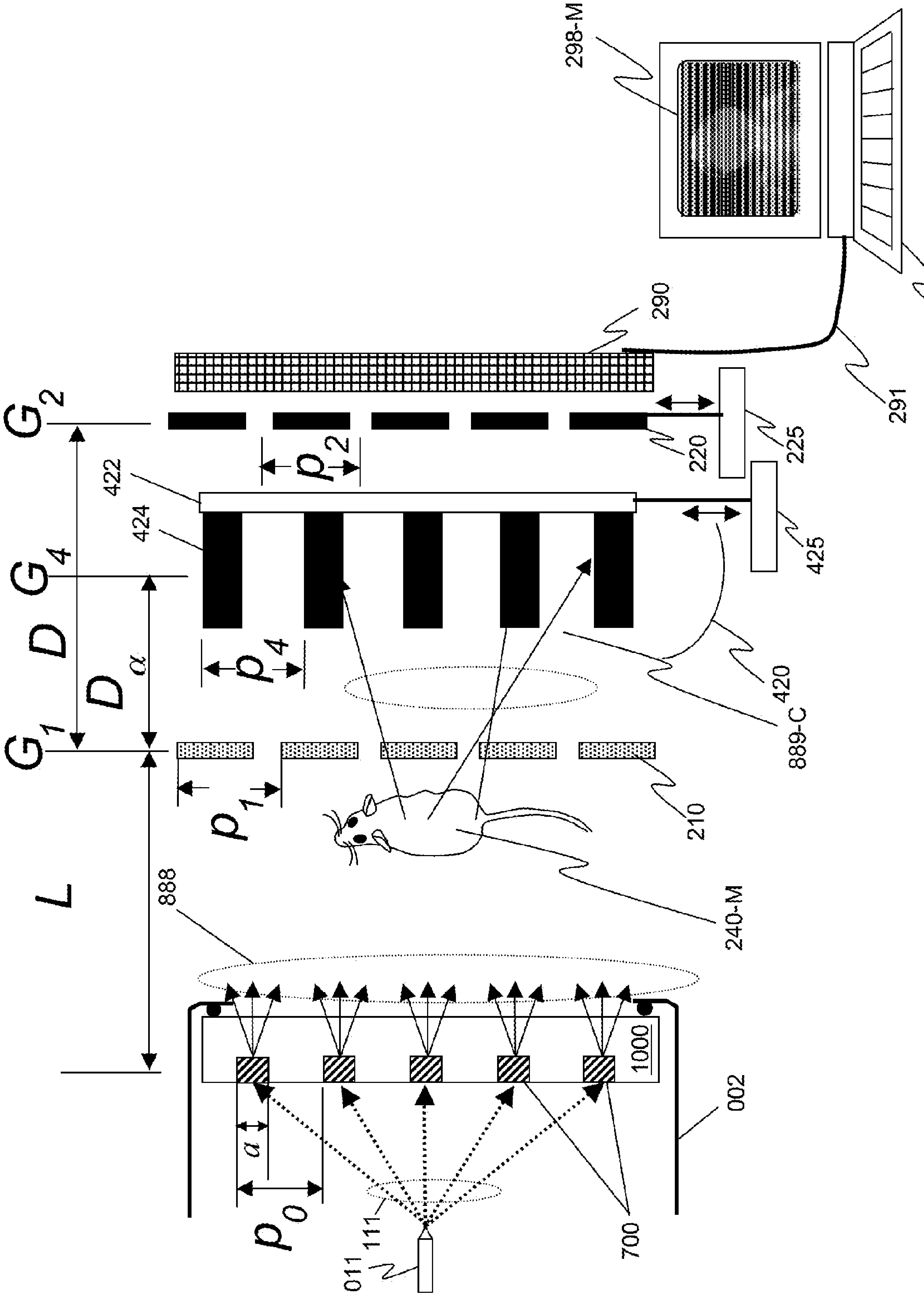
298-M
290
295
291
G_2
p_2
220
225
422
424
G_4
425
D
D_α
p_4
420
889-C
G_1
p_1
210
240-M
L
888
1000
002
a
p_0
111
011
700

FIG. 43

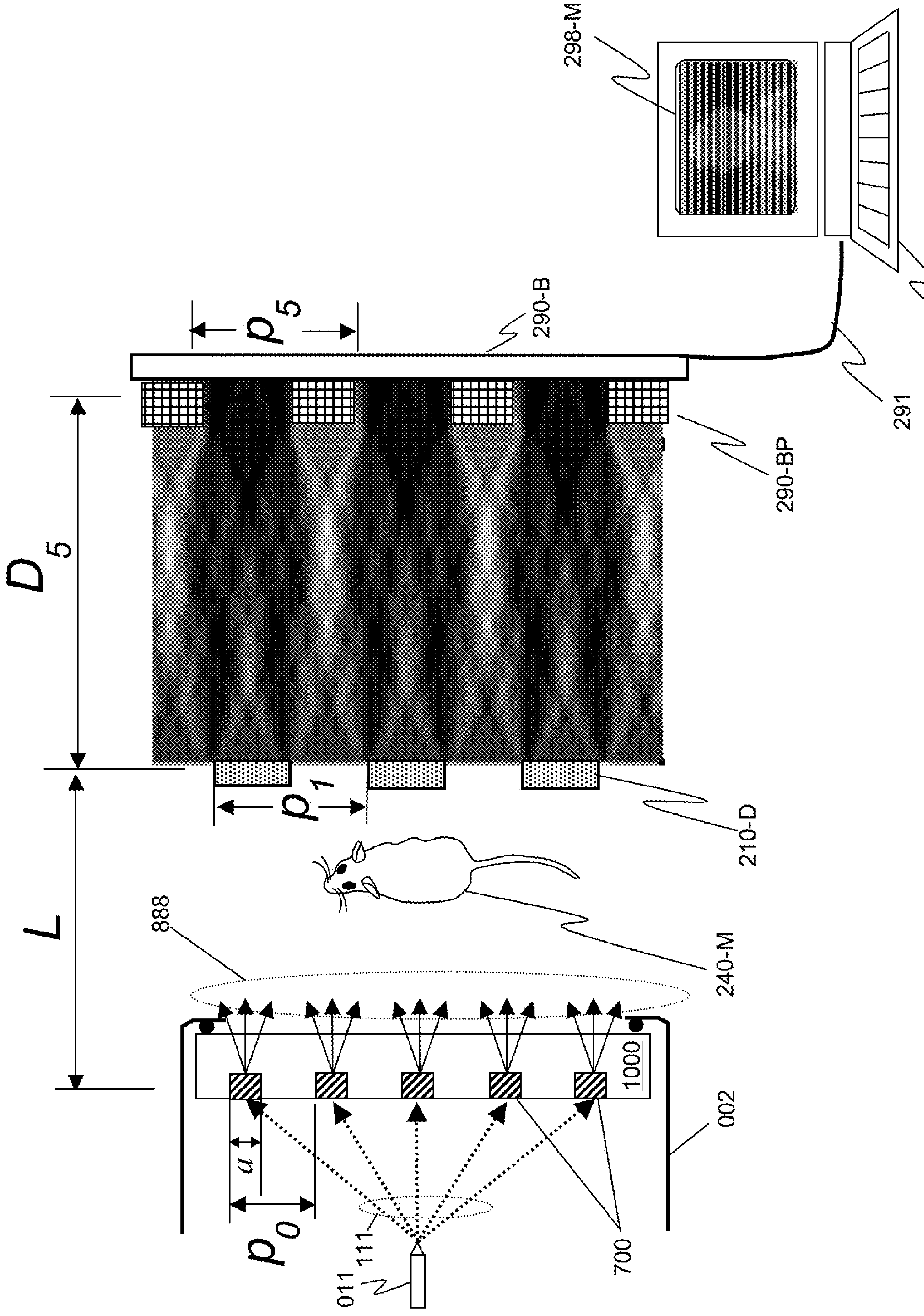
298-M
295
291
290-B
p_5
D_5
290-BP
210-D
p_1
L
888
240-M
1000
002
a
p_0
111
011
700

FIG. 44

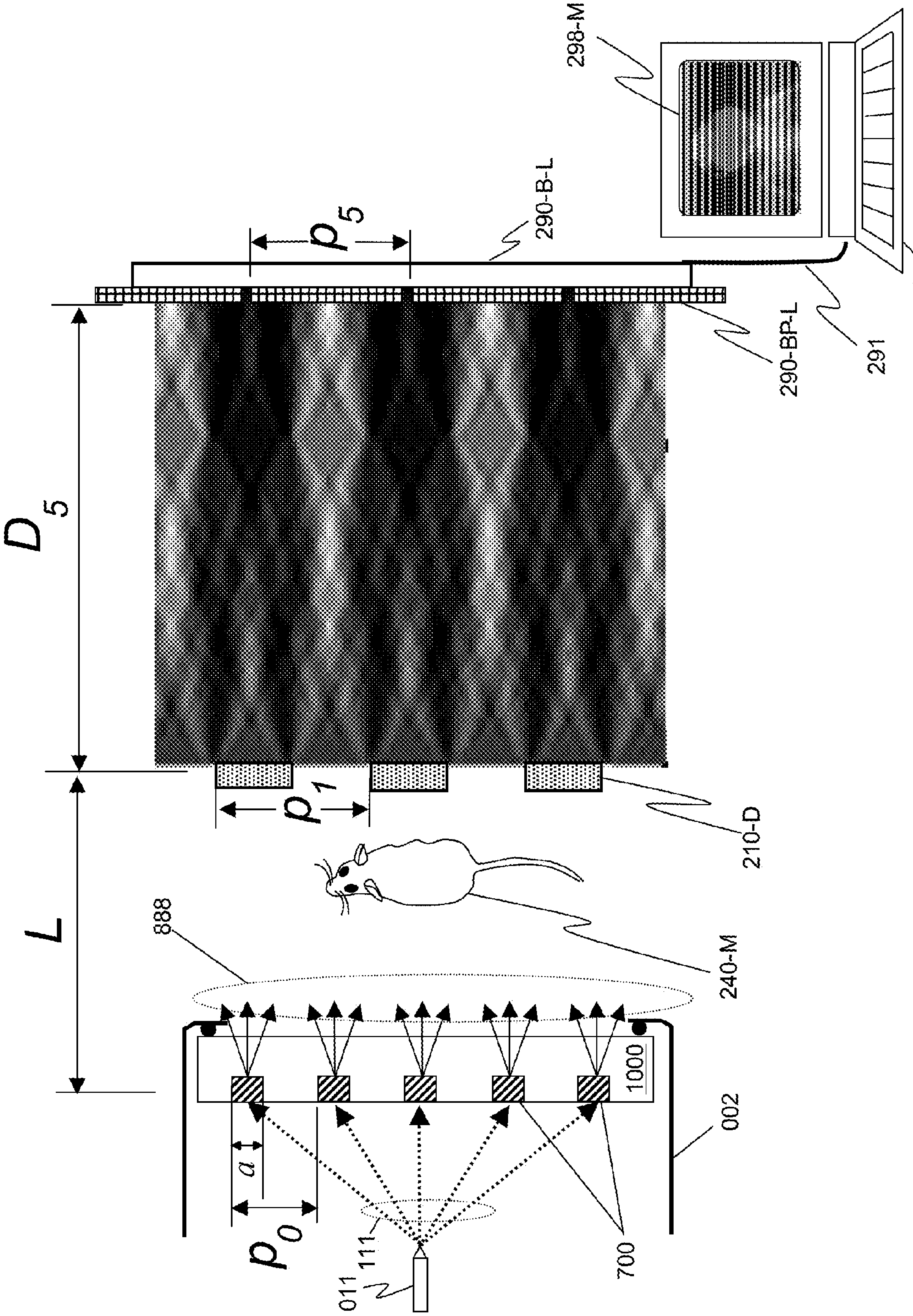
298-M
290-B-L
p_5
290-BP-L
291
295
D_5
210-D
p_1
L
888
240-M
1000
002
a
p_0
111
011
700

FIG. 45

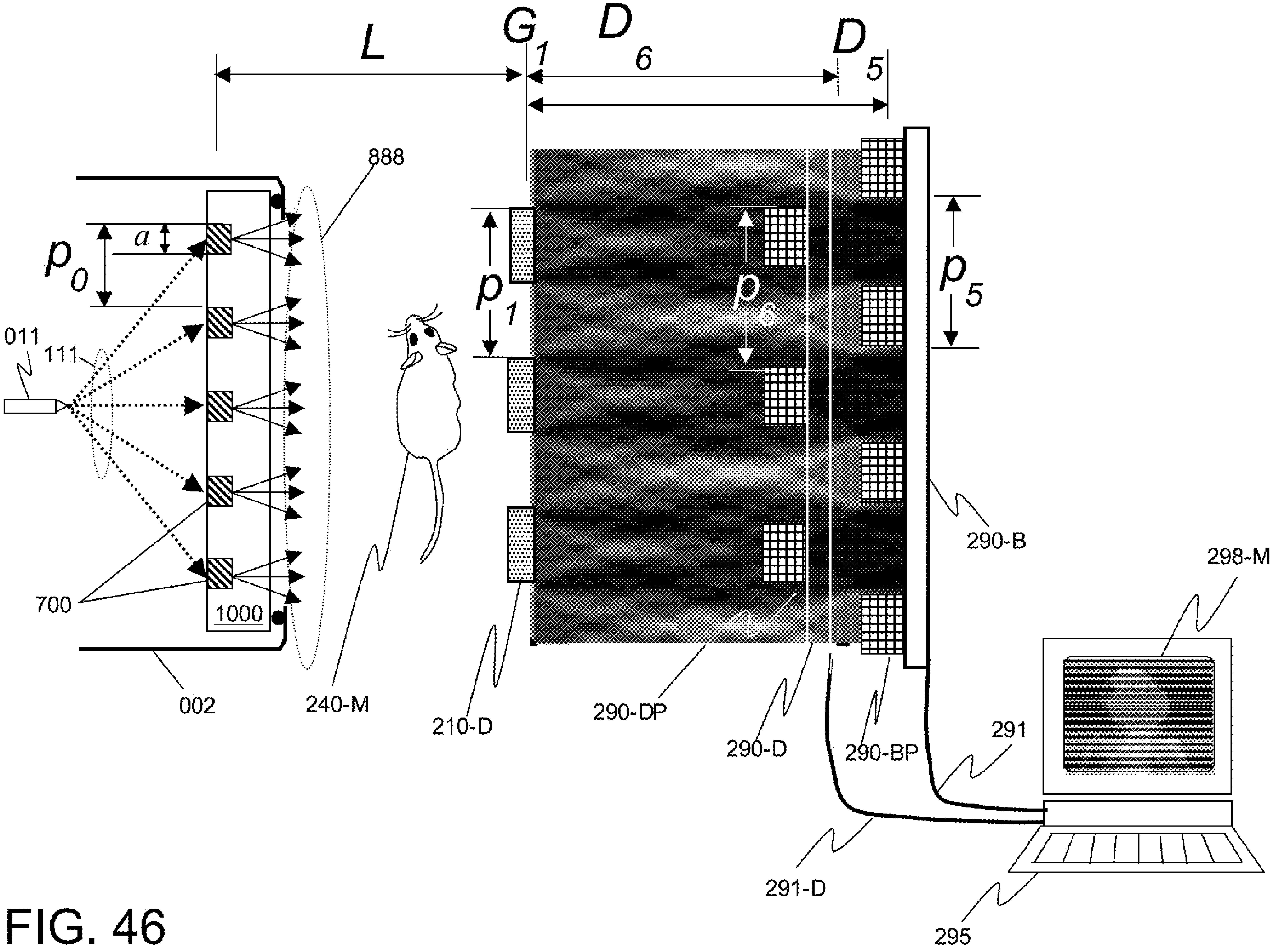

L
G_1
D_6
D_5
888
p_0
a
011
111
700
1000
002
240-M
p_1
210-D
p_6
290-DP
290-D
290-BP
p_5
290-B
298-M
291
291-D
295

FIG. 46

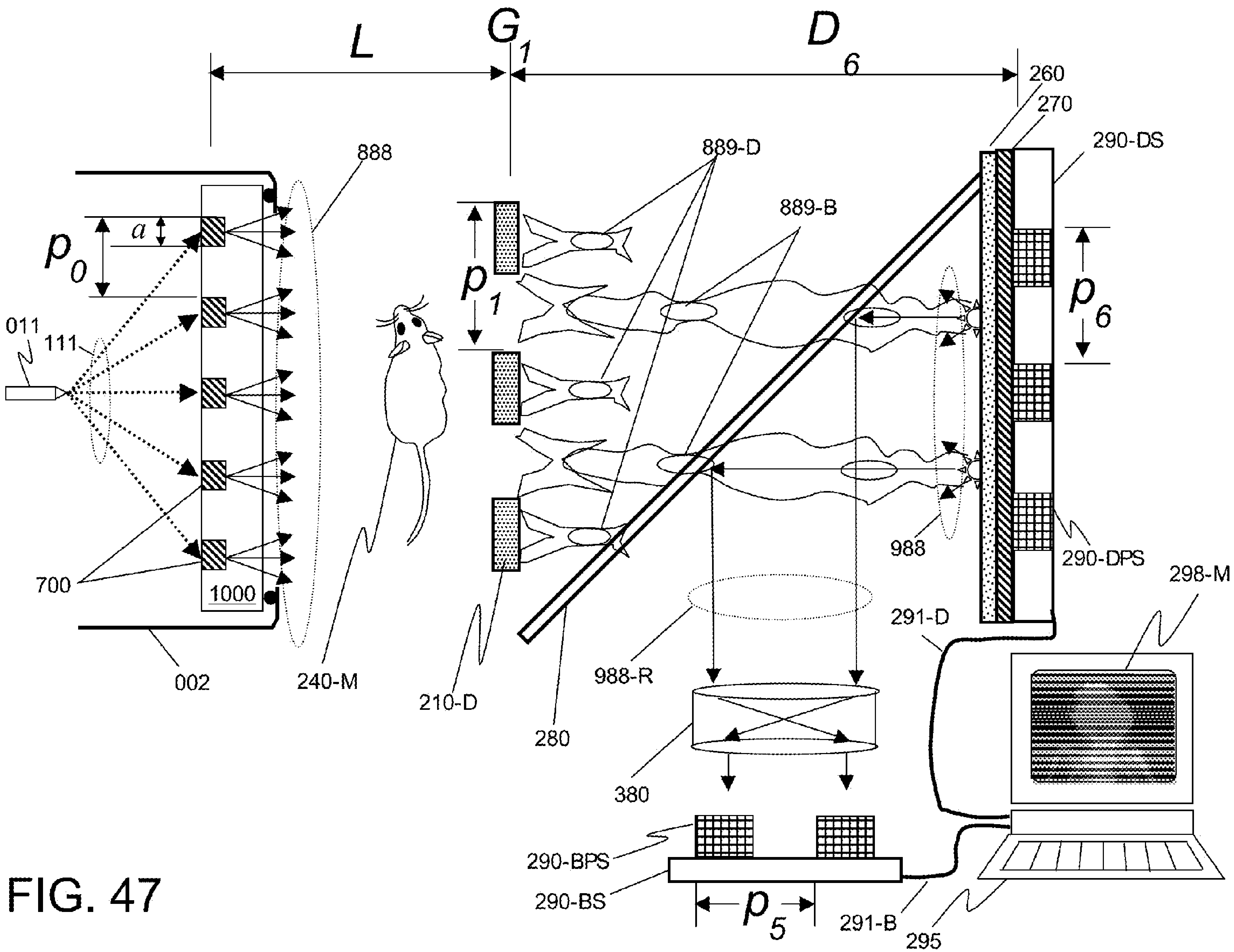
L
G1
D6
260
270
290-DS
888
889-D
889-B
a
p0
p1
p6
011
111
700
1000
002
240-M
210-D
280
988
290-DPS
298-M
291-D
988-R
380
290-BPS
290-BS
p5
291-B
295

FIG. 47

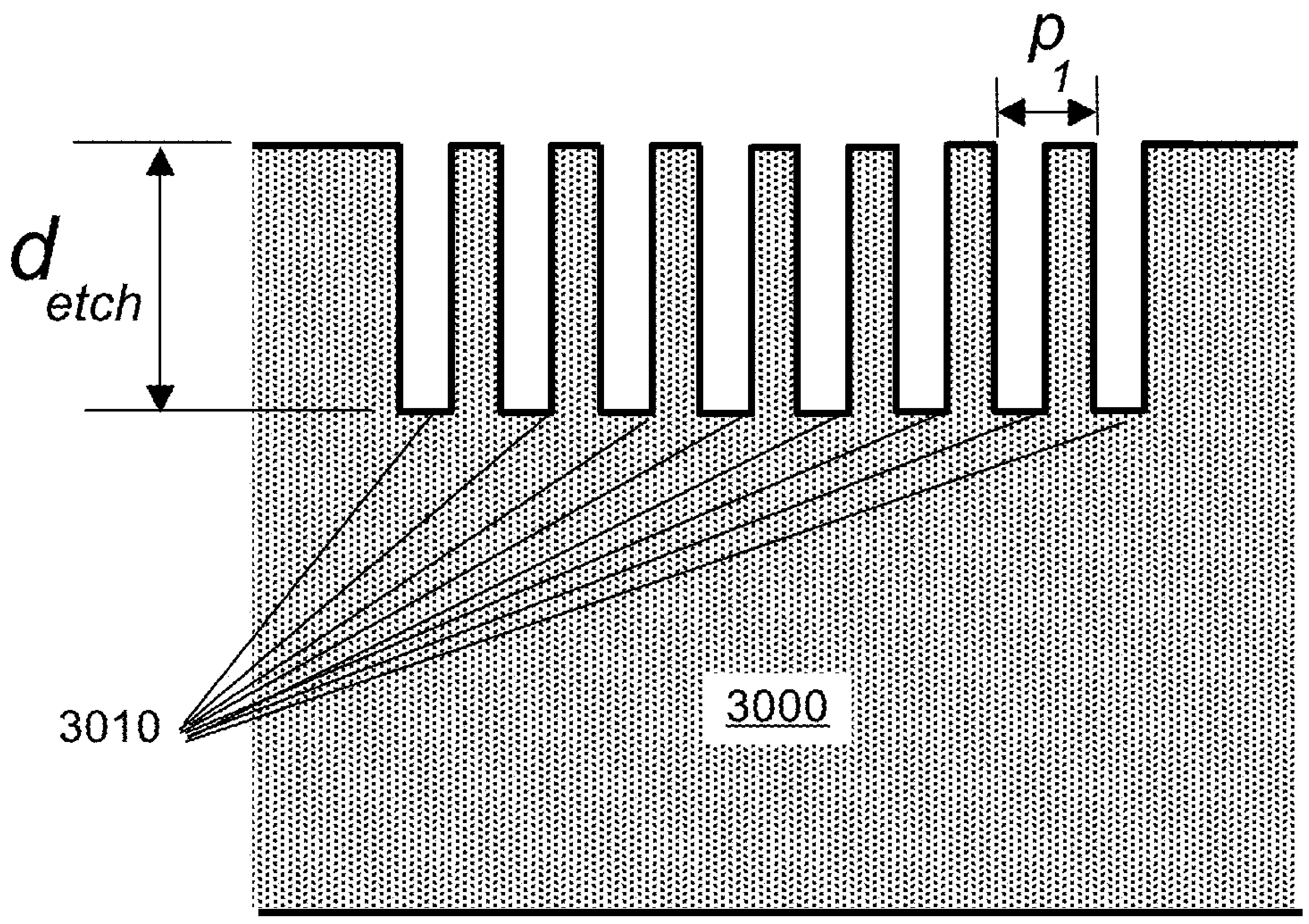

FIG. 48

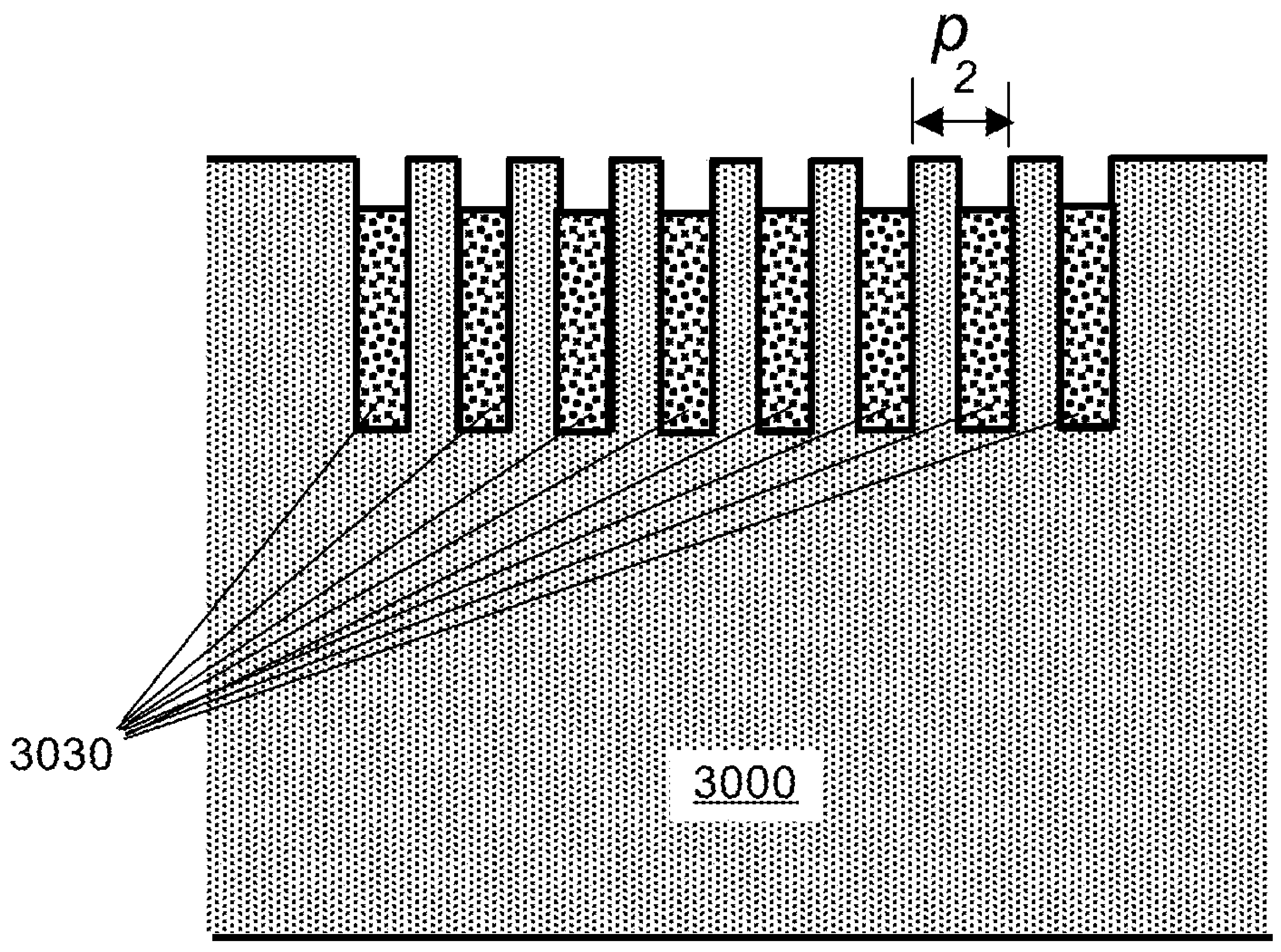

FIG. 49

X-RAY INTERFEROMETRIC IMAGING SYSTEM

Matter enclosed in heavy brackets [ ] appears in the original patent but forms no part of this reissue specification; matter printed in italics indicates the additions made by reissue; a claim printed with strikethrough indicates that the claim was canceled, disclaimed, or held invalid by a prior post-patent action or proceeding.

CROSS-REFERENCE TO RELATED APPLICATIONS

This patent application is a continuation-in-part of U.S. patent application Ser. No. 14/527,523, filed Oct. 29, 2014 and entitled "X-RAY INTERFEROMETRIC IMAGING SYSTEM", which claims the benefit of U.S. Provisional Patent Application No. 61/898,019, entitled "X-ray Phase Contrast imaging System" and filed on Oct. 31, 2013; 61/901,361, entitled "An X-ray Source Consisting of an Array of Fine Sub-Sources" and filed on Nov. 7, 2013; and 61/981,098 entitled "Two Dimensional Phase Contrast Imaging Apparatus" and filed Apr. 17, 2014, all of which are incorporated herein by reference in their entirety. The present application additionally claims the benefit of U.S. Provisional Patent Application No. 61/987,106, filed on May 1, 2014 and entitled "METHODS OF REDUCING SCATTER RADIATION USING TALBOT EFFECT"; 61/989,743, filed on May 7, 2014 and entitled "Methods of Improving Detector MTF and DQE and Reducing Scatter Background of an X-ray Imaging System Using Coherence Effect"; 61/991,889, filed May 12, 2014 and entitled "Method of Single-Shot Imaging to Obtain Absorption and Differential Phase, and/or Scattering, and/or Phase Contrast Images"; and 61/993,811, filed May 15, 2014 and entitled "Method of Talbot Effect based X-ray Imaging with High Image Contrast and Design of Apparatus Using Such", all of which are incorporated herein by reference in their entirety.

FIELD OF THE INVENTION

The embodiments of the invention disclosed herein relate to interferometric imaging systems using x-rays, and in particular, interferometric imaging systems comprising high-brightness sources of x-rays for generating phase-contrast images. The high brightness x-ray sources may use anodes or targets comprising periodic microstructures of x-ray generating materials embedded in a thermally conducting substrate of low atomic number material.

BACKGROUND OF THE INVENTION

The initial discovery of x-rays by Röntgen in 1895 [W. C. Röntgen, "Eine Neue Art von Strahlen" (Würzburg Verlag, 1896); "On a New Kind of Rays," Nature, Vol. 53, pp. 274-276 (Jan. 23, 1896)] occurred when Röntgen was experimenting with electron bombardment of targets in vacuum tubes. The contrast between the absorption from bone containing calcium (atomic number Z=20) and soft tissue containing mostly carbon (Z=6), was immediately apparent because the absorption difference between the two materials at x-ray energies between 5 and 30 keV can differ by a factor of 10 or more, as illustrated in FIG. **1**. These high energy, short wavelength photons are now routinely used for medical applications and diagnostic evaluations, as well as for security screening, industrial inspection, quality control

and failure analysis, and for scientific applications such as crystallography, tomography, x-ray fluorescence analysis and the like.

Although x-ray shadowgraphs have become a standard medical diagnostic tool, there are problems with simple absorption contrast imaging. Notably, for tests such as mammograms, variations in biological tissue may result in only a subtle x-ray absorption image contrast, making unambiguous detection of tumors or anomalous tissue difficult.

In the past decade, a new kind of x-ray imaging methodology has emerged, based on x-ray phase contrast interferometry. The method relies on the well-known Talbot interference effect, originally observed in 1837 [H. F. Talbot, "Facts relating to optical science No. IV", Philos. Mag. vol. 9, pp. 401-407, 1836] and fully explained by Lord Rayleigh in 1881 [Lord Rayleigh, "On copying diffraction gratings and some phenomena connected therewith," Philos. Mag. vol. 11, pp. 196-205 (1881)].

This effect is illustrated in FIG. **2**. For an absorbing grating G of period p, the diffraction pattern from a monochromatic beam of a wavelength λ with sufficient coherence forms a repeating interference pattern that reconstructs the original grating pattern, (known as a "self-image") at multiples of a distance known as the Talbot Distance D_T. For the case when the incident beam is a plane wave (equivalent to a source located at infinity from the grating G), D_T is given by:

$$D_T = \frac{2p^2}{\lambda} \qquad \text{[Eqn. 1]}$$

Between the grating G and the Talbot Distance, other periodic interference patterns emerge as well. The periodicity and the position of the Talbot fringes depend on the transmission properties of the grating G, including amount of phase-shift and percent of absorption, and grating line-to-space (opening) ratio, or duty factor. For example, for a periodic absorption grating, a fringe pattern that reconstructs the original grating pattern with a lateral shift by half the grating period occurs at half the Talbot Distance $D_T/2$, and a fringe pattern with a period of half of the original grating period occurs at one quarter of the Talbot Distance $D_T/4$ and at three quarters of the Talbot Distance $3D_T/4$, as illustrated in FIG. **2**. These 2-D interference patterns are sometimes called a "Talbot Carpet" because of the resemblance of these complex patterns to ornate oriental carpets. [Note: this image of an Optical Talbot Carpet in FIG. **2** is adapted from a file created by Ben Goodman and available at commons.wikimedia.org/wiki/File:Optical_Talbot_Carpet.png.]

FIGS. **3** and **4** illustrate a prior art Talbot interferometric comprising a partially coherent source **200** (shown as a microfocus source) of x-rays **288** and a beam splitting grating G_1 **210** of period p_1 that establishes a set of Talbot interference fringe patterns **289**. It should be noted that the coherence length of the x-ray source is preferably set to be comparable to or larger than the period p_1 of the beam splitting grating G_1 **210**, so that the Talbot interference fringes will have high contrast (Talbot fringes may be well defined if the fringe contrast is, for example, greater than 20%). The beam splitting grating **210** may be an amplitude (also known an absorption or transmission) grating, creating intensity fringes as illustrated in FIG. **2**, but is more typically a phase grating for efficient use of the illuminating x-rays, introducing periodic phase-shifts to the x-ray pattern that also form periodic Talbot fringes **289**. Henceforth in this application, a transmission grating will be used to describe gratings in which the x-ray transmission through the grating lines is less than 10% and a phase grating will be used to describe gratings in which the phase shift through the grating lines is a fraction (e.g. ½) or odd integer multiple of π.

The Talbot fringes **289** are detected using an x-ray detector **290**, preferably with a spatial resolution equal to or better than one third of the Talbot fringe period and having a high x-ray quantum detection efficiency. The detector **290** transforms the x-ray intensity pattern into electronic signals that are transmitted over a connector **291** to an image processing system **295**. When an object is placed in the beam path, the image processing system **295** is used to process the x-ray intensity pattern intensity information **298** to obtain absorption, phase, and scattering contrast images.

In practice, the spatial resolution of the detector **290** (such as a flat panel detector, or a charge coupled device (CCD) detector coupled with a scintillator that converts x-rays to visible light) is often on the order of tens of micrometers or larger, and the Talbot fringes **289** may be too fine to detect directly with the detector **290**. In this case, an analyzer grating G_2 **220** of period p_2 is often used to produce Moiré fringes. To record a complete set of images, the analyzer grating G_2 **220** will be moved in predetermined distances orthogonal to the grating period and relative to the detector to collect multiple interference patterns in a process called "phase-stepping", or less commonly, rotated at a small angle relative to G_1 to obtain a Moiré pattern in a single-shot image for Fourier analysis. The image(s) are then processed to reconstruct the wavefront and determine the shapes, structures, and composition of the objects that created them.

It should also be noted that, instead of physically moving the analyzer grating **220**, the position of the x-ray source may also be displaced to create a translation of the interference images that allows the collection of phase-shift information. This can be accomplished electronically by moving the position of the electron beam that bombards the x-ray generating material that serves as the source for the x-rays [see, for example, H. Miao et al., "Motionless phase stepping in X-ray phase contrast imaging with a compact source", Proceedings of the National Academy of Sciences, vol. 110(48) pp. 19268-19272, 2013] or by physically moving the x-ray source relative to a fixed position of the analyzer grating **220**.

These grating-based x-ray phase-contrast imaging (XPCI) techniques are generally referred to as "grating-based interferometry" (GBI).

As illustrated so far, the grating interferometer only produces interference fringes, and the analysis of these fringes will reveal the structure of the already known grating G_1 **210** or the wavefront of the illumination beam. However, when an object is introduced in the path of the x-ray beam, variations in the wavefront introduced by the object result in corresponding changes in the pattern of the Talbot interference fringes, generally known as Moiré fringes. Interferometric image reconstruction techniques may then be used to analyze the wavefront and reconstruct images representing the structure of the unknown object.

In FIG. **5**, the prior art Talbot interferometer of FIGS. **3** and **4** is illustrated being used as an imaging technique for a biological sample, in this case, a mouse **240**-M, placed between the source **200** and the beam splitting grating G_1 **210**. The x-rays **288** from the coherent source **200** pass through the mouse **240**-M and the beam splitting grating G_1 **210** and create a perturbed set of Talbot fringes **289**-M. The local phase shifts create angular deviations that translate into changes of locally transmitted intensity when analyzed by the analyzer grating G_2 **220** and detector **290**. Collecting multiple images from the x-ray detector **290** for situations where the analyzer grating G_2 **220** has been displaced by multiple predetermined positions allow a recording of the interference pattern **289**-M.

As before, the detector **290** transforms the x-ray intensity pattern into electronic signals that are transmitted over a connector **291** to an image processing system **295** used to produce one or more images **298**-M with absorption, differential phase, phase, and scattering contrast information. Numerical processing of the images, including images collected by the system with and without the object under investigation, can be used to infer the shapes and structure of the objects that created them, including objects such as the mouse **240**-M. The recorded intensity oscillations can be represented by a Fourier series, and with the proper image processing algorithms, differential phase shift and absorption signals can be extracted, and images corresponding to x-ray absorption, phase contrast, and scattering by the object can be synthesized. [See, for example, A. Momose et al., "Demonstration of x-ray Talbot interferometry", Jpn. J Appl. Phys. vol. 42, pp. L866-L868, 2003; A. Momose, U.S. Pat. No. 7,180,979, issued Feb. 20, 2007; and T. Weitkamp et al. "Hard X-ray phase imaging and tomography with a grating interferometer", Proc. SPIE vol 5535, pp. 137-142, 2004, and "X-ray phase imaging with a grating interferometer", Optics Express vol. 13(16), pp. 6296-6304, 2005.]

It should be noted that other configurations exist in which the object, such as a mouse **240**-M, can be placed between the beam splitting grating G_1 **210**-A and the analyzer grating G_2 **220** and detector **290**, as illustrated in FIG. **6**. Other configurations using various phase and amplitude gratings, or using detector **290** with higher resolution pixels without the analyzer grating **220**, may also be known to those skilled in the art.

Aside from imaging the anatomy of mice, clinical applications of phase-contrast x-ray imaging may be found in mammography, where the density of cancerous tissue may have a distinct phase signature from healthy tissue [see, for example, J. Keyriläinen et al., "Phase contrast X-ray imaging of breast", Acta Radiologica vol. 51 (8) pp. 866-884, 2010], or for bone diseases like osteoporosis or osteoarthritis, in which the angular orientation of the bone structures may be an early indicator of bone disease [see, for example, P. Coan et al., "In vivo x-ray phase contrast analyzer-based imaging for longitudinal osteoarthritis studies in guinea pigs", Phys. Med. Biol. vol. 55(24), pp. 7649-62, 2010].

However, for the prior art configurations described so far, x-ray power is a problem. An x-ray source with a full-width half maximum diameter S given by

$$S \leq \frac{\lambda L}{2\pi p_1} \qquad \text{[Eqn. 2]}$$

where p_1 is the period of the beam splitting grating G_1 **210** and L the distance between the source **200** and the beam splitting grating G_1 **210**, is required for the technique to produce high contrast fringes and Moiré patterns. For practical applications and system geometries, this implies a microfocus source. However, electron bombardment of the target also causes heating, and the x-ray power that can be achieved is limited by the maximum total electron power that can fall on the microspot without melting the x-ray generating material. A limited electron power means a limited x-ray power, and the low x-ray flux achievable with typical x-ray targets may lead to unacceptable long exposure times when used, for example, for mammography or other diagnostic tests involving live patients or animals. The total x-ray flux can be increased by distributing higher electron power over a larger area, but then the source becomes less coherent, degrading the image contrast.

Coherent x-rays of higher brightness and sufficient flux can be achieved by using a synchrotron or free-electron laser x-ray source, but these machines may occupy facilities that cover acres of land, and are impractical for use in clinical environments.

One innovation that has been shown to enable greater x-ray power employs an additional grating G_0 [see, for example, John F. Clauser, U.S. Pat. No. 5,812,629, issued Sep. 22, 1998]. Such a system is illustrated in FIG. **7**. In this configuration, a source grating G_0 **308** with period p_0, which is typically an x-ray transmission grating, is used in front of an x-ray source **300**. In this case, the x-ray source may be a high-power extended source with a large incident electron beam area (and not a microfocus source) that produces a higher total flux of x-rays.

The x-rays **388** pass through the grating G_0 **308** and emerge from the grating apertures as an array of individually spatially coherent (similar to a microfocus source described above) but mutually incoherent sub-sources of illumination for the beam splitting grating G_1. To ensure that each x-ray sub-source in G_0 contributes constructively to the image-formation process, the geometry of the setup should satisfy the condition:

$$p_0 = p_2 \frac{L}{D} \qquad \text{[Eqn. 3]}$$

When the condition is met, the x-rays from the many apertures of G_0 produce the same (overlapping) Talbot interference pattern, and because the various mutually incoherent sources do not interfere with each other, these Talbot patterns will add as intensities. The effect at the detector **290** is therefore to simply increasing the signal (along with it the signal-to-noise ratio) over what a single coherent source can provide.

This configuration is called the Talbot-Lau interferometer [see Franz Pfeiffer et al., "Phase retrieval and differential phase-contrast imaging with low-brilliance X-ray sources", Nature Physics vol. 2, pp. 258-261, 2006; and also Described in U.S. Pat. No. 7,889,838 by Christian David, Franz Pfeiffer and Timm Weitkamp, issued Feb. 15, 2011].

FIGS. **8**A-**8**C illustrate x-ray images of a live mouse collected using a Talbot-Lau interferometer, as reported by Martin Bech [M. Bech et al., "In-vivo dark-field and phase-contrast x-ray imaging", Scientific Reports 3, Article number: 3209, 2013, FIG. **1**]. The x-ray energy used was 31 keV, and the gratings were fabricated by lithographically etching structures in silicon (Z=14). Absorption gratings G_0 for the source and G_2 for the analyzer were created by additionally coating the patterned silicon with gold (Z=79).

All of the images of FIGS. **8**A-**8**C were reported as reconstructed from the same set of 5 interferometric images, each collected over an exposure time of 10 seconds. The raw images were Fourier processed and ramp corrected to obtain the three image modalities. FIG. **8**A illustrates an intensity image based on x-ray attenuation, showing the absorption contrast between the bones and soft tissue. FIG. **8**B illustrates a phase-contrast image, which clearly identifies soft tissue structures such as the trachea (illustrated with an arrow). FIG. **8**C illustrates an additional dark-field contrast image due to x-ray scattering from fine features with linear dimensions less than the spatial resolution of the imaging system, which strongly highlights the fur and lungs.

Unfortunately, the current art of Talbot-Lau GBIs have many constraints for most practical applications such as clinical imaging, including a requirement that both the source grating G_0 and the analyzer grating G_2 have fine pitches and apertures with large aspect ratios.

The requirement for the source grating G_0 is to create fine individual well-separated x-ray sub-sources to minimize the reduction in image contrast due to unwanted transmission of x-rays through the aperture defining structures. However, for a 1:1 line-to-space ratio grating, simple x-ray shadowing dictates that the x-ray transmission through the grating is limited to less than 50%, and is reduced further when the angular shadowing (limiting the angular range of the x-rays from the source to reach the object) is included. Furthermore, the optimal line-to-space ratio for G_0 that reduces the radiation dose to the object (which is important to preclinical and clinical imaging applications) is closer to 3:1 rather than 1:1. In this case, about 75% of the x-rays from the source are blocked due to area shadowing alone, and when gratings with large aspect ratios are used, greater losses occur due to angular shadowing.

The requirement for the analyzer grating G_2 is to be able to sample the Talbot interference fringes with sufficient resolution without losing contrast. As a result, both the G_0 and G_2 gratings must have small apertures and be of thickness sufficient to minimize unwanted x-ray transmission, which limits the efficient use of the x-rays from the source. Furthermore, the loss from the analyzer grating G_2 further results in a significantly higher dose (relative to the same system without a G_2 grating) for the object under investigation to produce an image with good characteristics due to multiple exposures for phase-stepping and absorption of x-rays resulting in lower signal-to-noise. When the object under investigation is a live animal or human, higher doses of ionizing radiation are undesirable and generally discouraged.

If the aperture dimensions of the grating G_0 are larger, angular collimation can be reduced (although not the area shadowing) so that x-ray transmission is not reduced as severely, but this reduces the spatial coherence length of the x-ray beam downstream from the apertures, and leads a reduction in image contrast. Smaller apertures can increase the possible image contrast and resolution by improving spatial coherence, but decreases the overall number of x-rays in the system, thus requiring longer exposure times. Moreover, with smaller apertures, these fine gratings become more difficult to manufacture.

The problem is exacerbated when attempting to use a Talbot-Lau interferometer for higher energy x-rays, which are often desired to obtain sufficient transmission through an object and to reduce radiation dose. In general, as was illustrated in FIG. **1**, the absorption of x-rays for biological tissue is far lower for x-rays with energy greater than 5 keV, and the use of higher energy x-rays will reduce the absorbed dose of potentially harmful ionizing radiation by orders of magnitude. However, 5 keV photons have a wavelength of 0.248 nm, and 50 keV have a wavelength 10 times smaller (0.0248 nm). Furthermore, building absorbing gratings such as G_0 and G_2 for these higher-energy, shorter-wavelength x-rays can present difficulties, as the thickness of the gratings must increase exponentially to maintain the same absorption factor for higher energy x-rays (the x-ray attenuation length is approximately proportional to E_{kev}^3).

The preceding problems of Talbot-Lau GBIs using linear gratings, which can be used for collecting interference data in one dimension only, become more severe if one wishes to generate phase-contrast images in two orthogonal directions. This is often required to make the image reconstruction robust and images more understandable, and because features parallel to the grating lines in the 1-D case are typically less accurately measured. One simple approach is to perform XPCI in two orthogonal directions and then subsequently register the two datasets properly. In addition to challenges associated with the imaging and registration processes, this approach may not be practical, especially when used with living subjects who may move or simply become impatient, and who will incur increased dosage (doubled) if the phase stepping must be performed in two directions. Simultaneous two-dimensional XPCI would be desirable, especially if data collection in a single exposure (shot) and at high x-ray energies is possible to reduce exposure times and the absorbed dosage.

There is therefore a need for an x-ray interferometric imaging system that offers the resolution and detection capabilities of the Talbot-Lau interferometer, but employing a brighter compact source of x-rays and, ideally, a brighter source of higher energy x-rays, especially one that could provide simultaneous two-dimensional phase-contrast imaging.

BRIEF SUMMARY OF THE INVENTION

We disclose here an x-ray interferometric imaging system in which the x-ray source comprises a target having a plurality of micro structured x-ray generating materials arranged within a periodic array pattern to form periodic sub-sources of x-rays. The system additionally comprises a beam-splitting grating G_1 that creates a Talbot interference pattern, and an x-ray detector to convert two-dimensional x-ray intensities into electronic signals.

If the spatial resolution of the detector is equal to or better than one third of the Talbot fringe period, the detector may record the fringes directly. The system may also comprise a second analyzer grating G_2 that may be placed in front of the detector to form additional interference fringes, and a means to translate the analyzer grating G_2 relative to the detector to create Moiré fringes at the detector. Additionally, the system may comprise a means of translating the phase grating G_1 relative to the analyzer grating G_2.

The x-ray source target comprises a plurality of microstructures of x-ray generating materials (such as molybdenum or tungsten) in close thermal contact with a thermally conducting substrate of a low atomic number material, such as diamond or beryllium. The x-ray generating microstructures may be arranged in a periodic pattern, with each periodic element of the pattern corresponding to a single discrete microstructure or alternatively, with each periodic element of the pattern comprising multiple discrete microstructures. One or more sources of electrons bombard the plurality of x-ray generating materials, which are generally arranged within a periodic array, so that the x-ray generated from each periodic array element serves as an individually coherent sub-source of x-rays of illumination for the beam splitting grating G_1. In some embodiments, the microstructures have lateral dimensions measured on the order of microns, and with a thickness on the order of one half of the electron penetration depth within the substrate material. In some embodiments, the microstructures are formed in a regular two-dimensional array.

The beam splitting grating G_1 may be a phase grating or an absorption grating. The analyzer grating G_2 is generally a transmission grating. Both gratings G_1 and G_2 may be fabricated as lithographically produced microstructures in silicon, and may comprise 1-D structures, 2-D structures, or combinations thereof.

A particular advantage of the invention is that high x-ray brightness and large x-ray power may be achieved by using an x-ray target in which the microstructures of a high Z material are in close thermal contact with, or embedded in, a substrate of low Z material and high thermal conductivity, such as beryllium or diamond. The ability of the substrate to draw heat away from the x-ray generating material allows higher electron density and power to be used, generating greater x-ray brightness and power from each of the sub-sources. This results in the creation of individual, well-separated spatially coherent x-ray sub-sources from the high Z material, while the use of a substrate with low Z and low mass density minimizes the production of x-rays from the substrate that can lead to a reduction in image contrast.

BRIEF DESCRIPTION OF THE DRAWINGS

FIG. **1** illustrates a plot of the x-ray absorption of carbon and calcium as a function of x-ray energy.

FIG. **2** illustrates a prior art Talbot interference pattern produced by a transmission grating.

FIG. **3** illustrates a prior art x-ray grating interference system using a microfocus source.

FIG. **4** illustrates a cross section view of the prior art x-ray grating interference system of FIG. **3**.

FIG. **5** illustrates the prior art x-ray grating interference system of FIG. **3** used to form an x-ray contrast image of a mouse.

FIG. **6** illustrates a variation of the prior art x-ray grating interference system of FIG. **3** used to form an x-ray contrast image of a mouse.

FIG. **7** illustrates a prior art Talbot-Lau interferometer being used to form an x-ray contrast image of a mouse.

FIG. **8**A illustrates a published x-ray absorption image of a mouse gathered using a prior art Talbot-Lau interference system.

FIG. **8**B illustrates a published x-ray phase-contrast image of a mouse gathered using a prior art Talbot-Lau interference system.

FIG. **8**C illustrates a published x-ray dark field scattering image of a mouse gathered using a prior art Talbot-Lau interference system.

FIG. **9** illustrates a schematic cross-section view of an embodiment of an x-ray interferometric imaging system according to the invention.

FIG. **10** illustrates a schematic cross-section view of an embodiment of the invention.

FIG. **11** illustrates a perspective view of the embodiment of the invention shown in FIG. **10**, in which the x-ray target comprises two dimensional periodic array of x-ray generating microstructures.

FIG. **12** illustrates a detailed schematic cross-section view of the embodiment of the invention shown in FIGS. **10** and **11**.

FIG. **13** illustrates a perspective view of an embodiment of the invention in which the x-ray target comprises of x-ray generating microstructures in the form of parallel lines.

FIG. **14** illustrates a perspective view of an embodiment of the invention in which the object (a mouse) is placed between the gratings G_1 and G_2.

FIG. **15** illustrates a detailed schematic cross-section view of an embodiment of the invention in which a high-resolution detector is used without an analyzer grating.

FIG. **16** illustrates a perspective view of an embodiment of the invention in which the object (a mouse) is placed between the grating G_1 and the detector, and the grating G_1 comprises a two-dimensional phase structure.

FIG. **17** illustrates a "mesh" 2-D pattern for a beam splitting grating used in some embodiments of the invention.

FIG. **18** illustrates a "checkerboard" 2-D pattern for a beam splitting grating used in some embodiments of the invention.

FIG. **19** illustrates a perspective view of an embodiment of the invention in which the object (a mouse) is placed between the source and the grating G_1, and the grating G_1 comprises a two-dimensional phase structure.

FIG. **20** illustrates a schematic cross-section view of an embodiment of the invention in which the target is mounted within the vacuum chamber.

FIG. **21** illustrates a detailed schematic cross-section view of the embodiment of the invention shown in FIG. **20**.

FIG. **22** illustrates a schematic cross-section view of an embodiment of the invention in which the target is mounted within the vacuum chamber and x-rays are generated using linear accumulation.

FIG. **23** illustrates a detailed schematic cross-section view of the embodiment of the invention shown in FIG. **22**.

FIG. **24** illustrates a schematic cross-section view of an embodiment of the invention in which two electron beams bombard the target from both sides.

FIG. **25** illustrates a detailed schematic cross-section view of the embodiment of the invention shown in FIG. **24**.

FIG. **26** illustrates a perspective view of a target comprising a grid of embedded rectangular target microstructures on a larger substrate that may be used in some embodiments of the invention.

FIG. **27** illustrates a perspective view of a variation of a target comprising a grid of embedded rectangular target microstructures on a larger substrate for use with focused electron beam that may be used in some embodiments of the invention.

FIG. **28**A illustrates a perspective view of a target comprising a grid of embedded rectangular target microstructures as used in some embodiments of the invention.

FIG. **28**B illustrates a top view of the target of FIG. **28**A.

FIG. **28**C illustrates a side/cross-section view of the target of FIGS. **28**A and **28**B.

FIG. **29**A illustrates a perspective view of a target comprising a set of embedded rectangular target microstructures forming a periodic linear pattern as used in some embodiments of the invention.

FIG. **29**B illustrates a top view of the target of FIG. **29**A.

FIG. **29**C illustrates a side/cross-section view of the target of FIGS. **29**A and **29**B.

FIG. **30** illustrates variations in target structure for a target as shown in FIGS. **28**A-C that may arise from processing variations.

FIG. **31** illustrates variations in target structure for a target as shown in FIGS. **29**A-C that may arise from processing variations.

FIG. **32** illustrates a cross-section view of a portion of the target of FIGS. **28**A-C and/or FIGS. **29**A-C, showing thermal transfer to a thermally conducting substrate under electron beam exposure according to the invention.

FIG. **33** illustrates a cross-section view of a variation of the target of FIGS. **28**A-C, FIGS. **29**A-C and/or FIG. **32** comprising a substrate with a thermal cooling channel according to the invention.

FIG. **34** illustrates a cross-section view of another variation of the target of FIGS. **28**A-C and/or FIGS. **29**A-C comprising an adhesion layer according to the invention.

FIG. **35** illustrates a cross-section view of another variation of the target of FIGS. **28**A-C and/or FIGS. **29**A-C comprising an electrically conducting overcoat according to the invention.

FIG. **36** illustrates a cross-section view of another variation of the target of FIGS. **28**A-C and/or FIGS. **29**A-C comprising buried x-ray material according to the invention.

FIG. **37** illustrates a cross-section view of another variation of the target of FIGS. **28**A-C and/or FIGS. **29**A-C comprising buried x-ray material and a thick thermally and electrically conducting overcoat according to the invention.

FIG. **38** illustrates a cross-section view of another variation of the target of FIGS. **28**A-C and/or FIGS. **29**A-C comprising an additional blocking structures on the back surface of the substrate, to block the transmission of x-rays produced by the substrate.

FIG. **39** illustrates a plot of the x-ray absorption of gold and silicon as a function of x-ray energy.

FIG. **40** illustrates a detailed schematic cross-section view for an embodiment of the invention in which an additional antiscattering grating is used.

FIG. **41** illustrates a cross-section of the placement of antiscattering gratings within a Talbot interference pattern.

FIG. **42** illustrates a schematic cross-section of an antiscattering grating.

FIG. **43** illustrates a detailed schematic cross-section view for an embodiment of the invention in which an additional antiscattering grating is used along with an analyzer grating at the detector.

FIG. **44** illustrates a schematic cross-section view for an embodiment of the invention in which the detector elements are aligned with the high intensity portions of the Talbot interference pattern.

FIG. **45** illustrates a schematic cross-section view for an embodiment of the invention in which a beamsplitting grating is placed upstream of a detector such that the detector elements are aligned with the high intensity (antinodes) of the Talbot interference pattern.

FIG. **46** illustrates a schematic cross-section view for an embodiment of the invention comprising both a bright field and dark field detector.

FIG. **47** illustrates a schematic cross-section view for an embodiment of the invention comprising both a bright field and dark field detector, in which a scintillator is used to convert x-rays to visible/UV photons.

FIG. **48** illustrates a possible structure of an x-ray phase grating according to some embodiments of the invention.

FIG. **49** illustrates a possible structure of an x-ray absorption grating according to some embodiments of the invention.

Note: The illustrations in the Drawings disclosed in this application are typically not shown to scale, and are meant to illustrate the principle of the invention and its function only, and not specific relationships between the microstructures in the target and the various grating periods p_1, p_2, p_3, p_4, p_5, and p_6. Please refer to the descriptions in the text of the Specification for specific details of the dimensions of these objects.

DETAILED DESCRIPTIONS OF EMBODIMENTS OF THE INVENTION

Descriptions of Various Embodiments of the Invention

One embodiment of the invention disclosed herein is an x-ray phase-contrast imaging (XPCI) system as illustrated in FIG. **9**. The system bears some similarity to the prior art Talbot-Lau interferometer, in that it comprises a beam splitting grating G_1 **210** of period p_1 that establishes a Talbot interference pattern, and an x-ray detector **290** typically comprising an array of sensors to convert two-dimensional x-ray intensities into electronic signals.

The beam splitting grating G_1 **210** may be a phase grating or a transmission grating, and may comprise 1-D periodic patterns (linear gratings), or may comprise more complex 2-D structures such as a grid that is periodic in two orthogonal directions.

The system may also comprise an analyzer grating G_2 **220** of period p_2 that may be placed in front of the detector to form additional interference fringes, such as Moiré fringes. The system may additionally comprise a means **225** to translate the analyzer grating G_2 **220** relative to the detector, and a connector **291** to transmit electronic signals corresponding to the detected x-ray intensity to an image processing system **295** for processing.

However, instead of using an extended x-ray source and an additional grating G_0 to create a plurality of x-ray source spots, as was done in the Talbot-Lau system, the embodiments of the present invention use an x-ray source comprising a plurality of x-ray generating sub-sources **108** arranged in a periodic array that generate x-rays **188** from electron beam bombardment, such that each sub-source is individually coherent, but together function as a set of mutually incoherent or partially coherent sub-sources of illumination for the beam splitting grating G_1. As with the combination of the extended x-ray source and the source grating of the Talbot-Lau interferometer, these sub-sources **108** form the Talbot interference fringe patterns that are created by the beam splitting grating G_1 **210** and perturbed by an object **240**-M, and may be recorded by detector **290**. If the spatial resolution of the detector **290** has a spatial resolution equal to or better than one third of the Talbot fringe period, the detector may record the fringes directly. If a lower resolution detector is used, an analyzer grating G_2 **220** may also be used to create Moiré fringes, as was described for the Talbot-Lau interferometer.

The plurality of discrete x-ray sub-sources can be considerably brighter than the x-ray source of the Talbot-Lau system. Because the source comprises sub-sources that are self-coherent but may be mutually incoherent, there is no need for an attenuating transmission grating G_0 to create an array of sub-sources from an extended x-ray source.

A system according to the invention comprising multiple sub-sources in a structured target may be designated a Talbot-ST interferometer.

FIGS. **10**, **11** and **12** show a more detailed illustration of one embodiment of the invention, in which the array of sub-sources are formed using microstructures of x-ray generating material embedded in a thermally conducting substrate. In this embodiment, an x-ray source **008** illuminates an object **240**-M and a beam-splitting grating G_1 **210**, and the interference pattern they form is detected by a detector **290**.

For the x-ray source **008**, a high voltage power supply **010** provides electrons through a lead **021** to an electron emitter **011** in a vacuum chamber **002** held to a shielding housing **005** by supports **003**. The electron emitter **011** emits electrons **111** towards a target **100**. The target **100** comprises a substrate **1000** and a region that comprises a periodic array of discrete microstructures **700** comprising x-ray generating material (typically a high Z metallic material such as copper, molybdenum or tungsten) positioned on or embedded or buried in the substrate (typically a low Z material such as beryllium, diamond, silicon carbide). The discrete microstructures **700** may be any number of sizes or shapes, but are generally designed to be periodic arrays of right rectangular prisms with lateral dimensions on the order of microns in size in at least one dimension, such that the emission from each microstructure acts as a sub-source of x-rays with a spatial coherence length that is comparable to or larger than the grating period p_1 at the beam splitting grating G_1 **210**. Additionally, the microstructures are preferably of a thickness (as typically measured orthogonal to the target surface) that is on the order of one half of the electron penetration depth within the substrate material.

The period p_0 of the microstructures **700** that form the x-ray sub-sources is related to the other geometric parameters in the system by:

$$p_0 = p_2\frac{L}{D} \qquad \text{[Eqn. 4]}$$

where L is the distance from the x-ray sub-sources **700** to the grating G_1 **210**, and D is the distance from the grating G_1 to the detector/analyzer grating G_2 **220** with period p_2. In some embodiments, D will be set to be one of the fractional Talbot distances with interference fringes of high contrast (visibility), defined by:

$$\text{Contrast} = \frac{I_{max} - I_{min}}{I_{max} + I_{min}} \qquad \text{[Eqn. 5]}$$

where I_{max} and I_{min} is the intensity peak and valley of the Talbot interference fringes without an object in the beam path, respectively.

For plane wave illumination (i.e. equivalent to the x-ray source being located at infinity) of a beam-splitting grating with a π phase-shift, the distance D is preferably given by:

$$D = D_N = N\frac{p_1^2}{8\lambda} = \frac{N}{16}D_T \qquad \text{[Eqn. 6]}$$

where D_N is the fractional Talbot distance for a plane wave illumination, λ is the mean x-ray wavelength, and N is referred to as a Talbot fractional order. The preferred value of D is dependent on the attenuating or phase shifting properties of the beam-splitting grating G_1, the line-space ratio of the beam-splitting grating G_1, and the source-to-grating distance L. For a π phase-shifting grating with a line-to-space ratio of 1:1, an odd integer fractional Talbot order N (N=1, 3, 5 . . .) is preferred for determining the distance D. For an x-ray source located at a finite distance (e.g. L not infinity), D is increased to:

$$D = \frac{L \times D_N}{L - D_N} \qquad \text{[Eqn. 7]}$$

The Talbot fringe period p_f for a given fractional order is given by:

$$p_f = Kp_1\frac{L+D}{L} \quad \text{[Eqn. 8]}$$

where K is a parameter dependent on the attenuating or phase shifting properties of the beam-splitting grating G_1. K equals ½ when the beam-splitting grating is a λ phase-shift grating, and equals 1 when the beam splitting grating is a π/2 phase shift grating.

Likewise, the Talbot fringe contrast is improved if a smaller x-ray sub-source size (i.e. more spatially coherent x-rays) is used, and in which the pitch p_1 used for the beam splitting grating G_1 is related to the size of the sub-source a and the distance L between them, satisfying the following requirement:

$$p_1 < \frac{\lambda L}{a} \quad \text{[Eqn. 9]}$$

where λ is a predetermined x-ray wavelength that will generally correspond to the wavelength of the monochromatic x-rays produced by the corresponding sub-source, or the mean x-ray wavelength for an x-ray sub-source with a broader spectrum.

In the vacuum chamber **002**, electrons **111** bombard the target, and generate heat and x-rays **888** in the microstructures **700**. The material in the substrate **1000** is selected such that it has relatively low energy deposition rate for electrons in comparison to the microstructures of the x-ray generating material, typically by selecting a low Z material for the substrate, and therefore will not generate a significant amount of heat and x-rays. The substrate **1000** material may also be chosen to have a high thermal conductivity, typically larger than 100 W/(m ° C.). The microstructures of the x-ray generating material are also typically embedded within the substrate, i.e. if the microstructures are shaped as rectangular prisms, it is preferred that at least five of the six sides are in close thermal contact with the substrate **1000**, so that heat generated in the microstructures **700** is effectively conducted away into the substrate **1000**. However, targets used in other embodiments may have fewer direct contact surfaces. In general, when the term "embedded" is used in this disclosure, at least half of the surface area of the microstructure will be in close thermal contact with the substrate.

The microstructures are typically connected electrically with a lead **022** to the positive terminal of the high voltage source **010** to allow the target to serve as an anode in the electrical system. Alternatively, the target may be grounded while the cathode (electron emitter) is of negative charge, or the target may be connected to a positive terminal while the cathode is grounded, so long as the anode is of relative higher voltage than the cathode. Additionally, in some embodiments, electron optics such as electrostatic lenses or magnetic coils may be placed inside or outside of the vacuum chamber **002** around or near the path of electrons **111** to further direct and focus the electron beam.

The target **100** as illustrated may additionally serve as a window in the vacuum chamber **002** so that the x-ray generating material is facing the interior of the vacuum chamber and the electron source, but x-rays **888** are also propagate through the back side of the target **100** towards the beam-splitting grating G_1 **210**. In other embodiments, a separate window is used, and additional x-ray filters may also be used

Once generated by the source **008**, the x-rays **888** may pass through an optional shutter **230**, an x-ray spectral filter to obtain a desired spectral bandwidth with a desired wavelength, and an object **240**-M to be investigated. The x-rays then diffract off the beam splitting grating G_1 **210**, which may additionally be mounted on a substrate **211**, and then fall on the analyzer grating G_2 **220**, which may also be mounted on a substrate **221**. The final interference pattern will be detected by an array detector **290** that provides electrical signals corresponding to the x-ray intensity through a connector **291** to an image processing system **295** for analysis.

In addition to the x-ray source and interference detection system, means to move the object **240**-M and the various gratings relative to each other, to the detector, and to the source may be used. In FIG. **10**, the image processing system **295** may also be connected through a network **231** to a means **245** of controlling a stage **244** that sets the position and angle of the object **240**-M, to a means **215** of controlling a mount **214** that sets the position and angle of the beam splitting grating G_1 **210**, and to a means **225** of controlling a mount **224** that sets the position and angle of the analyzer grating G_2 **220**, as well as a possible connection to the shutter **230** or to a switch **013** for the high voltage supply **010** to allow the x-rays to be moved and modulated (such as being turned on and off). Software run by processors in the image processing system **295** may control the motion of the gratings G_1 **210**, G_2 **220**, the object **240**-M, and also the x-ray exposure to allow the collection of the multiple images needed to obtain detailed amplitude, differential phase, phase-contrast, and scattering contrast images of the object **240**-M.

Additional embodiments may also include controls that allow the electron beam to be moved or modulated. For example, embodiments may be designed that additionally comprise a means of translating the x-ray source anode relative to the analyzer grating G_2. Additional embodiments that also allow the position and angle of the x-ray detector **290** to be adjusted may also be designed.

FIG. **13** illustrates an embodiment of the invention in which the target **100** comprises a substrate **1000** and a plurality of microstructured line sources **701**. These microstructured line sub-sources **701** will typically be a few microns wide in one direction (corresponding to the sub-source size parameter a, generally in the dimension orthogonal to the direction of the lines of the gratings G_1 **210** and G_2 **220**, which corresponds to the y-direction in FIG. **13**) but much longer (e.g. up to 1000 microns or several millimeters) in the direction parallel to the lines (which corresponds to the x-direction in FIG. **13**). The pitch of the microstructures **701** as sub-sources as shown in FIG. **13** is p_0, and is related to the pitch of the analyzer/detector by Equation 4.

FIG. **14** illustrates an embodiment of the invention in which the object **240**-M to be examined is placed between the gratings G_1 **210** and the detector **290**. The microstructures **700** of x-ray generating material on the target as illustrated in FIG. **14** comprise sub-sources arranged in a 2-D periodic array in two orthogonal directions, but may be any periodic array that satisfies the coherence illumination condition of the beam-splitting grating G_1 **210**, including a grid, a mesh, a checkerboard, or other periodic structures.

If the gratings comprise one-dimensional structures, the microstructures **700** in the source target **100** need only be periodic in the same direction as the 1-D arrays of G_1 **210** and G_2 **220** (i.e. the lines of microstructures **701** are ideally parallel to the lines of the gratings) but can have arbitrary or non-periodic structure in the perpendicular direction.

FIG. **15** additionally illustrates an embodiment of the invention in which the there is no analyzer grating G_2 **220**, but instead the detector **299** has a high resolution array G_D with a pixel resolution equal to or better than one third (⅓) of the Talbot fringe period in the direction orthogonal to the grating lines. With this resolution, a single exposure image may be processed to obtain absorption, phase, and scattering contrast images simultaneously. This can be advantageous in that the intensity loss of 50% or more that typically occurs for x-rays passing through G_2 **220** is avoided, and the signal reaching the detector and therefore the signal-to-noise ratio is substantially higher.

In order to collect the multiple images for the calculation of detailed amplitude, differential phase, phase-contrast, and scattering contrast images for an object **240**-M, the embodiment of FIG. **15** may additionally comprise a means **255** for translating the detector **290**, not only in the two lateral directions parallel to the plane of the grating G_1, but also in direction defined along the path of x-ray propagation, to ensure that the detector **299** is placed at the correct multiple of the Talbot distance T_D.

FIG. **16** illustrates an embodiment of the invention in which the beam splitting grating G_1 **210**-**2**D comprises a two-dimensional periodic array, which may be either a transmission or a phase grating. When using a 2-D beam-splitting grating of this type, the patterns may be arranged in any one of a number of periodic patterns, including a mesh, such as the pattern illustrated in FIG. **17**, or a checkerboard pattern, as illustrated in FIG. **18**, In these illustrations, clear regions are non-phase shifted regions, while patterned regions represent regions with a relative phase shift. Different, or even opposite relative phase shifts, may also be used in some embodiments, i.e., the clear regions can be phased shifted while the patterned regions are not.

For use with an incident x-ray beam with a spectral bandwidth of less than ±15% around the mean energy, a beam splitting grating with a phase shift of π radians and a line-to-space ratio of 1:1 may be preferred. For use with an incident beam with a spectral bandwidth greater than ±15%, a relative phase shift of $\pi/2$ radians may be preferred.

The beam splitting gratings in some embodiments may have a profile comprising 1-D stripes, such as a Ronchi profile or structures having a rectangular profile. The relative phase shift between the dark and clear stripes is preferably selected to be π or $\pi/2$ radians, but may also be any integer multiple or fraction of π. Alternatively, the dark stripes may have low x-ray transmission so that the beam splitting grating is an absorption grating.

FIG. **16** illustrates the use of a 2-D beam splitting grating G_1 **210**-**2**D in conjunction with a high-resolution detector **299**, as was also shown in FIG. **15**. To simultaneously obtain a differential phase contrast, phase contrast, absorption, scattering contrast images in two orthogonal directions, the geometric parameters, including the x-ray sub-source size a, the period p_1 of the grating G_1**210**-**2**D and the distance L, need to satisfy the coherence illumination condition of the grating G_1 in both directions. As before, the detector **299** has spatial resolution equal to or better than ⅓ of the Talbot fringe period in the two orthogonal directions in the image plane and is positioned to be aligned with the Talbot fringe pattern.

Such embodiments with 2-D patterns on the beam splitting grating G_1 **210**-**2**D may also be used with the previously described lower resolution detector **290** in conjunction with a two-dimensional analyzer grating G_2 which may be phase stepped in two directions in any sequence so that the phase information is obtained in both orthogonal directions. Similar to the description of G_1 **210**-**2**D above, this 2-D analyzer grating G_2 may be of any periodic structure such as a mesh, a checkerboard, or 2-D array of structures such as circles, triangles, squares, rectangles, etc.

FIG. **19** represents an embodiment similar to FIG. **16**, except that the object **240**-M under examination is now placed between the x-ray source and the beam-splitting grating **210**-**2**D.

Note that some of the embodiments are one-dimensional Talbot-Yun interferometers in which absorption, phase, and scattering information is obtained in one direction and incorporate one or more 1-D gratings in combination with a micro structured source target that is periodic in at least in the direction perpendicular to the grating line direction (but may be periodic in other directions as well). Other embodiments are two-dimensional Talbot-ST interferometers in which absorption, phase, and scattering information is obtained in two orthogonal directions (or all three dimensions by performing computed tomography using the 2-D Talbot-Yun setup).

FIGS. **20** and **21** illustrate another embodiment of the invention in which the x-ray source **080** comprises a vacuum chamber **020** supported on mounts **030** within an x-ray shielding housing **050**. The source **080** also comprises a target **100** comprising a substrate **1000** and a periodic pattern comprising x-ray sub-sources **700** mounted entirely within the vacuum chamber **020**. As before, this embodiment also comprises a high voltage source **010**, which has a negative terminal connected through a lead **021**-A to an electron emitter **011**-A, while the positive terminal is connected through one or more leads **022** to the microstructures in the target, allowing them to serve as an anode.

However, in this embodiment, the surface of the target **100** comprising the periodic array of x-ray sub-sources **700** comprising of x-ray generating material is facing a window **040** mounted in the wall of the vacuum chamber **020**, and the electron emitter **011**-A is aligned to emit a beam of electrons **111**-A onto the surface of the target **100** comprising sub-sources **700** facing the window **040**.

FIGS. **22** and **23** illustrate another embodiment of the invention in which the target **100** comprising a substrate **1000** and a periodic pattern comprising x-ray sub-sources **700** mounted entirely within the vacuum chamber **020**. As before, this embodiment also comprises a high voltage source **010**, which has a negative terminal connected through a lead **021**-B to an electron emitter **011**-B, while the positive terminal is connected through one or more leads **022** to the microstructures in the target, allowing them to serve as an anode.

However, in this embodiment, the surface of the target **100** comprising the periodic array of x-ray sub-sources **700** comprising x-ray generating material is oriented such that x-rays produced by some of the microstructures propagate towards other microstructures that are also producing x-rays, and a linear accumulation of x-rays **888**-B from a plurality of microstructures **700** emerges from the target. The distance g between the microstructures and microstructures **700** emerges from the target. The distance g between the microstructures and the width w_x in the propagation direction should be small enough such that the emission from the nth microstructure contributing to the accumulated x-rays can be considered as a single sub-source with dimension a of Eqn. 9, i.e.:

$$a \geq \tan\theta \cdot (n(g+w_x)) \qquad \text{[Eqn. 10]}$$

where a is the sub-source dimension that meets the coherence requirements of the system, and θ is one half of the field-of-view angle for the system.

Linear accumulation of x-ray sources as used in this embodiment of the invention is described more fully in the co-pending U.S. patent application entitled X-RAY SOURCES USING LINEAR ACCUMULATION by the inventors of the present invention (U.S. patent application Ser. No. 14/490,672 filed Sep. 19, 2014), which is hereby incorporated by reference in its entirety. Any of the source designs and configurations disclosed in the above referenced co-pending application may be considered for use as a component in any or all of the interferometric imaging systems disclosed herein.

Likewise, FIGS. **24** and **25** illustrate another embodiment of the invention that utilizes linear accumulation of x-rays. In this embodiment, the x-ray source **080** includes a target **2200** comprising a substrate **2210** and a first set of sub-sources **707** and a second set of sub-sources **708** mounted entirely within the vacuum chamber **020**. As before, this embodiment also comprises a high voltage source **010**, but this high voltage source is connected to a junction **010-2** that provides high voltage to two electron emitters **011**-D and **011**-E through leads **021**-D and **021**-E, respectively. As shown in FIGS. **24** and **25**, the first electron emitter **021**-D provides an electron beam **111**-D that bombards the first set of sub-sources **707**, while the second electron emitter **021**-E provides an electron beam **111**-E that bombards the second set of sub-sources **708**. Some of the x-rays **788** generated by the first set of sub-sources **707** and the second set of sub-sources **708** along the x-ray imaging beam axis combine to produce x-rays **2888** from the target **2200** will be augmented by the linear accumulation of x-rays from these two sets of x-ray sub-sources. In some embodiments, the separation between the two sets of sub-sources **707** and **708** may be smaller than 5 mm but larger than the source size in direction perpendicular to a line passing through the center of the two sub-sources. The periods of both the sub-sources **707** and **708** may be selected so that the associated Talbot fringes downstream of the beam splitting grating G_1 substantially overlap.

It will also be known to those skilled in the art that other embodiments of the invention comprising an x-ray source in which the target/anode under bombardment by electrons is moved, translated, or rotated to distribute the heat load are also possible.

Note: The illustrations of FIGS. **10** through **25** are not shown to scale, and are meant to illustrate the principle of the invention and not specific relationships between the microstructures **700**, the target **100** and the various grating periods p_1 and p_2. The microstructures **700**, **701**, **707**, **708** etc. may be on the order of microns in size, while the object under examination **240**-M may be centimeters in size. Likewise, although these are illustrated in which an object with dimensions on the order of centimeters (a mouse) is shown, the techniques described are not limited to such objects, but may be used to examine even larger structures, or microscopic structures as well, as long as a suitable resolution for the detector and other elements of the interferometer are suitably constructed.

2. Fabrication of X-Ray Targets

Targets such as those to be used in x-ray sources according to the invention disclosed herein have been described in detail in the U.S. patent application entitled STRUCTURED TARGETS FOR X-RAY GENERATION by the inventors of the present invention (U.S. patent application Ser. No. 14/465,816, filed Aug. 21, 2014), which is hereby incorporated by reference in its entirety. Any of the target designs and configurations disclosed in the above referenced co-pending application may be considered for use as a component in any or all of the x-ray sources disclosed herein.

As described herein and in the above cited pending patent applications, the target used in the source of x-rays may comprise a periodic array of sub-sources. Each sub-source may be comprised of a single or multiple microstructures of x-ray generating material in thermal contact with, or preferably embedded in, a substrate selected for its thermal conductivity. When the microstructures are in good thermal contact with a substrate having a high thermal conductivity, higher electron current densities may be used to generate x-rays, since the excess heat will be drawn away into the substrate. The higher current densities will give rise to higher x-ray flux, leading to a higher brightness source. As described in the above co-pending patent applications, sources with microstructures of x-ray generating material may have a brightness more than 10 times larger than simpler constructions made from the same materials. Additional configurations in which multiple sub-sources are aligned to contribute x-rays on the same axis can multiply the brightness further through linear accumulation of the x-ray sub-sources.

It should also be noted here that, when the word "microstructure" is used herein, it is specifically referring to microstructures comprising x-ray generating material. Other structures, such as the cavities used to form the x-ray microstructures, have dimensions of the same order of magnitude, and might also be considered "microstructures". As used herein, however, other words, such as "structures", "cavities", "holes", "apertures", etc. may be used for these structures when they are formed in materials, such as the substrate, that are not selected for their x-ray generating properties. The word "microstructure" will be reserved for structures comprising materials selected for their x-ray generating properties.

Likewise, it should be noted that, although the word "microstructure" is used, x-ray generating structures with dimensions smaller than 1 micron, or even as small as nano-scale dimensions (i.e. greater than 10 nm) may also be described by the word "microstructures" as used herein as long as the properties are consistent with the geometric factors for sub-source size and grating pitches set forth in the various embodiments.

It should also be noted that here that, when the word "sub-source" is used it may refer to a single microstructure of x-ray generating material, or an ensemble of smaller microstructures that function similarly to a single structure for the purposes of Talbot interferometry.

The fabrication of these microstructured targets may follow well known processing steps used for the creation of embedded structures in substrates. If the substrate is a material with high thermal conductivity such as diamond, conventional lithographic patterning, such as focused ion beam lithography or electron beam lithography, using photoresists can produce micron sized structures, which may then be etched into the substrate using processes such as reactive ion etching (RIE). Deposition of the x-ray generating material into the etched structures formed in the substrate may then be carried out using standard deposition processes, such as electroplating, chemical vapor deposition (CVD), atomic layer deposition, or hot pressing.

The x-ray generating material used in the target should ideally have good thermal properties, such as a high melting point and high thermal conductivity, in order to allow higher electron power loading on the source to increase x-ray production. The x-ray generating material should additionally be selected for good x-ray production properties, which includes x-ray production efficiency (proportional to its atomic number) and in some cases, it may be desirable to produce a specific spectra of interest, such as a characteristic x-ray spectral line. For these reasons, targets are often fabricated using tungsten, with an atomic number Z=74. Table I lists several materials that are commonly used for x-ray targets, several additional potential target materials (notably useful for specific characteristic lines of interest), and some materials that may be used as substrates for target materials. Melting points, and thermal and electrical conductivities are presented for values near 300° K (27° C.). Most values are cited from the CRC Handbook of Chemistry and Physics, 90^{th} ed. [CRC Press, Boca Raton, Fla., 2009]. Other values are cited from various sources found on the Internet. Note that, for some materials Ouch as sapphire for example) thermal conductivities an order of magnitude larger may be possible when cooled to temperatures below that of liquid nitrogen (77° K) [see, for example, Section 2.1.5, Thermal Properties, of E. R. Dobrovinskaya et al., Sapphire: Material, Manufacturing, Applications, Springer Science+Business Media, LLC, 2009].

TABLE I

Various Target and Substrate Materials and Selected Properties.

Material (Elemental Symbol)	Atomic Number Z	Melting Point ° C. (1 atm)	Thermal Conductivity (W/(m ° C.))	Electrical Conductivity (MS/m)
Common Target Materials:				
Chromium (Cr)	24	1907	93.7	7.9
Iron (Fe)	26	1538	80.2	10.0
Cobalt (Co)	27	1495	100	17.9
Copper (Cu)	29	1085	401	58.0
Molybdenum (Mo)	42	2623	138	18.1
Silver (Ag)	47	962	429	61.4
Tungsten (W)	74	3422	174	18.4
Other Possible Target Materials:				
Titanium (Ti)	22	1668	21.9	2.6
Gallium (Ga)	35	30	40.6	7.4
Rhodium (Rh)	45	1964	150	23.3
Indium (In)	49	157	81.6	12.5
Cesium (Cs)	55	28	35.9	4.8
Rhenium (Re)	75	3185	47.9	5.8
Gold (Au)	79	1064	317	44.0
Lead (Pb)	82	327	35.3	4.7
Other Potential Substrate Materials with low atomic number:				
Beryllium (Be)	4	1287	200	26.6
Carbon (C): Diamond	6	*	2300	10^{-19}
Carbon (C): Graphite ||	6	*	1950	0.25
Carbon (C): Nanotube (SWNT)	6	*	3180	100.0
Carbon (C): Nanotube (bulk)	6	*	200	
Boron Nitride (BN)	B = 5 N = 7	**	20	10^{-17}
Silicon (Si)	14	1414	124	1.56×10^{-9}
Silicon Carbide (β-siC)	Si = 14 C = 6	2798	0.49	10^{-9}
Sapphire (Al_2O_3) || C	Al = 13 O = 8	2053	32.5	10^{-20}

* Carbon does not melt at 1 atm; it sublimes at ~3600° C.

** BN does not melt at 1 atm; it sublimes at ~2973° C.

FIG. **26** illustrates a target as may be used in some embodiments of the invention. In this figure, a substrate **1000** has a region **1001** that comprises an array of sub-sources **700** comprising microstructures of x-ray generating material (typically a metallic material), in which the sub-sources are arranged in a regular array of right rectangular prisms. In a vacuum, electrons **111** bombard the target from above, and generate heat and x-rays in the microstructures **700**. The material in the substrate **1000** is selected such that it has relatively low x-ray production (efficiency is proportional to atomic number) and energy deposition rate (stopping power is proportional to density) for electrons in comparison to the x-ray generating microstructure material, and therefore will not generate a significant amount of heat and x-rays. This is typically achieved by selecting a low mass density and low atomic number (Z) material for the substrate.

The substrate **1000** material may also be chosen to have a high thermal conductivity, typically larger than 100 W/(m ° C.), and the microstructures are typically embedded within the substrate, i.e. if the microstructures are shaped as rectangular prisms, it is preferred that at least five of the six sides are in close thermal contact with the substrate **1000**, so that heat generated in the microstructures **700** is effectively conducted away into the substrate **1000**. However, targets used in other embodiments may have fewer direct contact surfaces. In general, when the term "embedded" is used in this disclosure, at least half of the surface area of the microstructure will be in close thermal contact with the substrate.

Note that the sub-source sizes and dimensions in some embodiments may be constrained by the same limitations as the periodicity p_0 of the grating G_0 in prior art. In other words, the spatial resolution achievable at the object position in the x-ray interferometric imaging systems as shown in FIGS. **9** through **25** is determined by the overall x-ray source size and the detector resolution, similar to the conditions described in the prior art interferometeric imaging systems, such as the Talbot-Lau system. Therefore, the maximum x-ray source size (width of each microstructure spot) is limited for a given detector resolution and a given imaging geometry as determined by the distance between the source and object and the distance between the object to the detector.

The line-to-space ratio of the arrays of sub-sources is a design parameter that should be considered in the design of any system. A large spatial coherence length is inversely proportional to the size of an x-ray source or sub-source. Because the fringe visibility of the Talbot interference fringes increases linearly with the relative ratio of the spatial coherence length of the illuminating x-ray beam to the period of the beam-splitting grating p_1 for a value of the ratio from 0.3 to 1, it is generally preferred to have a small source size. However, the x-ray production is inversely proportional to the area of the sub-source (e.g. a reduction in line width will lead to a decrease of x-ray production). Since the throughput of an imaging system is generally proportional to square of the contrast transfer function and only proportional to the x-ray flux, it is generally preferred to have a line-to-space ration less than 1:1. Some embodiments of the invention may use a line-to-space (i.e. x-ray generating material to substrate material) ratio between 1:5 and 1:2 (i.e. the relative area of the x-ray generating material may range from 20% to 33%).

A figure of merit (FOM) that may be helpful for the selection of materials for targets according to this invention is the ratio of x-rays produced by the microstructures to the x-rays produced by the electrons also bombarding the substrate. This figure of merit may be useful for the design of and selection of materials for the targets for the system, and should be taken into consideration in addition to the thermal conductivity of the substrate. As the electron energy deposition rate is proportional to the mass density and the x-ray production efficiency in a material is proportional to its atomic number, this figure of merit may be defined as follows:

$$\mathrm{FOM} = \frac{Z_2 \times \rho_2}{Z_1 \times \rho_1} \qquad \text{[Eqn. 11]}$$

where Z is the atomic number and ρ is the density, and material **1** is the substrate and material **2** is the x-ray generating material.

TABLE II

Figure of Merit for x-ray material/substrate combinations.

Substrate material			Microstructure material			Figure of Merit
Material	Atomic # Z_1	Mass density (g/cm^3)	Material	Atomic # Z_2	Mass density (g/cm^3)	$\frac{Z_2 \times \rho_2}{Z_1 \times \rho_1}$
SiC	12.55	3.21	Cu	29	8.96	6
Si	14	2.33	Cu	29	8.96	8
SiC	12.55	3.21	Mo	42	10.2	11
Diamond	6	3.5	Cu	29	8.96	12
Si	14	2.33	Mo	42	10.2	13
Diamond	6	3.5	Mo	42	10.2	21
SiC	12.55	3.21	W	74	19.25	35
Be	4	1.85	Cu	29	8.96	35
Si	14	2.33	W	74	19.25	44
Be	4	1.85	Mo	42	10.2	59
Diamond	6	3.5	W	74	19.25	68
Be	4	1.85	W	74	19.25	193

A number of microstructures and substrate material combinations are listed below in Table II. Any of the following combinations may be used, but it is preferable that the materials are selected such that the FOM is greater than 12, and that the thermal conductivity of the substrate material is greater than 100 W/(m ° C.) at room temperature.

FIG. **27** illustrates another target as may be used in some embodiments of the invention in which the electron beam **111**-F is directed by electrostatic lenses to form a more concentrated, focused spot. For this situation, the target **1100**-F will still comprise a region **1001**-F comprising an array of microstructures **700**-F comprising x-ray material, but the size and dimensions of this region **1001**-F can be matched to regions where electron exposure will occur. In these targets, the "tuning" of the source geometry and the x-ray generating material can be controlled such that the designs mostly limit the amount of heat generated to the micro structured region **1001**-F, while also reducing the design and manufacturing complexity. This may be especially useful when used with electron beams focused to form a micro-spot, or by more intricate systems that form a more complex electron exposure pattern.

The depth of penetration of electrons into the material can be estimated by Pott's Law [P. J. Potts, Electron Probe Microanalysis, Ch. 10 of A Handbook of Silicate Rock Analysis, Springer Netherlands, 1987, p. 336)], which states that the penetration depth x in microns is related to the 10% of the value of the electron energy E_0 in keV raised to the 3/2 power, divided by the density of the material:

$$x(\mu\mathrm{m}) = 0.1 \times \frac{E_0^{1.5}}{\rho} \qquad \text{[Eqn. 12]}$$

For less dense material, such as a diamond substrate, the penetration depth is much larger than for a material with greater density, such as most materials containing elements used for x-ray generation.

Using this formula, Table III illustrates some of the estimated penetration depths for some common x-ray target materials.

TABLE III

Estimates of penetration depth for 60 keV electrons into some materials.

Material	Z	Density (g/cm^3)	Penetration Depth (μm)
Diamond	6	3.5	13.28
Copper	29	8.96	5.19
Molybdenum	42	10.28	4.52
Tungsten	74	19.25	2.41

The majority of characteristic Cu K x-rays are generated within the penetration depth. The electron interactions below that depth typically generate few characteristic K-line x-rays but will contribute to the heat generation, thus resulting in a low thermal gradient along the depth direction. It is therefore preferable in some embodiments to set a maximum thickness for the microstructures in the target in order to limit electron interaction in the material and optimize local thermal gradients. One embodiment of the invention limits the depth of the micro structured x-ray generating material in the target to between one third and two thirds of the electron penetration depth in the substrate at the incident electron energy. In this case, the lower mass density of the substrate leads to a lower energy deposition rate in the substrate material immediately below the x-ray generating material, which in turn leads to a lower temperature in the substrate material below. This results in a higher thermal gradient between the x-ray generating material and the substrate, enhancing heat transfer. The thermal gradient is further enhanced by the high thermal conductivity of the substrate material.

For similar reasons, selecting the thickness of the microstructures to be less than one half of the electron penetration depth in the substrate is also generally preferred for efficient generation of bremsstrahlung radiation, because the electrons below that depth have lower energy and thus lower x-ray production efficiency.

Note: Other choices for the dimensions of the x-ray generating material may also be used. In targets as used in some embodiments of the invention, the depth of the x-ray material may be selected to be 50% of the electron penetration depth in the substrate. In other embodiments, the depth of the x-ray material may be selected to be 33% of the electron penetration depth in the substrate. In other embodiments, the depth for the microstructures may be selected related to the "continuous slowing down approximation" (CSDA) range for electrons in the material. Other depths may be specified depending on the x-ray spectrum desired and the properties of the selected x-ray material.

FIG. **28** illustrates a region **1001** of a target as may be used in some embodiments of the invention that comprises an array of sub-sources **700** with microstructures in the form of right rectangular prisms comprising x-ray generating material arranged in a regular array. FIG. **28**A presents a perspective view of the sixteen microstructures **700** for this target, while FIG. **28**B illustrates a top down view of the same region, and FIG. **28**C presents a side/cross-section view of the same region. (For the term "side/cross-section view" in this disclosure, the view meant is one as if a cross-section of the object had been made, and then viewed from the side towards the cross-sectioned surface. This shows both detail at the point of the cross-section as well as material deeper inside that might be seen from the side, assuming the substrate itself were transparent [which, in the case of diamond, is generally true for visible light].)

In these targets, the microstructures have been fabricated such that they are in close thermal contact on five of six sides with the substrate. As illustrated, the top of the microstructures **700** are flush with the surface of the substrate, but other targets in which the microstructure is recessed may be fabricated, and still other targets in which the microstructures present a topographical "bump" relative to the surface of the substrate may also be fabricated.

An alternative target as may be used in some embodiments of the invention may have several microstructures of right rectangular prisms simply deposited upon the surface of the substrate. In this case, only the bottom base of the prism would be in thermal contact with the substrate. For a structure comprising the microstructures embedded in the substrate with a side/cross-section view as shown in FIG. **28**C with depth D_z and lateral dimensions in the plane of the substrate of W_x and W_y, the ratio of the total surface area in contact with the substrate for the embedded microstructures vs. deposited microstructures is

$$\frac{A_{Embedded}}{A_{Deposited}} = 1 + 2D\frac{(W+L)}{(W \times L)} \quad \text{[Eqn. 13]}$$

With a small value for D relative to W and L, the ratio is essentially 1. For larger thicknesses, the ratio becomes larger, and for a cube (D=W=L) in which 5 equal sides are in thermal contact, the ratio is 5. If a cap layer of a material with similar properties as the substrate in terms of mass density and thermal conductivity is used, the ratio may be increased to 6.

FIG. **29** illustrates a region **1001** of a target as may be used in some embodiments of the invention, such as that previously illustrated in FIG. **13**, that comprises an array of linear sub-sources **701** with microstructures in the form of right rectangular prisms comprising x-ray generating material arranged in a regular array. FIG. **29**A presents a perspective view of the three microstructures **701** for this target, while FIG. **29**B illustrates a top down view of the same region, and FIG. **29**C presents a side/cross-section view of the same region.

In this embodiment, the lateral dimensions in the plane of the substrate are a width and length W_x and L_y. The effective sub-source size a will correspond to the width W_x.

FIGS. **30** and **31** illustrate a practical issue that may arise in forming the targets such as those illustrated in FIGS. **28** and **29**. FIG. **30** illustrates variations possible with the grid of x-ray generating microstructures **700** as illustrated in FIG. **28**, and FIG. **31** illustrates variations possible with the linear x-ray generating microstructures **701** as illustrated in FIG. **29**.

In FIG. **30**, odd-shaped microstructures **700**-A of other geometric shapes may be formed. Likewise, voids **700-0** may also appear where certain structures may be expected. Other deposition processes, for example deposition using pre-formed particles of x-ray generating material may create ensemble clusters of particles **700**-C that, when bombarded with electrons, may still act as x-ray sub-sources similar in function to those that are produced by a uniform structure. Also shown in FIG. **30** is a microstructure with multiple crystal structures and grain boundaries **700**-G that again may still produce x-rays similar to those that are produced by a uniform structure, but may be considered to comprise an ensemble of microstructures.

The effective x-ray sub-source size in all of these situations may be approximated using the size parameter a, even though the microstructures comprise particles that are considerable smaller.

FIG. **31** shows examples of ensemble microstructures as may occur when fabricating linear microstructures **701**. If uniform pre-fabricated particles of x-ray generating material are created and coated onto the substrate, an ensemble of particles **703** of x-ray generating material may be formed. In other processes, if non-uniform particles are used, clusters of particles **704**-A and **704**-B may form, in some cases with a non-uniform distribution that may include gaps of voids. In other processes, an ensemble of particles **704** of x-ray generating material may approximate a line source of x-rays.

All of these ensembles, when bombarded with electrons, may still act as x-ray sub-sources similar in function to those that are produced by a uniform linear structure. The effective source size in these situations may be approximated using the size parameter a, even though the microstructures comprise particles that are considerable smaller.

The heat transfer that may occur under electron bombardment is illustrated with representative arrows in FIG. **32**, in which the heat generated in sub-sources **700** embedded in a substrate **1000** is conducted out of the microstructures comprising the sub-sources **700** through the bottom and sides (arrows for transfer through the sides out of the plane of the drawing are not shown). The amount of heat transferred per unit time (ΔQ) conducted through a material of area A and thickness d given by:

$$\Delta Q = \frac{\kappa \cdot A \cdot \Delta T}{d} \quad \text{[Eqn. 14]}$$

where κ is the thermal conductivity in W/(m ° C.) and AT is the temperature difference across thickness d in ° C. Therefore, an increase in surface area A, a decrease in thickness d and an increase in ΔT all lead to a proportional increase in heat transfer.

An alternative embodiment is illustrated in FIG. **33**, in which the substrate additionally comprises a cooling channel **1200**. Such cooling channels may be a prior art cooling channel, as discussed above, using water or some other cooling fluid to conduct heat away from the substrate, or may be fabricated according to a design adapted to best remove heat from the regions near the embedded microstructures **700**.

Other target structures for various embodiments may be understood or devised by those skilled in the art, in which the substrate may, for example, be bonded to a heat sink, such as a copper block, for improved thermal transfer. The copper block may in turn have cooling channels within it to assist in carrying heat away from the block. Alternatively, the substrate may be attached to a thermoelectric cooler, in which a voltage is applied to a specially constructed semiconductor device. In these devices, the flow of current causes one side to cool while the other heats up. Commercially available devices, such as Peltier coolers, can produce a temperature difference of up to 70° C. across the device, but may be limited in their overall capacity to remove large amounts of heat from a heat source. Heat pipes containing a heat transfer fluid that evaporates and condenses, as are used for cooling CPU chips in server farms when compact design is a consideration, may also be used to cool the substrate.

Alternatively, the substrate can be attached to a cryogenic cooler, such as a block containing channels for the flow of liquid nitrogen, or be in thermal contact with a reservoir of liquid nitrogen or some other cryogenic substance, such as an antifreeze solution, to provide more extreme cooling. When the substrate comprises a material such as diamond, sapphire, silicon, or silicon carbide, thermal conductivity generally increases with decreasing temperature from room temperature. In such a case, designing the target so that it can withstand cooling to these lower temperatures may be preferred.

FIG. **34** illustrates an alternative example of a target that may be used in embodiments of the invention in which the cavities formed in the substrate **1000** are first coated with an adhesion layer **715** (preferably of minimal thickness) before embedding the x-ray generating material that forms the microstructures **700**. Such an adhesion layer may be appropriate in cases where the bond between the x-ray material and the substrate material is weak. The adhesion layer may also act as a buffer layer when the difference between thermal expansion coefficients for the two materials is large. For some choices of materials, the adhesion layer may be replaced or extended (by adding another layer) with a diffusion barrier layer to prevent the diffusion of material from the microstructures into the substrate material (or vice versa). For embodiments in which an adhesion and/or diffusion barrier layer is used, the selection of materials and thicknesses should consider the thermal properties of the layer as well, such that heat flow from the microstructures **700** to the substrate **1000** is not significantly impeded or insulated by the presence of the adhesion layer **715**.

FIG. **35** illustrates an alternative example of a target that may be used in an embodiment in which an electrically conducting layer **725** has been added to the surface of the target. When bombarded by electrons, the excess charge needs a path to return to ground for the target to function effectively as an anode. If the target as illustrated in FIGS. **28** and **29** were to comprise only discrete, unconnected microstructures **700** within an electrically insulating substrate material (such as undoped diamond), under continued electron bombardment, significant charge would build up on the surface. The electrons from the cathode would then not collide with the target with the same energy, or might even be repelled, diminishing the generation of x-rays.

This can be addressed by the deposition of a thin layer of conducting material that is preferably of relatively low atomic number, such as aluminum (Al), beryllium (Be), carbon (C), chromium (Cr) or titanium (Ti), that allows electrical conduction from the discrete microstructures **700** to an electrical path **722** that connects to a positive terminal relative to the high voltage supply. This terminal as a practical matter is typically the electrical ground of the system, while the cathode electron source is supplied with a negative high voltage.

FIG. **36** illustrates another example of a target that may be used in an embodiment of the invention, in which the sub-sources **702** are embedded deeper, or buried, into the substrate **1000**. Such an embedded microstructure may be further covered by the deposition of an additional layer **1010**, which may be, for example, diamond, providing the same heat transfer properties as the substrate. This allows heat to be conducted away from all sides of the buried sub-source **702**. For such a situation and when the additional layer **1010** does not have sufficient electrical conductivity, it is advisable to provide a path **722** to ground for the electrons incident on the structure, which may be in the form of an embedded conducting layer **726** laid down before the deposition of the additional layer **1010**. In some embodiments, this conducting layer **726** will have a "via" **727**, or a vertical connection, often in the form of a pillar or cylinder, that provides an electrically conducting structure to link the embedded conducting layer **726** to an additional conducting layer **728** on the surface of the target, which in turn is connected to the path **722** to ground, or the high voltage supply.

FIG. **37** illustrates another example of a target that may be used in embodiments of the invention, in which the sub-sources **702** are again buried within the substrate. However, in this embodiment, instead of first providing an electrically conducting layer followed by the deposition of an additional cap layer, in this embodiment only a single layer **770** is deposited, selected for a combination of electrical properties and thermally conducting properties. This may be, for example, a deposition of carbon nanotubes (Z=6) oriented vertically relative to the surface, such that they conduct both heat and electrons away from the buried microstructures **702**. This single layer **770** may in turn be connected to a path **722** to ground to allow the target to serve as an anode in the x-ray generation system. Alternatively, the material of the layer **770** may be selected to comprise aluminum (Al), beryllium (Be), chromium (Cr), or copper (Cu).

FIG. **38** illustrates another variation of an embodiment, in which additional patterns of blocking material **729** have been deposited on the backside of the target substrate **1000**. If the figure of merit for the selected material combination, as discussed above in Table II, is not large, there may still be significant x-rays generated by the substrate that will reduce contrast in the image. These substrate-generated x-rays can be blocked by a deposition of a suitable material, such as gold, as blocking structures **729**. Gold (Z=79) has a strong x-ray absorption, as illustrated in FIG. **39**. Processes to deposit these blocking structures may comprise standard deposition processes, and an alignment step may be needed to ensure alignment with the x-ray generating structures on the opposite side.

It should be clear to those skilled in the art that although several embodiments have been presented separately in FIGS. **26**-**38**, and various processes for their manufacture will be presented later, the elements of these embodiments may be combined with each other, or combined with other commonly known target fabrication methods known in the art. For example, the buried sub-sources **702** of FIG. **37** may also comprise multiple grains of microstructures, as was illustrated in FIGS. **30** and **31**. Likewise, the adhesion layer **715** as illustrated in FIG. **34** may also be applied to fabrication of embedded sub-sources **700** as shown in FIG. **35**. The separation of these alternatives is for illustration only, and is not meant to be limiting for any particular process.

Although the sub-sources illustrated in FIGS. **26**-**38** have been shown as regularly spaced patterns with uniform size and shape, a regular pattern of sub-sources having non-uniform size and shape, can also be used in some embodiments of the invention. Additionally, each sub-source within a regular periodic pattern may further be comprised of multiple smaller microstructures of non-uniform sizes and shapes. These smaller microstructures may be non-regular and do not necessarily need to have similar x-ray emission characteristics or strength, so as long as the larger sub-sources that each group of microstructures comprise are periodic in nature.

Likewise, although some embodiments have been described with microstructures in, for example, the shape of right rectangular prisms, fabrication processes may create structures that have walls at angles other than 90°, or do not have corners that are exactly right angles, but may be rounded or beveled or undercut, depending on the artifacts of the specific process used. Embodiments in which the microstructures are essentially similar with the shapes described herein will be understood by those skilled in the art to be disclosed, even if process artifacts lead to some deviation from the shapes as illustrated or described.

In other embodiments of the system, a periodic attenuating grating G_0 such as are used in the prior art Talbot-Lau interferometers may also be used in conjunction with the source of the invention, so that the x-rays produced by the substrate material surrounding the sub-sources are further attenuated, allowing greater monochromaticity and therefore higher spatial coherence for the source. The apertures of the grating should be coincident with projections of the microstructured x-ray sub-sources, or may, in some embodiments, be placed at a Talbot fractional or integer distance downstream of the source and with the apertures coincident with the source self-images. It is preferable that the grating G_0 is of high atomic number and relatively low aspect ratio, for ease of manufacturability.

3. Additional Embodiments

3.1. An Additional Absorption Grid

Additional embodiments may comprise an additional absorption grid, with features and placement designed to reduce scattered radiation (such as Compton scattering and elastic scattering from fine structures with dimensions substantially smaller than the resolution of an imaging system) that contributes to the background in x-ray imaging and reduction of image contrast in many x-ray imaging techniques, including the various embodiments discussed above or various x-ray absorption imaging techniques. The ratio of the intensity of the scattered radiation to the intensity of the primary radiation used forming the images is particularly significant in imaging examinations where a large quantity of scatter is created, e.g., those involving a large volume of tissue being irradiated and those requiring high energy x-rays, thus limiting the efficacy of disease diagnosis for obese patients or for dense body parts (e.g. craniofacial, dense breast tissue, etc.). Current art in antiscattering grids typically comprise high radiation absorption septa (typically fabricated using high Z materials like lead) interlaced with a medium with high radiation transmission (such as aluminum or fiber material). It is typically specified by the grid ratio (ratio of the height of the structures and the interspacing between them), period, and septum width. Use of an antiscattering grid, however, requires a greater radiation exposure to the patient as a fraction of primary beam is also attenuated by the septa.

A common drawback for existing antiscattering grids is that the septa also absorb the useful primary x-rays transmitted through the object, resulting in an undesirable reduction of the image signal and therefore an increased radiation dose to the sample or patient.

The embodiments of the invention as previously disclosed above may also be augmented by the use of an antiscattering grid having a pattern of septa determined by specific imaging setup designed to use the Talbot effect. One embodiment of the invention comprises an antiscattering grid positioned between the beam splitting grating G_1 and the detector. The period of the grid spacing and the position may be determined so that the septa are at positions that should be the nodes in the Talbot carpet. The antiscattering grid preferably absorbs the scattered radiation while permitting efficient transmission of the primary radiation, resulting in reduction of background noise and increase in image contrast. The antiscattering grid may comprise simple 1-D structures for the septa, but may also be designed to have 2-D or even 3-D structures tuned to the Talbot interference pattern with which they are intended to be used.

An embodiment of the invention incorporating an antiscattering grid is illustrated in FIG. **40**. As in the other embodiments illustrated in this disclosure, x-rays **888** are generated from microstructured regions **700** comprising x-ray generating material upon bombardment with an electron beam **111**. The generated x-rays are transmitted through a sample, in this case a mouse **240**-M, and the transmitted x-rays are detected on a detector **290**. However, in passing through the mouse **240**-M, Compton scattering and other undesired scattering phenomena may occur, producing x-rays **889**-C that may propagate at many different angles and reduce the absorption image contrast.

The insertion of an anti-scatter grid **420** helps to attenuate the scattered x-rays, while passing the majority of the x-rays that contribute to image formation. Here, the antiscattering grid **420**, designated as G_4, is positioned at a distance D_α from the beam splitting grating **210**, designated as G_1. The antiscattering grid **420** will typically comprise a substrate **422** that is made from a material mostly transparent to x-rays (such as aluminum or a carbon fiber material), upon which a number of absorbing structures **424** comprising material that absorbs x-rays, such as gold, tin, platinum, tungsten, tantalum, nickel, lead, copper, gadolinium, or some other high Z material, have been arranged in a periodic manner. The thickness of the absorbing structures **424** is determined by the X-ray imaging energy which is in turn determined by application; for example, for imaging at 40 keV of infants, the thickness of such structures may be on the order of several hundred microns for lead. In some embodiments, the substrate and absorbing structures may both be fabricated from a single wafer or block of high Z material. The space between the absorbing structures **424** may comprise only air, or may have another low Z material deposited therein. In such embodiments, the distance D_α from the beam splitting grating G_1 will be set such that the position is at one of the fractional Talbot distances, i.e.

$$D_\alpha = D_N = N\frac{p_1^2}{8\lambda} = \frac{N}{16}D_T \qquad \text{[Eqn. 15]}$$

where D_N is the fractional Talbot distance for a plane wave illumination, λ is the mean x-ray wavelength, and N is referred to as a Talbot fractional order.

The period of the structures in the antiscattering grid may be set to be

$$p_4 = Kp_0\frac{D_\alpha}{L} \qquad \text{[Eqn. 16]}$$

where p_0 is the period of the microstructured source, L the distance between the x-ray sources **700** and the beam splitting grating **210**, and K is a scaling factor which is equal to 1 when the beam-splitting grating introduces a phase shift of $\pi/2$, and is equal to ½ when the beam-splitting grating introduces a phase shift of π.

The antiscattering grid may be a 1-D grating, or a 2-D grating, with the periods in the x and y axes corresponding using Eqn. 16 above with the corresponding (e.g., horizontal and vertical) periods in the beam splitting grating. In some embodiments, the absorbing septa will be arranged with an aspect ratio of >5:1, i.e. with features 5 times or more higher than the width of the gap between features, and the normal-incidence transmission of the absorbing regions will be less than 10%. Septa may be designed such that the ratio of the area of the septa to the total area ranges from 20-50%. The position may be controlled by a controller **425** that may allow the antiscattering septa to be aligned with the interference fringes formed by the beam splitting grating **210**.

Some scattered x-rays may still propagate at angles and in directions that allow it to be transmitted through the apertures in the antiscattering grid. However, by placing the antiscattering grid such that the absorbing structures are co-positioned with the nodes of the Talbot fringe pattern, nearly 100% of the Talbot fringe pattern may be transmitted, while 50% to 75% or more of the scattered x-rays may be absorbed. In some embodiments, the absorbing structures are not matched to each node but may instead be matched to integer multiples of the nodes.

Further reduction in scattered x-rays may be achieved by including a second antiscattering grid. This second grid may be placed at the same Talbot distance in close proximity to the first antiscattering grating, effectively increasing the absorption and aspect ratio of the features, or it may be positioned at another Talbot distance using the same design consideration as discussed in the previous embodiments.

FIG. **41** illustrates the placement of two antiscattering grids in the Talbot image of a phase grating. The Talbot pattern as illustrated corresponds to a 1:1 $\pi/2$ phase grating, as has been previously presented in references such as "X-Ray Phase Imaging with Talbot Interferometry" by A Momose et al. in BIOMEDICAL MATHEMATICS: Promising Directions in Imaging, Therapy Planning, and Inverse Problems (Medical Physics Publishing, Madison Wis., 2010), pp. 281-320.

The x-rays **889** transmitted through a sample enter from the left and fall onto the 1:1 $\pi/2$ phase grating **210**. Under spatially coherent illumination, the grating produces a Talbot carpet, as discussed in the previous embodiments. At the third fractional Talbot distance (N=3), an absorption grating **420** is placed and positioned so that the absorbing features, designated by a set of white boxes denoting x-ray blocking material in FIG. **41**, are aligned with the nodes of the Talbot carpet. At the fifth fractional Talbot distance (N=5), another absorption grating **430** is placed and positioned so that the absorbing features, designated by a set of white boxes denoting x-ray blocking material in FIG. **41**, are aligned with the nodes of the Talbot carpet. Scattered x-rays **889**-C, illustrated by white arrows, will mostly be blocked by these absorption gratings **420** and **430**, while the intensity of the Talbot pattern remains relatively unchanged. It should be noted that the formation of Talbot carpet as illustrated corresponds to one in which the beam splitting grating is illuminated with x-rays having sufficient spatial coherence.

The designs and patterns on the antiscattering grids will correspond to the patterns fabricated into the beam splitting gratings. For example, if the mesh pattern of FIG. **17** is used as the beam splitting grating G_1, the antiscattering grid may also be arranged in a mesh pattern. If the checkerboard pattern of FIG. **18** is used as the beam splitting grating G_1, the antiscattering grid may also be arranged in a checkerboard pattern. Or, if the checkerboard pattern of FIG. **18** is rotated 45° to form a diamond pattern, the antiscattering grid may also be arranged in a rotated checkerboard (diamond) pattern. Additional embodiments may further include other periodic structures such as honeycomb structures.

The transmission through the antiscattering grid is a function of the aspect ratio and the relative size of the absorbing features. This is illustrated in FIG. **42**. The height of the grating is given by h_g, while the width of the apertures between absorbing structures is w_g and the period of the antiscatter grating is p_4. Scattered x-rays with a propagation angle θ from normal such that

$$\tan(\theta)<(w_g/h_g) \qquad \text{[Eqn. 17]}$$

will generally pass through the grid if they happen to not hit one of the absorbing structures end on. Transmission for normal incidence x-rays will be given by the ratio of the area of absorbing and non-absorbing structures. For the case of a 50/50 grid, where $p_4=2w_g$, the best transmission will be 50%. In this case, the transmission of scatter ration at small scattering angles with respect to the primary radiation is the same as the primary radiation, there is not preferential absorption of the scatter radiation. For scatter radiation with scattering angles greater than

$$\theta=\tan^{-1}(w_g/h_g) \qquad \text{[Eqn. 18]}$$

the antiscattering grid preferentially absorbs scatter radiation.

In some embodiments, the antiscattering grid may be used in addition to an analyzer grating G_2 for the detector. Such an embodiment is illustrated in FIG. **43**. Using such a configuration, multiple embodiments of the invention enable one to obtain additional information about the sample.

The embodiment as illustrated in FIG. **43** comprises an x-ray source **002** with microstructured periodic array sub-sources as disclosed in various embodiments, a beam splitting grating G_1 **210**, an antiscattering grid G_4 **420**, and a detector **290**, without the analyzer grating G_2. In absence of the beam splitting grating **210** and the antiscattering grid **420**, this imaging system is similar to most conventional x-ray imaging systems, except for the microstructured x-ray source **002**, which is usually an extended x-ray source. The current art of antiscattering grid is ineffective for absorbing scattered radiation with small scattering angles with respect to the primary radiation because it has a significant fraction of the area that are transparent to both the scatter radiation and primary radiation. This becomes particularly significant for observing subjects such as babies or uncompressed breasts, in which scattering such as Compton scattering can be 5× greater than the signal carrying absorption contrast information. According to embodiments of the invention, scattered radiation can be preferentially absorbed by placing the antiscattering grid at one of the fractional Talbot distances and positioning the absorbing features at the nodes of the corresponding Talbot carpet. This embodiment is particularly important for imaging objects having large volume using high energy x-rays, such as clinical x-ray imaging and security inspection.

According to another embodiment of the invention, a dark-field image may be recorded by the detector **290** without the analyzer grating **220** by placing the antiscattering grid **420** at one of the fractional Talbot distances and positioning the absorbing features at the antinodes (or integer multiples of the antinodes) of the corresponding Talbot carpet. Another dark-field image can be recorded by the detector **290** without the absorption grid **420** but with the analyzer grating **220** aligned so that its absorbing parts are aligned to the antinodes of the Talbot carpet. Because two different dark-field images are obtained at different distances from the beam splitting grating **210**, they will contain different spatial information about the object.

According to another embodiment of the invention, by placing an antiscattering grid at one of the fractional Talbot distances and positioning its absorbing features at the nodes of the corresponding Talbot carpet, several established phase contrast imaging techniques usually done without the antiscattering grid can be used, including differential phase contrast imaging, phase stepping to obtain simultaneous phase, absorption, and scattering images, and imaging using a high spatial resolution detector without phase stepping.

3.2. Detector MTF and DQE

Variations in the detector configuration and positioning may also contribute to improvements in the signal-to-noise ratio for x-ray systems constructed according to the invention. The figures of merit that may be impacted by the selection of detector properties are the modulation transfer function (MTF) and the detection quantum efficiency (DQE).

The presence of Compton scattering, as described above, may contribute to the degradation of these figures of merit. However, other factors may also impact MTF and DQE. The achievable MTF and DQE of a detector depend on different physical processes. The intrinsic physical processes to all x-ray array detectors include the interaction (traveling) range of the photoelectrons produced by the ionizing radiation, production of secondary x-ray fluorescence produced by the ionization/de-excitation of atoms in the detector sensing material by the incident x-rays, and parallax blurring resulting from the finite thickness of the sensing material at oblique incidence angles with respect to the surface normal. Reabsorption of Compton scattered radiation and secondary fluorescence x-rays by the materials of the detector can also contribute to the reduction of MTF and DQE, but this contribution is usually negligible.

Additional processes in actual detectors may also contribute to the reduction of MTF and DQE. For direct conversion digital array detectors (such as amorphous selenium-photoconductor-based flat panel detector), lateral diffusion of charge carriers may contribute to the reduction of MTF ad DQE. For indirect conversion digital array detectors comprising a layer of a phosphor material (such as Gd_2O_2S) ora scintillator material (such as column-grown CsI fibers), light spread due to scattering can contribute significantly to the reduction of the MTF and DQE in the detector.

For all digital array detectors, the fill factor (the percent of the effective detection area) will also contribute to the reduction of MTF and DQE, which can be especially problematic with small detector pixels. For all the factors contributing to the reduction of MTF and DQE, these effects get worse with increasing detector resolution (smaller pixels), and may lead to many design compromises and tradeoffs, including: the compromise between scintillator/phosphor thickness (and, therefore, its quantum detection efficiency); spatial resolution limitations due to light scattering induced image blurring; and considerations and trade-offs between improving resolution (smaller pixels) with detector parameters such as fill factor, material mass density (to which the photoelectron range is inversely proportional), and the elemental composition of the detector sensing material which determines the range of the characteristic fluorescence x-rays.

Most of the detrimental factors to MTF and DQE make a maximum contribution when the radiation is incident near or at the edges of the detector pixels. Thus an improvement in MTF and DQE may be achieved if all the incident radiation is directed to be incident at the center of the detector pixels.

Commonly deployed position-sensitive detectors do not have intrinsic angle sensing/rejection capability. Scattered radiation (including small-angle scattering by fine structures in the object as well as Compton scattering) is part of the undesirable image background, producing "counts" in the detector that are indistinguishable from the "counts" due to the desired radiation.

Therefore, the use of a system comprising a detector that rejects or reduces the scattered radiation can increase the image contrast and the DQE of the system.

3.3. Embodiments with a Modified Detector

As discussed above, the scattered radiation may be blocked by placing an absorption grid or grating aligned such that the absorption regions correspond to the dark Talbot fringes.

Likewise, it is also possible to select the detector grid spacing and positioning so that the centers of the rows (and/or columns) are aligned with the centers of the antinodes of the Talbot fringes, such that the area between sensor pixels (which by definition is made to be transparent to the incident x-rays) correspond to the position of the nodes of the Talbot carpet. By using a detector with such a spacing and alignment, the scattered x-rays that would normally be absorbed by the detector are not absorbed. As a consequence, the noise associated with them in the sensor pixels due to photoelectrons, reabsorption of secondary fluorescence x-rays, and Compton scattering, will be absent, and the signal-to-noise ratio is improved.

FIG. **44** illustrates a system in which the detector is so arranged. As in previous embodiments, the x-rays **888** generated by a source comprising a plurality of microstructured sub-sources **700** arranged in a regular pattern (i.e. a set of lines or an array) generate x-rays that propagate through an object to be examined **240**-M and fall onto a beam-splitting grating **210**-D. The beam-splitting grating is generally a one- or two-dimensional phase-shifting grating, with spacing and period p_1 of the grating having a relationship to the spacing of the sub-sources as described in Eqn. 9 above. The Talbot pattern as illustrated corresponds to a beam splitting grating **210**-D having a 1:1 π/2 phase shifting pattern, as illustrated in, for example, "X-Ray Phase Imaging with Single Phase Grating" by Y Takeda et al., Jpn. J. Appl. Phys. vol. 46, 2007, pp. L89-L91.

A detector comprising various sensor pixels **290**-BP connected electronic backplane **290**-B produces signals related to the number of x-rays detected, and that signal passes through a connector **291** to a data processing system **295** for analysis. The detector is positioned at one of the fractional Talbot distances, i.e.

$$D_5 = D_N = N_5 \frac{p_1^2}{8\lambda} = \frac{N_5}{16} D_T \qquad \text{[Eqn. 19]}$$

where D_N is the fractional Talbot distance for a plane wave illumination, λ is the mean x-ray wavelength, and N_5 is the Talbot fractional order (N=1, 2, 3, . . .) at which the detector is placed.

The spacing p_5 of the sensor pixels is then selected to correspond to the Talbot spacing for the corresponding beam-splitting grating G_1. The relationship is given by:

$$p_5 = Kp_0\frac{D_5}{L} \qquad \text{[Eqn. 20]}$$

where p_0 is the period of the microstructured source, L the distance between the x-ray sources **700** and the diffraction grating **210**-D, and K is a scaling factor which is equal to 1 when the beam-splitting grating introduces a phase shift of $\pi/2$, and is equal to ½ when the beam-splitting grating introduces a phase shift of π.

FIG. **45** illustrates another embodiment in which the grating **210**-D is used to produce a Talbot interference pattern. The detector **290**-B-L comprises pixels **290**-BP-L in which the majority of the area of the detector comprises pixels, with only a small gap between pixels. The detector **290**-B-L is placed at a predetermined Talbot distance (fractional or odd integer) such that the antinodes (regions of constructive interference) of the Talbot pattern is incident on or near the center of each detector pixel **290**-BP-L. Thus the detector has a periodicity that corresponds to the period of the Talbot pattern. Such a grating and detector scheme may be used with the microstructured source previously mentioned, or with any other source with sufficient lateral coherence, such as a microfocus source.

The designs and patterns on the detector grids will correspond to the patterns fabricated into the beam splitting gratings. For example, if the checkerboard pattern of FIG. **18** is used as the beam splitting grating G_1, the detector grid may also be arranged in a checkerboard pattern. Or, if the mesh pattern of FIG. **17** is used as the beam splitting grating G_1, the detector grid may also be arranged in a mesh pattern. If the checkerboard pattern of FIG. **18** is rotated 45° to form a diamond pattern, the detector grid may also be arranged in a rotated checkerboard (diamond) pattern.

3.4. "Single Shot" Talbot Techniques

Existing x-ray imaging systems for clinical, security inspection, and nondestructive test use primarily absorption contrast (difference in attenuation between neighboring features). It has been long recognized that x-ray phase contrast (difference in phase shift between neighboring features) can be significantly larger than absorption contrast for most materials at high energy x-rays, especially for low Z materials. Recently, scattering contrast (difference in small angle scattering strength between neighboring features) has been recognized for imaging sub-resolution features within an imaging resolution element (such as pores and fine structures of dimension less than the imaging resolution). It is highly desirable to be able to simultaneously obtain in a single shot (exposure) an absorption contrast image in combination with at least one of a differential phase contrast image, phase contrast image, or scattering contrast image.

Several researchers have developed single-shot x-ray phase contrast imaging techniques that use beam splitting gratings and an analyzer grating slightly rotated with respect to the beam splitting grating, and then using a Fourier transform image analysis technique to arrive at a phase contrast image. The drawback of this technique is that the image spatial resolution is substantially compromised. Additional developments include further variants of single-shot techniques [see, for example, H. Wen, E. E. Bennett, M. M. Hegedus, and S. C. Carroll, "Spatial harmonic imaging of X-ray scattering—initial results," IEEE Trans. Med. Imaging vol. 27(8), 997-1002 (2008); and H. Wen, E. E. Bennett, M. M. Hegedus, and S. Rapacchi, "Fourier X-ray scattering radiography yields bone structural information," Radiology vol. 251(3), 910-918 (2009)], which they called the "spatial harmonic method". In these references, a single projection image containing a transmission grating (grid) will have several distinct harmonic peaks in the spatial frequency domain. Inverse Fourier transformation of these peaks results in harmonic images. The relative weight between absorption and diffraction-caused attenuations differs among these images, and therefore provide sufficient information to extract separate absorption and diffraction images. Raw images obtained by both single-shot techniques do not contain separate absorption and dark-field (scattering) images, and require image analysis to obtain images from different contrast mechanisms.

3.5. Embodiments with Two Modified Detectors (for "Single Shot" Techniques)

In other embodiments of the invention, a system with two detectors, one positioned at one of the fractional Talbot distances and aligned with its grid (active pixels), spacing (transparent areas between the active pixels) and positioning so that the centers of the rows (and/or columns) are aligned with the centers of the antinodes of the Talbot fringes, while the other positioned at another one of the fractional Talbot distance downstream of the first detector and aligned with its grid (active pixels), spacing (areas between the active pixels, preferably transparent) and positioning so that the centers of the rows (and/or columns) are aligned with the centers of the nodes of the Talbot fringes. By using a pair of detectors with such a spacing and alignment, both the absorption and the scattering (dark-field) images may be collected at the same time, in a "single shot". In some embodiments, the positions of the two detectors can be reversed, but the spacing between the active pixels of the upstream detector in this case should still be sufficiently transparent to x-rays.

FIG. **46** illustrates a system in which a pair of detector is so arranged. As in previous embodiments, the x-rays **888** generated by a source comprising a plurality of microstructured sub-sources **700** arranged in a regular pattern (i.e. a set of lines or an array) generate x-rays that propagate through an object to be examined **240**-M and fall onto a beam-splitting grating **210**-D. The beam-splitting grating is generally a one- or two-dimensional phase-shifting grating, with spacing and period p_1 of the grating having a relationship to the spacing of the sub-sources as described in Eqn. 9 above.

One detector comprising various sensor pixels **290**-BP connected electronic backplane **290**-B produces signals related to the number of x-rays detected, and that signal passes through a connector **291** to a data processing system **295** for analysis. As above, the detector is positioned at one of the fractional Talbot distances, i.e.

$$D_5 = D_N = N_5\frac{p_1^2}{8\lambda} = \frac{N_5}{16}D_T \qquad \text{[Eqn. 21]}$$

where D_N is the fractional Talbot distance for a plane wave illumination, λ is the mean x-ray wavelength, and N_5 is the Talbot fractional order (N=1, 2, 3, . . .) at which the first detector is placed. The active pixels (indicated by the hatched boxes) of the detector **290**-BP are aligned with the antinodes of the corresponding Talbot carpet. The areas between the active pixels are preferably transparent, but not necessary.

As above, the spacing p_5 of the sensor pixels is then selected to correspond to the Talbot spacing for the corresponding beam-splitting grating G_1. The relationship is given by

$$p_5 = Kp_0\frac{D_5}{L} \qquad \text{[Eqn. 22]}$$

where p_0 is the period of the microstructured source, L the distance between the x-ray sources **700** and the diffraction grating **210**-D, and K is a scaling factor which is equal to 1 when the beam-splitting grating introduces a phase shift of $\pi/2$, and is equal to ½ when the beam-splitting grating introduces a phase shift of π.

However, in this embodiment, the system also comprises a second detector comprising various sensor pixels **290**-DP connected electronic backplane **290**-D that produces signals related to the number of x-rays detected for the dark field, and that signal passes through a connector **291**-D to a data processing system **295** for analysis. As above, the detector is positioned at one of the fractional Talbot distances, i.e.

$$D_6 = D_N = N_6\frac{p_1^2}{8\lambda} = \frac{N_6}{16}D_T \qquad \text{[Eqn. 23]}$$

where D_N is the fractional Talbot distance for a plane wave illumination, λ is the mean x-ray wavelength, and N_6 is the Talbot fractional order (N=1, 2, 3, . . .) at which the second detector is placed. The active pixels (indicated by the hatched boxes) of the detector **290**-DP are aligned with the nodes of the corresponding Talbot carpet. The areas between the active pixels need to be sufficiently transparent to x-rays.

As above, the spacing p_6 of the sensor pixels of the second detector is then selected to correspond to the Talbot spacing for the corresponding beam-splitting grating G_1. The relationship is given by

$$p_6 = Kp_0\frac{D_6}{L} \qquad \text{[Eqn. 24]}$$

where p_0 is the period of the microstructured source, L the distance between the x-ray sources **700** and the diffraction grating **210**-D, and K is a scaling factor which is equal to 1 when the beam-splitting grating introduces a phase shift of $\pi/2$, and is equal to ½ when the beam-splitting grating introduces a phase shift of π.

The designs and patterns on the detector grids will correspond to the patterns fabricated into the beam splitting gratings. For example, if the checkerboard pattern of FIG. **18** is used as the beam splitting grating G_1, the detector grids may also be arranged in a checkerboard pattern. Or, if the mesh pattern of FIG. **17** is used as the beam splitting grating G_1, the detector grids may also be arranged in a mesh pattern. If the checkerboard pattern of FIG. **18** is rotated 45° to form a diamond pattern, the detector grids may also be arranged in a rotated checkerboard (diamond) pattern.

With this arrangement, the partially transmitting second detector **290**-DP records a dark-field x-ray image due to a combination of scattering contrast (x-rays scattered by small-angle scattering by sub-resolution features) and/or refraction (phase) contrast from sharp features with a large phase gradient, while the first (image) detector **290**-BP records an image with a combination of an absorption contrast image and/or a refraction (phase) contrast image from features with a small phase gradient. Alternatively, a partially transmitting grating with reverse property from the preceding partially transmitting grating can be used. In this configuration, the images recorded by the partially transmitting detector and the image detector are reversed compared to the preceding detector arrangement.

The ratio of half of the period of the Talbot interference fringe or pattern to the fractional Talbot distance provides a first angular measure which can be used as an approximate measure for substantial presence of scattered/refracted x-rays in the nodes of the Talbot fringes or pattern. By selecting the Talbot fractional orders for the placement of the partially transmitting detector and the main detector and geometric parameters of the beam splitting grating period, distances between the source, beam splitting grating, and x-ray wavelength, one can optimize sub-resolution feature sizes or desired phase gradient of large features for preferentially higher contrast imaging.

An alternative embodiment of a two detector "single shot" system is illustrated in FIG. **47**. Here, the bright Talbot Fringes **889**-B and dark Talbot regions **889**-D are illustrated as propagating away from a beam splitting phase grating with period p_1. At a suitable distance away, typically at a multiple of the fractional Talbot distance, a detector **290**-DS comprising a scintillator **260** and additionally a reflective coating **270** is placed. The reflective coating is such that the visible light **988** generated when the scintillator absorbs x-rays and emits visible or near UV light is reflected to the scintillator. The detector **290**-DS detects the x-rays that are transmitted through the scintillator **260** and the reflector **270**, and may additionally comprise sensor pixels **290**-DPS that are placed at in a regular array with period p_6 such that their positions will correspond to the nodes of the Talbot pattern. This detector **290**-DS may in turn produce signals related to the number of x-rays detected in the nodes due to scattering by features with dimensions smaller than the resolution element of the imaging system, and these signals pass through a connector **291**-D to a data processing system **295** for analysis.

The scintillator **260** may also be coated in a 1-D or 2-D pattern, so that visible or near UV photons are generated only in regions corresponding to high x-ray intensity (i.e. the antinodes of the Talbot fringes).

The system also comprises a beamsplitter **280** that transmits x-rays but reflects visible and/or UV Photons, and a visible/UV imaging system **380** (e.g. a lens or a microscope objective) that forms an image of the bright field portions of the Talbot interference pattern. The visible/UV photons **998** emitted by the scintillator reflect off this beamsplitter, and the reflected visible/UV photons **988**-R are formed into an image by the visible/UV imaging system onto a bright field detector **290**-BS. The visible/UV detector may have a uniform array of pixels, or may have selected regions with a period p_5 with positions arranged to correspond to the images of the bright field portions of the Talbot pattern. The visible/UV detector **290**-BS produces signals related to the number of x-rays detected in the antinodes of the Talbot fringes, and that signal passes through a connector **291**-B to a data processing system **295** for analysis.

In this manner, both bright field and dark field information are gathered in parallel, without the detectors blocking each other, as may be the case for the pair of detectors as was shown in FIG. **46**.

4. Fabrication of Gratings

Fabrication of the gratings used in embodiments of the invention may be made using known prior art fabrication processes such as those previously described by Christian David [C. David et al., "Fabrication of diffraction gratings for hard x-ray phase contrast imaging", Microelectron. Eng. 84, 1172-1177, 2007].

Gratings for x-rays may be fabricated using silicon substrates, with etched changes in topography to induce phase changes and depositions of a higher Z material, such as gold (Au, Z=79), to induce absorption changes. The x-ray absorption properties for gold and silicon are illustrated in FIG. **39**.

As shown in FIG. **48**, a periodic pattern **3010** may be etched into a silicon substrate **3000** to create a structure which introduces a periodic phase shift for x-rays falling at normal incidence. The phase shift depends on the etch depth, with a phase-shift of π radians for normal incidence x-rays achieved when the following condition is met:

$$d_{etch} = \frac{1}{2}\frac{\lambda}{|n-1|} = \frac{1}{2}\frac{\lambda}{\delta} \qquad \text{[Eqn. 25]}$$

Values for δ for silicon at several x-ray energies, along with the depth etched structures need to a phase-shift of π radians are shown in Table IV.

A typical grating fabrication process comprises coating a <110> oriented silicon wafer with a photoresist, and patterning the resist using conventional photolithography, focused ion beam lithography, or electron beam lithography. The silicon then undergoes an etching process such as wet etching in, for example, a potassium hydroxide (KOH) solution, or reactive ion etching (RIE), with the etching selectively occurring only for portions of the silicon not masked by the resist. The etch depth may be controlled by adjusting the time of the etch process. Other variations of the etching process will be known to those skilled in the art of semiconductor processing and manufacturing.

TABLE IV

Etch depth for Silicon phase shift of π radians.

X-ray Energy (keV)	Wavelength λ (nm)	δ	π phase shift depth (μm)
3.0	0.413	5.43E−05	3.81
5.0	0.248	1.98E−05	6.26
8.048 (Cu Kα)	0.154	7.58E−06	10.17
10.0	0.124	4.89E−06	12.69
17.48 (Mo Kα)	0.0709	1.59E−06	22.36
30.0	0.0413	5.36E−07	38.52
50.0	0.0248	1.93E−07	64.31
59.39 (W Kα)	0.0209	1.37E−07	76.32
100.0	0.0124	4.82E−08	128.74

Absorption gratings such as those used for G_2 may be fabricated by initially creating a silicon phase grating, as described above, and then depositing an x-ray absorbing material, such as gold, into the grooves already patterned in the silicon. This is illustrated in FIG. **49**, in which an amount of x-ray absorbing material **3030** such as gold has filled the grooves created in a silicon substrate **3000**. One process for the deposition of gold into the silicon grooves involves a standard electroplating processes. To ensure that gold is only deposited into the grooves, a sacrificial layer of aluminum may initially be deposited at an angle, and a seed layer ~50 nm thick comprising Chromium (Cr) and gold (Au) are then deposited. A phosphoric acid treatment removes all the material deposited on the tops of the silicon structures, leaving seed material only in the bottom of the grooves in the silicon. Standard electroplating may follow, with growth of gold occurring only onto the deposited seed layers. Deposition of gold at hundreds of microns can create absorption gratings with a transmission modulation of 75% or more. Absorption will, however, depend on the x-ray energy and the absorption coefficient for the material, as was illustrated in FIGS. **1** and **39**. Other methods for making x-ray absorption gratings will be known to those skilled in the art.

For some applications and for certain x-ray wavelengths, crystal gratings may also be used.

It should be noted that the antiscattering grids or gratings disclosed with these embodiments of the invention can be fabricated using any number of lithographic pattering techniques known to those skilled in the art as well.

5.0 Detector Properties

The detector may be any one of a number of detectors used to form x-ray images. One type of commonly used x-ray detector comprises a fluorescent screen or scintillator, such as one comprising a layer of cesium iodide (CsI), thallium doped CsI, yttrium aluminium garnet (YAG) or gadolinium sulfoxylate (GOS), that emits visible photons when exposed to x-rays. The visible photons are then detected by an electronic sensor that converts visible intensity into electronic signals, often with the additional formation of a relay image using visible optics that enlarge and magnify the intensity pattern of the photons emitted by the fluorescent screen. With the relay optics, the electronic detector need not comprise a high resolution sensor itself, and inexpensive commercial CCD detectors or complementary metal-oxide-semiconductor (CMOS) sensor arrays with, for example, 1024×1024 pixels, each 24 μm×24 μm square, may be used.

Commercial flat panel digital x-ray sensors in which a layer of scintillator material is placed in close proximity to (or even coated onto) an array of conventional optical image sensors are manufactured by, for example, Varian Inc. of Palo Alto, Calif. and General Electric, Inc. of Billerica, Mass. Other configurations of image sensors may be known to those skilled in the art. In embodiments in which a G2 analyzer grating is used, it is preferable to use highly efficient, fast read-out detectors such as flat panel detectors, used for medical and industrial uses. For many applications, using a flat panel detector with a resolution larger than 20 microns will require that an analyzer grating G_2 with a period equal to the Talbot fringe period be placed in the x-ray beam path before the detector.

A second approach is to use an electronic sensor that directly creates an electrical signal in response to the absorption of x-rays, by, for example, the creation of direct electron-hole pairs in amorphous selenium (a-Se). These are then converted into electronic signals using an array of thin-film transistors (TFTs). Such direct flat panel detectors

(FPDs) such as the Safire FPD of Shimadzu Corp. of Kyoto, Japan, are commercially available.

6.0. Variations

Embodiments may further comprise other components typically included in Talbot interferometer, including spectral filters to obtain a desired x-ray energy bandwidth and positioning control systems for all the various components of the system.

It should be noted that certain terms used within this disclosure will be well known to those skilled in the art, such as grids or gratings. In the descriptions here, grids and gratings are terms that may be used interchangeably, and are not meant to be restrictive to a particular grid, period, or pattern.

Likewise, it should be noted that certain terms used within this disclosure will be well known to those skilled in the art, such as Talbot fringes, interference patterns, or “carpets”. In the descriptions here, interference patterns, fringes, or “carpets” are terms that may be used interchangeably, and are not meant to be restrictive to any particular intensity pattern.

Likewise, it should be noted that certain terms used within this disclosure will be well known to those skilled in the art, such as septa for the absorbing structures of antiscattering grids. In the descriptions here, septa or septum or structure are terms that may be used interchangeably in reference to the absorbing structures of the antiscattering grid, and are not meant to be restrictive to any particular ratio of height to width, or to imply a solely one-dimensional geometry.

With this application, several embodiments of the invention, including the best mode contemplated by the inventors, have been disclosed. It will be recognized that, while specific embodiments may be presented, elements discussed in detail only for some embodiments may also be applied to others.

While specific materials, designs, configurations and fabrication steps have been set forth to describe this invention and the preferred embodiments, such descriptions are not intended to be limiting. Modifications and changes may be apparent to those skilled in the art, and it is intended that this invention be limited only by the scope of the appended claims.

We claim:

1. An x-ray transmission imaging system comprising:

a source of x-rays comprising:

a vacuum chamber;

an emitter for an electron beam; and

an electron target comprising:

a substrate comprising a first material[and, embedded in the substrate,]*; and*

at least a plurality of discrete [structures] *sub-sources embedded in the substrate and* comprising a second material selected for its x-ray generating properties, [and in which said] *the* plurality of discrete [structures; are arranged within a periodic pattern of sub-sources] *sub-sources arranged in a periodic pattern*;

a stage to position and orient an object to be examined;

an x-ray detector comprising a two-dimensional array of x-ray detecting elements[,] positioned to detect x-rays transmitted through the object to be examined;

[said x-ray transmission system additionally comprising:]

a scattering rejection apparatus placed between the position of the object to be examined and the detector, *the scattering rejection apparatus* comprising:

a [beam-splitting] *beam splitting* x-ray grating comprising periodic structures that form an x-ray phase-shifting grating positioned to diffract x-rays generated by the sub-sources [of x-rays] so that a Talbot interference pattern is formed by the interaction of the x-rays generated by the source of x-rays with the beam splitting *x-ray* grating; and

[an] *a first* antiscattering grid having a periodic array of septa comprising an x-ray absorbing material positioned between the beam splitting x-ray grating and the detector[and]*, the septa having dimensions and periodicity that correspond to dimensions of the Talbot interference pattern*;

a controller for adjusting the position of the [anti-scattering] *first antiscattering* grid relative to the Talbot interference pattern[; in which the dimensions and periodicity of the septa of the antiscattering grid are selected to correspond to the dimensions of the Talbot interference pattern, and the septa of the antiscattering grid are positioned] such that the septa are aligned with the nodes of the Talbot interference pattern*; and*

a second antiscattering grid positioned between the first antiscattering grid and the detector.

2. The x-ray transmission imaging system of claim **1**, in which

the x-ray phase shifting grating comprises structures to introduce a phase-shift of approximately π radians for a predetermined x-ray wavelength.

3. The x-ray transmission imaging system of claim **1**, in which

the x-ray phase shifting grating comprises structures to introduce a phase-shift of approximately π/2 radians for a predetermined x-ray wavelength.

4. The x-ray transmission imaging system of claim **1**, in which the periodic structures of the x-ray phase-shifting grating have a period p_1 related to a dimension a for at least one of the discrete [structures] *sub-sources* of the x-ray target by:

$$p_1 < \lambda L/a$$

where λ is a predetermined x-ray wavelength, and L is the distance between the target and the [beam-splitting] *beam splitting* x-ray grating.

5. The x-ray transmission imaging system of claim **1**, in which the septa of the *first* antiscattering grid comprise a high Z material selected from the group consisting of: tin, platinum, gold, tungsten, tantalum, molybdenum, nickel, lead, copper and gadolinium.

6. The x-ray transmission imaging system of claim **1**, in which the *first* antiscattering grid additionally comprises a substrate comprising an x-ray transparent material.

7. The x-ray transmission imaging system of claim **1**, in which

one or more of the septa have a height that is greater than 5 times the width of the gap between said one or more of the septa and its neighboring septa.

8. The x-ray transmission imaging system of claim **1**, in which the period of the septa of the *first* antiscattering grid is an integer multiple of the lateral period of the Talbot interference pattern.

9. The x-ray transmission imaging system of claim **1**, [additionally comprising: a] *wherein the* second antiscattering grid **[**comprising**]** *comprises* an x-ray absorbing material**[** positioned between the first antiscattering grid and the detector**]**.

10. The x-ray transmission imaging system of claim **1**, in which the contrast of the Talbot interference pattern is greater than 20%.

11. The x-ray transmission imaging system of claim **1**, in which the plurality of discrete **[**structures are**]** *sub-sources is* arranged in a two-dimensional periodic pattern of sub-sources.

12. The x-ray transmission imaging system of claim **11**, in which

the two-dimensional periodic pattern of sub-sources comprises a mesh pattern.

13. The x-ray transmission imaging system of claim **11**, in which

the two-dimensional periodic pattern of sub-sources comprises a checkerboard.

14. The x-ray transmission imaging system of claim **11**, in which

the x-ray phase shifting grating comprises a two-dimensional periodic pattern of phase-shifting structures.

15. The x-ray transmission imaging system of claim **1**, **[**additionally comprising: an analyzer grating having**]** *wherein the second antiscattering grid comprises* periodic structures of x-ray absorbing material**[** positioned between the antiscattering grid and the detector**]**.

16. The x-ray transmission imaging system of claim **1**, in which

the Talbot interference pattern comprises diverging interference fringes.

* * * * *

UNITED STATES PATENT AND TRADEMARK OFFICE

CERTIFICATE OF CORRECTION

PATENT NO. : RE48,612 E
APPLICATION NO. : 16/523940
DATED : June 29, 2021
INVENTOR(S) : Wenbing Yun

Page 1 of 1

It is certified that error appears in the above-identified patent and that said Letters Patent is hereby corrected as shown below:

In the Specification

In Column 13, Line 11, delete "λ" and insert --π--.

In Column 19, Line 19, delete "Ouch" and insert --(such--.

In Column 24, Line 41, delete "AT" and insert --ΔT--.

Signed and Sealed this
Thirtieth Day of August, 2022

Katherine Kelly Vidal

Katherine Kelly Vidal
Director of the United States Patent and Trademark Office